Determination of the polarization amplitudes and *CP* asymmetries
in *B*⁰ → φ *K**(892)⁰ at LHCb

PAR

Anh Duc NGUYEN

Abstract

The LHCb experiment is one of the large experiments installed around the LHC collider. Its aim is the study of CP violation and rare b-hadrons decays. This thesis addresses these two objectives.

CP violation was found in 1964 in the decays of neutral kaons by J. H. Christenson, J. W. Cronin, V. L. Fitch, and R. Turlay. It was reconfirmed in 2001 in B meson systems by BaBar and Belle experiments. CP violation can be explained in the Standard Model (SM) using the Cabibbo-Kobayashi-Maskawa (CKM) matrix with three quark generations.

The $B^0 \to \phi K^*(892)^0$ is a rare flavour changing neutral decay which processes via the gluonic penguin diagram ($b \to s$ transition). In SM, the predicted CP asymmetry is so small for this decay channel that any deviation from the SM value would signal "New Physics".

This decay is a pseudo-scalar (B^0) decaying to vector mesons (ϕ and $K^*(892)^0$) with spin-1. Conservation of angular momentum leads to three possible helicity states of the vector mesons which reflects into three amplitudes: these will be unravelled by an angular analysis of the final-state particles, $\phi \to K^+ K^-$ and $K^*(892)^0 \to K^+ \pi^-$.

An angular analysis of the decay $B^0 \to \phi K^*(892)^0$ is reported based on data of pp collision at a centre-of-mass energy of $\sqrt{s} = 8\,\text{TeV}$ and corresponding to an integrated luminosity of 2.0 fb^{-1}, with the LHCb detector. The analysis includes both the contribution of $K^+\pi^-$ and K^+K^- S–waves and a significant contribution from them is found. The measurements of P–wave amplitudes and phases is consistent with the one of BaBar and Belle experiments, but are much more precise. Our results also confirm the previous LHCb one bay on a statistics corresponding to an integrated luminosity of 1.0 fb^{-1}. The longitudinal polarization fraction f_{L} for the P–wave is measured to be $0.499 \pm 0.011(\text{stat}) \pm 0.010(\text{syst})$. The differences between the polarization amplitudes and phases of the $B^0 \to \phi K^*(892)^0$ and $\overline{B}^0 \to \phi \overline{K}^*(892)^0$ decays have been derived as well as the triple-product asymmetries. The results show no evidence for direct CP violation.

Keywords: LHCb experiment, CKM matrix, CP violation, flavour physics, charmless B decays.

iv

Résumé

L'expérience LHCb est l'une des grandes expériences installées sur l'anneau du collisionneur LHC. Le but de LHCb est d'étudier la violation de la symétrie CP et les désintégrations rares de hadrons comportant un quark b.

La violation de CP a été découverte en 1964 dans les désintégrations des kaons neutres par J.H. Christenson, J.W. Cronin, V.L. Fitch et R. Turlay. Elle a été confirmée en 2001 dans le système des mésons B auprès des expériences BaBar et Belle. Dans le cadre du modèle standard (MS), la violation de CP peut être expliquée par la théorie de Cabibbo, Kobayashi et Maskawa (CKM) faisant intervenir trois générations de quarks.

La désintégration $B^0 \rightarrow \phi K^*(892)^0$ est une désintégration rare, neutre, changeant la saveur des quarks et procède via un diagramme pingouin pour la transition $b \rightarrow s$. Dans le MS, l'assymétrie CP pour cette désintégration est prédite comme étant faible et toute déviation de cette prédiction signalerait la présence d'une "Nouvelle Physique".

Dans cette désintégration, un méson pseudo-scalaire (le B^0) se désintègre en deux mésons vectoriels (les mésons ϕ et $K^*(892)^0$). La conservation du moment angulaire conduit à trois états d'hélicité possibles qui se retrouvent dans trois amplitudes de transition, lesquelles peuvent être obtenues par une analyse angulaire de l'état final $\phi \rightarrow K^+K^-$ et $K^*(892)^0 \rightarrow K^+\pi^-$.

Dans ce mémoire, nous présentons une analyse angulaire de la désintégration $B^0 \rightarrow \phi K^*(892)^0$ basée sur les données enregistrées à l'expérience LHCb dans les collisions pp à une énergie dans le centre de masses de $\sqrt{s} = 8$ TeV pour une luminosité intégrée de 2.0 fb^{-1}. Dans l'analyse, les contributions des ondes S des systèmes $K^+\pi^-$ et K^+K^- sont prises en compte et nous avons trouvé que leur contribution est significative. Les amplitudes et les phases des ondes P trouvées sont consistantes avec celles obtenues des expériences BaBar et Belle. Par ailleurs, nos résultats confirment aussi les résultats précédents de LHCb basés sur une statistique moins importante et correspondante à une luminosité de 1.0 fb^{-1}.

La proportion de l'amplitude de polarisation longitudinale f_{L} dans l'onde P est de 0.499 ± 0.011 (stat) ± 0.010 (syst), confirmant le désaccord observé par les expériences précédentes avec l'attente naïve d'une dominance de l'amplitude de polarisation longitu-

dinale. L'assymétrie CP brute et les assymétries dans les produits mixtes ont aussi été déduites de l'analyse angulaire; les résultats ne montre pas d'évidence de la violation directe de CP.

Mots clefs: expérience LHCb, matrice CKM, violation de CP, physique de la saveur, désintégration hadronique du méson B sans apparition de charme.

Tóm tắt luận án

LHCb là một trong những thí nghiệm lớn hoạt động trên máy gia tốc LHC. Mục đích của thí nghiệm là nghiên cứu vi phạm đối xứng CP và các kênh phân rã hiếm của hadron b. Trong bản luận án này sẽ trình bày hai vấn đề nêu trên.

Vi phạm đối xứng CP được phát hiện năm 1964 trong kênh phân rã kaon trung hòa bởi J. H. Christenson, J. W. Cronin, V. L. Fitch, and R. Turlay. Hiện tượng trên được khẳng định trong hệ meson B bởi các thí nghiệm BaBar và Belle vào năm 2001. Vi phạm đối xứng CP có thể được giải thích trong khuôn khổ Mô hình Chuẩn bằng cách sử dụng ma trận CKM với ba thế hệ quark.

Kênh $B^0 \to \phi K^*(892)^0$ là quá trình phân rã trung hòa hiếm, trong đó "flavour" được thay đổi (chuyển đổi $b \to s$) thông qua giản đồ Feynman gluon.

Theo Mô hình Chuẩn, giá trị của vi phạm đối xứng CP được tiên đoán cho kênh này nhỏ đến mức mà bất cứ độ lệch nào ra khỏi giá trị của Mô hình Chuẩn cũng được coi là thông tin về Vật lý mới (New Physics).

Trong kênh được nghiên cứu, meson giả vô hướng (B^0) phân rã thành hai vector meson (ϕ và $K^*(892)^0$) có spin-1. Do bảo toàn mômen xung lượng dẫn đến chỉ tồn tại ba trạng thái helicity của các vector meson. Biên độ của ba trạng thái helicity trên sẽ được xác định thông qua phân tích phân bố góc của các hạt con trong hai phân rã, $\phi \to K^+K^-$ và $K^*(892)^0 \to K^+\pi^-$.

Kết quả nghiên cứu phân bố góc của kênh $B^0 \to \phi K^*(892)^0$ thu được dựa trên việc phân tích số liệu va chạm pp với năng lượng trong hệ khối tâm $\sqrt{s} = 8\,\text{TeV}$ được ghi nhận bởi detector LHCb; số liệu trên tương ứng với Luminosity tổng cộng là 2.0 fb^{-1}. Quá trình phân tích có tính đến và cho thấy sự đóng góp rõ rệt từ sóng S của tổ hợp $K^+\pi^-$ và K^+K^-. Các biên độ và pha phân cực thu được từ sóng P trong luận án này phù hợp với kết quả của hai thí nghiệm BaBar và Belle nhưng với độ chính các cao hơn nhiều. Tỷ số phân cực dọc f_L cho sóng P nhận giá trị $0.499 \pm 0.011(\text{stat}) \pm 0.010(\text{syst})$. Sự sai khác giữa biên độ và pha phân cực trong hai phân rã $B^0 \to \phi K^*(892)^0$ và $\overline{B}^0 \to \phi \overline{K}^*(892)^0$ được xác định cũng như bất đối xứng của tích bộ ba (triple-product asymmetries). Các kết quả cho thấy không có bằng chứng rõ rệt của vi phạm đối xứng CP trực tiếp.

Từ khóa: Thí nghiệm LHCb, ma trận CKM, vi phạm đối xứng CP, Vật lý "flavour", phân rã B meson.

Acknowledgements

First and foremost, I would like to express my gratitude to my supervisor, Dr Trần Minh Tâm, who dedicated his valuable time to support, encourage and guide me throughout my thesis work. I would like to thank him for being so patient in the correction of my thesis dissertation and in the preparation of its defense. I also express my gratitude to Prof. Aurelio Bay, Prof Nakada Tatsuya and Prof. Olivier Schneider who together with my supervisor have given me the opportunity to work on this thesis at the High Energy Physics Laboratory (LPHE), EPFL.

I also would like to thank all the members of the jury for their important comments as well as corrections, particularly Dr Greig Cowan for his long list of enlightening suggestions that have much improved this dissertation.

I would also like to thank all my colleagues from the LPHE. Thanks to Dr Frédéric Blanc for his help and useful suggestions, and to Prof. Maurice Gailloud for his help to apprehend some complex theory and calculations in the early stage of my work. I am greatly indebted to the LPHE secretaries, Mrs Erika Lüthi and Mrs Esther Hofmann for their indispensable technical support and their kindness.

I would also like to thank the group of High Energy Physics (GPHE) of the Hanoi University of Sciences, VNU. I am grateful to Prof. Nguyễn Mậu Chung who directed me in the field of Particle Physics. Thanks for his patient help in various aspects of my work and in particular in the understanding of relevant physics theory at the beginning of my career.

I would like to thank all my friends from the Association of Vietnamese Students in Lausanne, especially those in EPFL for the activities and fun during the numerous lunch breaks at Le Vinci.

I also acknowledge support from the project 322 of the Ministry of Education and Training (MOET) of Vietnam and from the Hanoi University of Sciences, VNU.

Last but not least, I also wish to thank my parents for their unconditional support and love. And most importantly, I am deeply thankful to my wonderful wife Diệu Thu and our little princess Anh Thư, for bringing me great support and happiness in my life, although they cannot be here with me during the preparation time of my thesis. I am indebted to my wife for her understanding, her love and especially her sacrifices to take care of our baby.

x

Contents

Introduction

In the Standard Model, the rare flavour changing neutral process $B^0 \to \phi K^*(892)^0$ proceeds mainly via the gluonic penguin diagram in which the $b \to s$ transition occurs as shown in Figure 1. The first evidence for this decay was provided by the CLEO [1] and BaBar collaborations [2]. Measurements of the branching fraction as well as angular analyses have been performed by both the BaBar and Belle collaborations [3–7]. A complete angular analysis of this process has also been performed by LHCb and has appeared in Reference [8]. The averaged branching fraction is $(1.00 \pm 0.05) \times 10^{-5}$ given in the Particle Data Group (PDG) [9].

In the channel $B^0 \to \phi K^*(892)^0$, pseudo-scalar B^0 mesons decay to charmless vector mesons ϕ and $K^*(892)^0$ ($P \to VV$). We proceed as follows: first the daughter particles ϕ and $K^*(892)^0$ are reconstructed from the KK and $K\pi$ final particles, next is the B^0 meson. In the rest frame of the ϕ and $K^*(892)^0$, the direction of the K from the daughter particle decays, with respect to the B^0 directions, define the angles which will be used in the analysis. The decay amplitudes of $P \to VV$ can be decomposed into three helicity components, one for each helicity of the final state: H_0, H_+ and H_- (see further detail in section 3.1). They can also be defined in the transversity basis with transverse amplitudes $A_0 = H_0$, $A_\parallel = \frac{1}{\sqrt{2}}(H_+ + H_-)$ and $A_\perp = \frac{1}{\sqrt{2}}(H_+ - H_-)$[1]. The Standard Model factorization predicts that the helicity amplitudes for $P \to VV$ decays satisfy the amplitude hierarchy $H_0 \gg H_+ \gg H_-$ (see Appendix A). This means that $P \to VV$ decays are naively expected to be dominated by the longitudinal polarization states and satisfy the scaling law

$$1 - f_{\mathrm{L}} = \mathcal{O}\left(\frac{m_V^2}{m_B^2}\right) \quad \text{and} \quad \frac{f_\perp}{f_\parallel} = 1 + \mathcal{O}\left(\frac{m_V}{m_B}\right), \tag{1}$$

where f_{L}, $f_\perp$ and $f_\parallel$ are the longitudinal, perpendicular and parallel polarization fractions respectively, defined by $f_\alpha = |A_\alpha|^2 / \sum |A_\alpha|^2$, $\alpha = \mathrm{L}, \perp, \parallel$ and m_V is the mass of the

---

[1]In this analysis A_0 is equivalent to A_{L} (Longitudinal component).
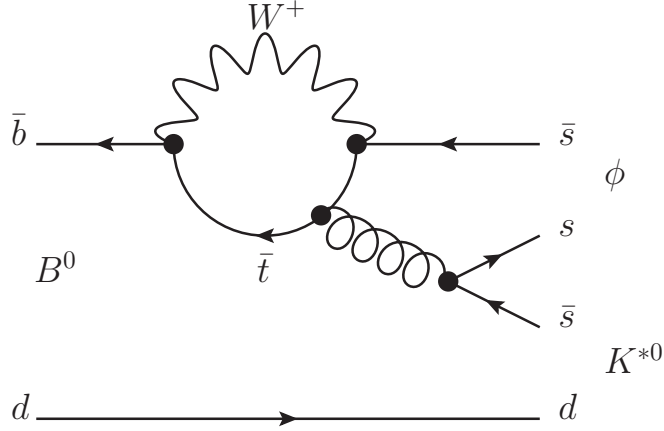
Figure 1: Penguin diagram describing the $B^0 \to \phi K^{*0}$ decay. The loop is dominated by the top quark.

vector meson involved in the decay. This expectation seems to be confirmed in tree dominated decays $B^0 \to \rho^+\rho^-$ and $B^0 \to \rho^0\rho^0$ by Belle: $f_{\rm L}(\rho^+\rho^-) = 0.941^{+0.034}_{-0.040} \pm 0.03$ [10] and BaBar: $f_{\rm L}(\rho^+\rho^-) = 0.992 \pm 0.024^{+0.026}_{-0.013}$ [11] and $f_{\rm L}(\rho^0\rho^0) = 0.75^{+0.11}_{-0.14} \pm 0.04$ [12], except for a new publish of Belle in 2014 shows that $f_{\rm L}(\rho^0\rho^0) = 0.21^{+0.18}_{-0.22} \pm 0.15$ [13] is too small compare to BaBar result. This is not the case, however, for penguin $b \to s$ decays as for $B^+ \to \phi K^{*+}$ or $B^0 \to \phi K^{*0}$. $f_{\rm L}$ is naively expected to be $1 - 4m_V^2/m_B^2 \sim 0.9$ in $B^0 \to \phi K^*(892)^0$ decay. Whereas measurements from BaBar, Belle and LHCb collaborations show that $f_{\rm L} \approx 0.5$ [7, 8, 14]. This discrepancy between Standard Model prediction and experimental measurement has been known as the "Polarization Puzzle". Not only the $B^0 \to \phi K^*(892)^0$ decay is concerned, but most of experimental measurements for $P \to VV$ decays also are, as summarized in Figure 2. Several mechanisms have been proposed to explain this phenomena such as penguin-included annihilation contribution [15], final state interactions [16] and new physics effects [17]. Among these, the next-to-leading-order factorizable correction [17], [18] approach gives $f_{\rm L}(\phi K^*(892)^0) \sim 0.6$ and is much more consistent with experimental results. However this approach suffers from large uncertainties due to weak annihilation effects.

$B^0 \to \phi K^{*0}$[2] decay is a flavour specific one: the flavour of the B^0 (or $\overline{B}^0$) can be determined by the charge of the pion (π^- for the B^0 and π^+ for the $\overline{B}^0$). With a flavour specific decay, one has the opportunity to search for direct CP violation in the decay amplitudes. As in a CP search we deal with the moduli of the amplitudes corresponding to matter and anti-matter transitions, for the CP violation to be apparent and significant, we need

---

[2]In this thesis K^{*0} is also defined as $K^*(892)^0$ unless otherwise stated.
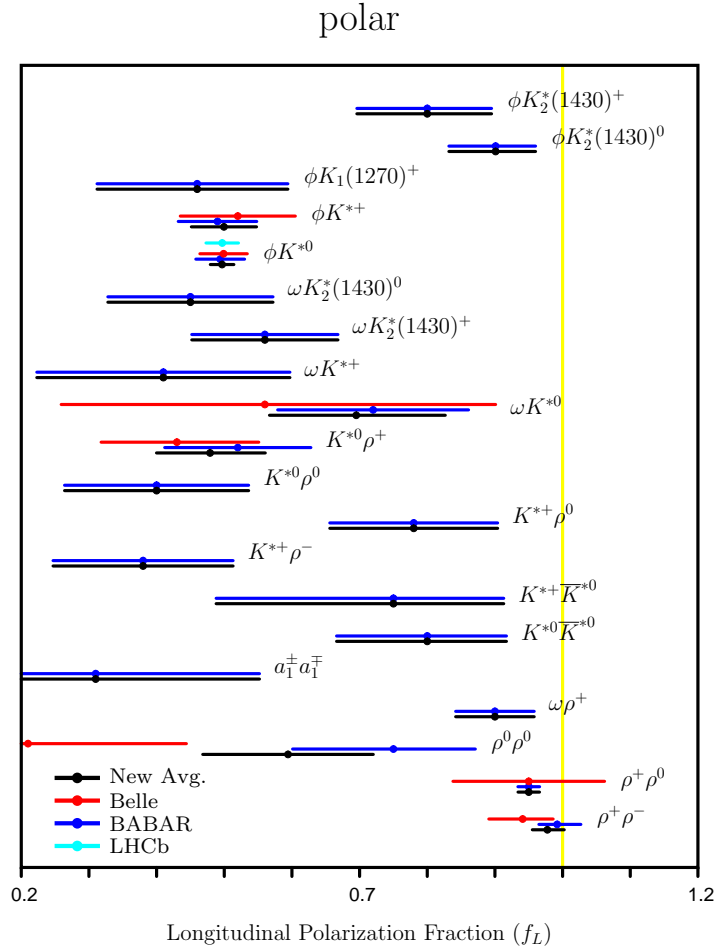
Figure 2: Longitudinal polarization fraction, $f_{\rm L}$, for different B meson decays in two vector particles as of August 2014 [19].

at least two competing mechanism whose amplitudes should have similar magnitudes but different phases; for the two moduli to be different, these phases must include a strong part which remains invariant under CP and a weak part which changes sign under CP. In our case $B^0 \to \phi K^{*0}$, the penguin loop (Figure 1) is dominated by the heavy top quark making the contribution of lighter quarks (c, u) negligible. With a single amplitude, one expect in Standard Model that the decay amplitudes squared for $B^0 \to \phi K^{*0}$ and $\overline{B}^0 \to \phi \overline{K}^{*0}$ to be quite close one to the other. It is therefore not surprising that CP asymmetries were found to be consistent with zero in many previous measurement [3–7].

In this dissertation, we will evidence the direct CP violation using the "triple-product" asymmetries as suggested by A. Datta and D. London [20] and by M. Gronau and J. L. Rosner [21]. These triple-product asymmetries can indeed be deduced from the amplitudes and phases obtained in the polarization study stage. Our group has published [8]

the results on the polarization amplitudes in $B^0 \to \phi K^{*0}$ and the related CP asymmetries based on a pp collision data sample selected in 2011 corresponding to an integrated luminosity of 1.0 fb^{-1}. In this publication [8], we confirm that the CP asymmetries are consistent with zero and that longitudinal polarization fraction $f_{\rm L} = 0.497 \pm 0.019 \pm 0.015$. The analysis of $B^0 \to \phi K^*(892)^0$ decay presented in this dissertation used data of pp collision at a centre-of-mass energy of $\sqrt{s} = 8 \, {\rm TeV}$ corresponding to an integrated luminosity of 2.0 fb^{-1}, with the LHCb detector. The polarization amplitudes and phases, CP asymmetries as well as triple-product asymmetries are determined using the results of the angular analysis which includes the contributions from both K^+K^- and $K^+\pi^-$ of $P-$ and S–wave.

This report is organized as follows. The first chapter introduces the basics of the Standard Model and summarises different types of CP violation in the B system. The next chapter describes the LHCb detector and its subsystems as well as its analysis tools. In Chapter 3, we will present the model used to fit the angular and mass distribution of the $B^0 \to \phi K^{*0}$ decay products in the observed data. In the second part, we parametrize the acceptance of the detector as a function of the helicity angles and $K\pi$ invariant mass in term of orthogonal functions (Legendre polynomials and real-valued spherical harmonics) and use the method of "normalization weights" to correct the acceptance effects. The experimental reconstruction and selection of the signal decay are described in Chapter 4 and the results of the measurements in Chapter 5, where the background study and the systematic uncertainties will be reported. Finally, a summary and conclusions are given.

Chapter 1

CP Violation in B meson system

This chapter is devoted to briefly introducing the phenomenology. After recalling the basics of the Standard Model, and as we are a member of the LHCb experiment, we will spend a large part of this chapter to B physics. Several types of CP violation in the B system will be discussed.

1.1 The Standard Model of Particle Physics

The Standard Model (SM), developed in the early 1970s, is a theory describing the fundamental particles and their interaction. It incorporates relativity and quantum mechanics: it is based on quantum field theory. Until now, most particles of this model have been discovered, and most recently the Higgs boson [22], [23] at the Large Hadron Collider (LHC) at the European Organization for Nuclear Research (CERN).

The SM attempts to explain all the phenomena of particle physics in term of the properties and interactions of the fundamental particles, which can be classified in three distinct types: two spin-$\frac{1}{2}$ families, and one family of spin-1 bosons. In addition, one spin-0 particle, called the Higgs boson, is postulated to explain the origin of mass. Quarks and leptons are the two spin-$\frac{1}{2}$ fermion families. The charge and mass of these particles are summarized in Table 1.1

The interactions between the fundamental particles, the electromagnetic, the weak and the strong force, are mediated by four vector bosons of spin-1. The photon, γ, is the exchanged particle in the electromagnetic interaction, the eight gluons mediate the strong interactions among quarks, and the three weak bosons, $W^{\pm}$ and Z, are the corresponding intermediate bosons of the weak interactions. The charge and mass of these bosons are summarised in Table 1.2.

		Quarks			Leptons	
Gen.	Particle	Charge	Mass	Particle	Charge	Mass
I	$\begin{pmatrix} u \\ d \end{pmatrix}$	$+\frac{2}{3}$ $-\frac{1}{3}$	$2.3^{+0.7}_{-0.5}\,\text{MeV}$ $4.8^{+0.5}_{-0.3}\,\text{MeV}$	$\begin{pmatrix} \nu_e \\ e^- \end{pmatrix}$	0 -1	$< 2\,\text{eV}$ $511.0\,\text{keV}$
II	$\begin{pmatrix} c \\ s \end{pmatrix}$	$+\frac{2}{3}$ $-\frac{1}{3}$	$1.28 \pm 0.03\,\text{GeV}$ $95 \pm 5\,\text{MeV}$	$\begin{pmatrix} \nu_\mu \\ \mu^- \end{pmatrix}$	0 -1	$< 2\,\text{eV}$ $105.7\,\text{MeV}$
III	$\begin{pmatrix} t \\ b \end{pmatrix}$	$+\frac{2}{3}$ $-\frac{1}{3}$	$173.2 \pm 0.9\,\text{GeV}$ $4.18 \pm 0.03\,\text{GeV}$	$\begin{pmatrix} \nu_\tau \\ \tau^- \end{pmatrix}$	0 -1	$< 2\,\text{eV}$ $1.78\,\text{GeV}$

Table 1.1: Properties of the fermions in the SM [9].

The ideal of gauge invariance is one of the most important one in particle physics as it is

Name	Symbol	Charge	Mass $[\,\text{GeV}/c^2\,]$	Interaction
Photon	γ	0	0	Electromagnetism
W boson	$W^\pm$	± 1	80.39 ± 0.02	Weak
Z boson	Z	0	91.19 ± 0.002	Weak
Gluon	g	0	0	Strong
Higgs boson	H^0	0	125.7 ± 0.4	

Table 1.2: Properties of the bosons in the SM [9].

now used to describe the four fundamental forces. The basic method of gauge theory is to preserve the invariance of the Lagrangian describing the interaction of the particles under the symmetry transformations of the particle wave functions; these symmetry transformations concerning the conservation laws obtained in nature: for example, the separate conservation of lepton number for electron, muon and tau leads to the symmetry $SU(2)_L$ or weak isospin transformation which must be accounted for in the theory.

Quantum Electrodynamics (QED)

We start with QED which intends to describe the interaction of charged particles, for instance the electron. The Lagrangian which describes the electron wave function has to be invariant under a change in the phase of the electron wave function. If this change is unique at all points in space-time, this operation, call global phase transformation $G\mathcal{L}(\psi_e) \to \mathcal{L}(\psi_e^*)$, should not affect the observation as we know that the laws of physics do not depend upon any phase convention.

This exercise is more difficult if we demand that the change of the phase be dependent

of space-time

$$G(x)\mathcal{L}(\psi_e) \rightarrow \mathcal{L}^*(\psi_e^*) . \tag{1.1}$$

Now, due to the derivatives that exist in the Lagrangian, this latter is changed by the transformation: $\mathcal{L}^* \neq \mathcal{L}$, that means the Lagrangian is not invariant under this new symmetry. However, by redefining the derivative as a "covariant derivative" which includes the electromagnetic field $A_\mu(x)$, the Lagrangian can be made invariant:

$$G(x)\mathcal{L}(\psi_e, A) \rightarrow \mathcal{L}(\psi_e^*, A^*) . \tag{1.2}$$

This is no surprise as we know that the interaction of two electrons is described by one electron interacting with (emitting) a photon at point A, the propagation of the photon until its interaction (absorption) at another point B. Another interesting point here is the fact that the invariance of the Lagrangian under the local gauge transformation implies a massless boson, the photon whose range is infinite.

Now for the weak interaction, we have seen that the separate conservation of lepton numbers exist. It is therefore "natural" to group the leptons' wave functions into doublets

$$\begin{pmatrix} \nu_e \\ e^- \end{pmatrix}_L , \qquad \begin{pmatrix} \nu_\mu \\ \mu^- \end{pmatrix}_L , \qquad \begin{pmatrix} \nu_\tau \\ \tau^- \end{pmatrix}_L , \tag{1.3}$$

where the subscript L refer to left handed leptons. We note here that there is a similarity between these doublets and the isospin doublet of nucleons $\begin{pmatrix} p \\ n \end{pmatrix}$ for which the strong interaction only "sees" the nucleons and not their charge. Weak interaction also only "sees" a lepton and cannot distinguish between a neutrino and an electron (muon, tau). Exactly as for the nucleons, the weak interaction are invariant under rotation in the weak isospin space and the Lagrangian should be invariant under SU(2), the group of 2×2 unitary matrices with determinant one.

The underlying symmetry is therefore the $SU(2)$ one to be applied on left handed electrons, muons and taus. The similarity with QED however does not go further:

- now we must have three gauge bosons $W^\pm$ and Z^0 corresponding to charged current interaction during which a neutrino becomes an electron (or an anti-neutrino becomes a positron) and also to neutral current reactions where a neutrino does not have to become an electron.

- to ensure gauge invariance like the one we have for QED, the three weak gauge bosons $W^\pm$, Z^0 must be massless. This fact is disturbing as one knows that weak interactions are of short range, which means that the exchanged boson should be massive and out of the range of measurements of the sixties' experiments.

At this point, we need a break through which allows the W bosons to be massive whilst ensuring the gauge invariance. It was until the publication of the work of Peter Higgs, François Englert and Robert Brout on Spontaneous Symmetry Breaking (SSB) that this difficulties were overcome.

The Higgs mechanism

We recall that we deal with left handed lepton doublets

$$\psi_l = \begin{pmatrix} \nu_l \\ l^- \end{pmatrix}_L , \tag{1.4}$$

and that to realize invariance under local transformations, we had to introduce three gauge particles $W^\pm$ and W^0 which at this stage are massless. We use it and forget to account for the invariance under a phase transformation in the charged lepton wave function.

The idea here is to introduce a scalar doublet

$$\Phi = \begin{pmatrix} \phi^+ \\ \phi^0 \end{pmatrix} , \tag{1.5}$$

called the Higgs field (this Higgs field is neither a matter field nor a gauge field) and its interaction potential $V(\Phi)$. This potential has the shape of Mexican hat (see Figure 1.1). With this interaction potential, the energy is not minimum at zero values of the fields, but along a circle defined by

$$(\phi^+)^2 + (\phi^0)^2 = R^2 . \tag{1.6}$$

If we redefine the Higgs fields so that it is zero on the states of minimum of energy, the Lagrangian will still describe the same physics, but after this SSB the outcomes are

- the vector gauge bosons for the weak interaction, $W^\pm$ and Z^0, acquire their mass by absorbing the scalar fields, the $\phi^\pm$ and mixture of ϕ^0 and $\overline{\phi}^0$, respectively.

- the photon remains massless.
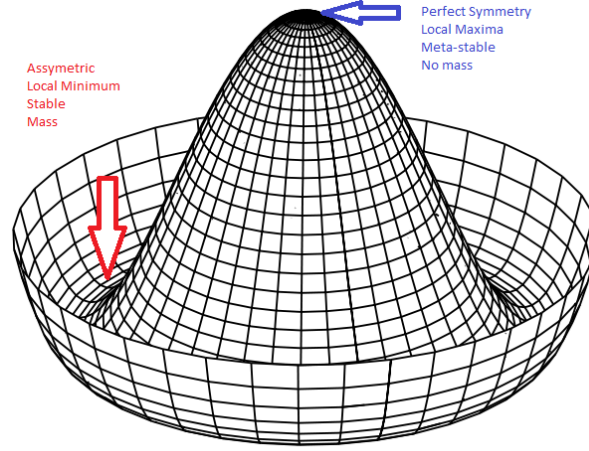
Figure 1.1: "Mexican hat" potential.

- the massive Higgs boson is the remaining mixture of ϕ^0 and $\overline{\phi}^0$.

Quantum Chromodynamics (QCD)

After the discovery that hadrons are made of spin-$\frac{1}{2}$ quarks and that baryons contain three valence quarks, one realizes that some combination of these three quarks do not obey the Pauli principle. The examples are the Δ^{++} and Ω^- which belong to the $J^P = (3/2)^+$ decuplet. Their wave function consists of at least three factors

$$\psi_{tot} = \psi_{space} \times \psi_{spin} \times \psi_{flavour} \ . \tag{1.7}$$

For the Δ^{++} or for the Ω^-, all quarks have the same flavour, so that $\psi_{flavour}$ is symmetric under the interchange of any two quarks. Because the Δ^{++} have the total spin-$\frac{3}{2}$, the orbital angular momentum is zero and the quarks' spins are all the same which mean that the quarks are placed symmetrically and that ψ_{space} is symmetric. Hence ψ_{tot} seems to violate the Pauli exclusion principle. To solve this problem, in 1964 Greenberg, Han and Nambu proposed that the quarks carry another quantum number which would allow to satisfy the demand of the Pauli principle. This quantum number is called "colour": there are three colours "red", "blue" and "green" which form the fundamental representation of the colour symmetry group $SU(3)_c$. Group algebra shows that the simplest colour multiplet which is anti-asymmetric is the colour singlet: all hadrons are then colour singlets.

The fundamental idea for QCD is that three "colour charges" of the quarks play the same role in the strong interaction as the electric charge does for the QED.

Now we can build a theory which is locally gauge invariant based on an internal symmetry group $SU(3)_c$. The quantum of the interaction are massless spin-1 gauge particle called gluons.

As these gluons couple to two colour states, *e.g.* to a quark and an anti-quark, the colour carried by the gluon must come from the combination of a colour triplet (red, blue and green) and an anti-colour triplet ($\overline{\text{red}}, \overline{\text{blue}}$ and $\overline{\text{green}}$).

In QED, the photon does not carry electric charge and can not interact with another photon. In QCD, the gluons do have colour charge and, hence, can interact among themselves directly. This has very important consequences on the confinement of the quarks inside the hadron.

In summary, the Standard Model gather weak and electromagnetic interaction and QCD. The underlying internal symmetry is

$$SU(3)_C \times SU(2)_L \times U(1)_Y . \tag{1.8}$$

1.2 The CKM matrix and the unitary triangle

1.2.1 The CKM matrix

In the SM, flavour-changing quark transitions are due to charged currents from the weak interaction in which the charged current operator J_μ couples to the W-boson according to the interaction Lagrangian [24].

$$\mathcal{L}_{int} = -\frac{g}{\sqrt{2}}(J_\mu W_\mu^+ + J_\mu^\dagger W_\mu^-) ,$$

and $W_\mu^\pm = \frac{1}{\sqrt{2}}(W_\mu^1 \mp W_\mu^2)$ in which $W_\mu^{1,2}$ are the weak bosons fields. The charged current which couples to a W^- boson is written as

$$J_\mu^\dagger = (\bar{u},\bar{c},\bar{t})_L \gamma_\mu (1-\gamma_5) \begin{pmatrix} d' \\ s' \\ b' \end{pmatrix} = (\bar{u},\bar{c},\bar{t})_L \gamma_\mu (1-\gamma_5) V_{CKM} \begin{pmatrix} d \\ s \\ b \end{pmatrix} , \tag{1.9}$$

where γ^μ are the Dirac matrices, the unitary 3×3 matrix V_{CKM} is the Cabibbo-Kobayashi-Maskawa (CKM) mixing matrix [25], [26]. It has been introduced in 1973 by Kobayashi and Maskawa to describe the *CP* violation with three quark generations. Similarly, the exchange of a W^+ boson is obtained using the hermitian conjugate. The $u, d, s, ...$ symbols

are here the Dirac spinors corresponding to the quarks. The CKM matrix connects the electroweak state (d',s',b') of the down-type quarks to their mass eigenstates (d,s,b)

$$
\begin{pmatrix} d' \\ s' \\ b' \end{pmatrix} = \begin{pmatrix} V_{ud} & V_{us} & V_{ub} \\ V_{cd} & V_{cs} & V_{cb} \\ V_{td} & V_{ts} & V_{tb} \end{pmatrix} \begin{pmatrix} d \\ s \\ b \end{pmatrix} = V_{\mathrm{CKM}} \begin{pmatrix} d \\ s \\ b \end{pmatrix} . \tag{1.10}
$$

The V_{ij} are coupling of quark transition from a down-type $(j = d, s, b)$ to an up-type quarks $(i = u, c, t)$.

In general, an $(n \times n)$ complex matrix will have $2n^2$ real parameters. However, the condition $\sum V_{ij} V_{jk}^* = \delta_{ik}$ gives n constrains for $i = k$ and $n(n-1)$ ones for $i \neq k$: the unitary condition reduces the number of independent parameters to n^2. With n generations, we are dealing with $2n$ quark fields for which we have the freedom to choose $2n - 1$ relative phases. Therefore, the number of independent parameters in the CKM matrix is

$$
n^2 - (2n - 1) = (n - 1)^2 .
$$

With two-generations $(n = 2)$, the 2×2 unitary matrix has only one real parameter chosen as the Cabibbo angle (θ_c). As the matrix is real, *CP* violation can not be accommodated from this mechanism.

With three generations of quarks and the CKM matrix being unitary, the matrix can be described completely by four independent parameters, which can be chosen as three Euler angles and one complex phase which is the only possible source of *CP* violation in SM.

1.2.2   Parametrization of the CKM matrix

There are many different ways to parametrize the CKM matrix. A convenient parametrization was introduced by Chau and Keung, and has is proposed in the review of particle physics [27]

$$
V_{\mathrm{CKM}} = \begin{pmatrix} c_{12}c_{13} & s_{12}c_{13} & s_{13}e^{-i\delta_{13}} \\ -s_{12}c_{23} - c_{12}s_{23}s_{13}e^{i\delta_{13}} & c_{12}c_{23} - s_{12}s_{23}s_{13}e^{i\delta_{13}} & s_{23}c_{13} \\ s_{12}s_{23} - c_{12}c_{23}s_{13}e^{i\delta_{13}} & -c_{12}s_{23} - s_{12}c_{23}s_{13}e^{i\delta_{13}} & c_{23}c_{13} \end{pmatrix} , \tag{1.11}
$$

where $c_{ij} \equiv \cos\theta_{ij}$, $s_{ij} \equiv \sin\theta_{ij}$, θ_{ij} being the Euler angles, *i.e.* the mixing angles between the generations i and j; the phase δ_{13} allows *CP* violation in the considered sector.

As $s_{13} = |V_{ub}| \simeq 0.003$, $c_{13} \simeq 1$ and $\sin\theta_{12} = \lambda \equiv \sin\theta_C$ where θ_C is the Cabibbo angle, one can define $\sin\theta_{23} = A\lambda^2$ and $\sin\theta_{13}e^{-i\delta_{13}} = A\lambda^3(\rho - i\eta)$ and get the useful parametrization of the CKM matrix proposed by Wolfenstein [28]

$$V_{\text{CKM}} = \begin{pmatrix} 1 - \frac{\lambda^2}{2} & \lambda & A\lambda^3(\rho - i\eta) \\ -\lambda & 1 - \frac{\lambda^2}{2} & A\lambda^2 \\ A\lambda^3(1 - \rho - i\eta) & -A\lambda^2 & 1 \end{pmatrix} + \delta_{V_{\text{CKM}}} \ , \qquad (1.12)$$

where $\delta_{V_{\text{CKM}}} = \mathcal{O}(\lambda^4)$.

In this parametrization, four independent parameters A, λ, ρ and η remain where A, ρ and η all are of order one. The higher order terms are important for the B_s^0 system, which is used at the order $\mathcal{O}(\lambda^5)$

$$\delta_{V_{\text{CKM}}} = \begin{pmatrix} -\frac{1}{8}\lambda^4 & 0 & 0 \\ \frac{1}{2}A^2\lambda^5(1 - 2(\rho + i\eta)) & -\frac{1}{8}\lambda^4(1 + 4A^2) & 0 \\ \frac{1}{2}A\lambda^5(\rho + i\eta) & \frac{1}{2}A\lambda^4(1 - 2(\rho + i\eta)) & -\frac{1}{2}A^2\lambda^4 \end{pmatrix} + \mathcal{O}(\lambda^6) \ . \quad (1.13)$$

1.2.3   The unitarity triangles

The unitarity of the CKM matrix

$$\sum_k V_{ki}V_{kj}^* = \delta_{ij} \qquad (1.14)$$

yields six orthogonal relations which can be represented as six "unitary triangles" in the complex plane. These triangles all have the same area.

These orthogonality relations are

$$\begin{aligned} (\textbf{ds}) \quad & V_{ud}V_{us}^* \ + \ V_{cd}V_{cs}^* \ + \ V_{td}V_{ts}^* = 0 \ , \\ (\textbf{sb}) \quad & V_{us}V_{ub}^* \ + \ V_{cs}V_{cb}^* \ + \ V_{ts}V_{tb}^* = 0 \ , \\ (\textbf{db}) \quad & V_{ud}V_{ub}^* \ + \ V_{cd}V_{cb}^* \ + \ V_{td}V_{tb}^* = 0 \ , \\ (\textbf{cu}) \quad & V_{ud}^*V_{cd} \ + \ V_{us}^*V_{cs} \ + \ V_{ub}^*V_{cb} = 0 \ , \\ (\textbf{tc}) \quad & V_{cd}^*V_{td} \ + \ V_{cs}^*V_{ts} \ + \ V_{cb}^*V_{tb} = 0 \ , \\ (\textbf{tu}) \quad & V_{ud}^*V_{td} \ + \ V_{us}^*V_{ts} \ + \ V_{ub}^*V_{tb} = 0 \ , \end{aligned} \qquad (1.15)$$

where the first three equations present the orthogonality of two different columns of the CKM matrix, and the last three two different rows.

Using the Wolfenstein expansion, there are only two triangles with the sides that are all of order λ^3

$$
\begin{aligned}
(\textbf{db}) \quad & V_{ud}V_{ub}^* \; + \; V_{cd}V_{cb}^* \; + \; V_{td}V_{tb}^* = 0 \; , \\
& \mathcal{O}(\lambda^3) \qquad \mathcal{O}(\lambda^3) \qquad \mathcal{O}(\lambda^3) \\
(\textbf{tu}) \quad & V_{ud}^*V_{td} \; + \; V_{us}^*V_{ts} \; + \; V_{ub}^*V_{tb} = 0 \; . \\
& \mathcal{O}(\lambda^3) \qquad \mathcal{O}(\lambda^3) \qquad \mathcal{O}(\lambda^3)
\end{aligned}
\tag{1.16}
$$

The other four triangles have sides with different powers of λ, hence, these triangles are "squashed".

The unitary triangle (**db**), used for B^0 system, plays a central role in the test of the CKM picture, because it is the easiest one to constrain via its angles, given the current experimental accuracy. In the B_s^0 system, the unitary triangle (**sb**) also need to be measured.

Dividing the three sides of the unitary triangle (**db**) and of the unitary triangle (**sb**) by $|V_{cd}V_{cb}^*|$ and $|V_{cs}V_{cb}^*|$, respectively yields new unitary triangle (**db**) and (**sb**) shown in Figure 1.2.

The angles in the unitary triangle (**db**) and (**sb**) are defined as follows

$$
\alpha = \arg\left[-\frac{V_{td}V_{tb}^*}{V_{ud}V_{ub}^*}\right] , \qquad\qquad \gamma = \arg\left[-\frac{V_{ud}V_{ub}^*}{V_{cd}V_{cb}^*}\right] ,
$$
$$
\beta = \arg\left[-\frac{V_{cd}V_{cb}^*}{V_{td}V_{tb}^*}\right] , \qquad\qquad \beta_s = \arg\left[-\frac{V_{ts}V_{tb}^*}{V_{cs}V_{cb}^*}\right] .
\tag{1.17}
$$

Sometimes a different convention of the Wolfenstein parameters is used which is denoted as $\bar{\rho}$ and $\bar{\eta}$. These parameters are defined as:

$$
\bar{\eta} = \eta(1 - \frac{\lambda^2}{2}) \;\; \text{and} \;\; \bar{\rho} = \rho(1 - \frac{\lambda^2}{2}) \; .
\tag{1.18}
$$

With this notation, the sides of the **db** unitary triangle are:

$$
|R_b| = \left|\frac{V_{ud}V_{ub}^*}{V_{cd}V_{cb}^*}\right| = \sqrt{\bar{\rho}^2 + \bar{\eta}^2} \; ,
$$
$$
|R_t| = \left|\frac{V_{td}V_{tb}^*}{V_{cd}V_{cb}^*}\right| = \sqrt{(1 - \bar{\rho})^2 + \bar{\eta}^2} \; ,
\tag{1.19}
$$

and the third side having an unit length.
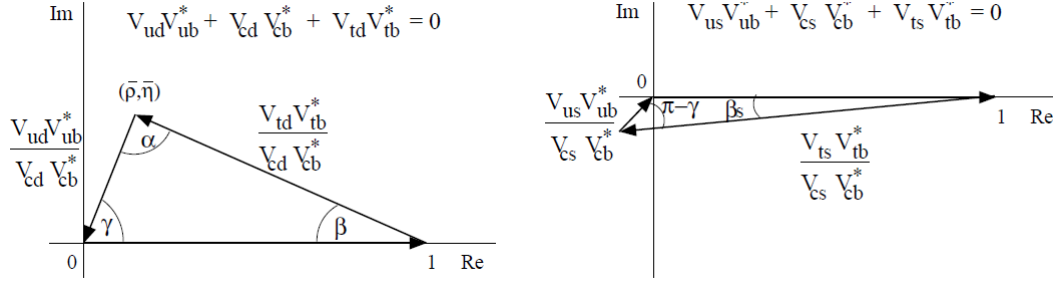
Figure 1.2: The unitary triangle (**db**) (left) for B^0 system and (**sb**) (right) for B_s^0 system.

1.2.4   Constraining the CKM matrix from measurements

The currently published magnitudes of the CKM matrix elements, the values obtained by averaging many experiments, are given by [9]

$$
\begin{pmatrix} |V_{ud}| & |V_{us}| & |V_{ub}| \\ |V_{cd}| & |V_{cs}| & |V_{cb}| \\ |V_{td}| & |V_{ts}| & |V_{tb}| \end{pmatrix} = \begin{pmatrix} 0.97427 \pm 0.00014 & 0.22536 \pm 0.00061 & 0.00355 \pm 0.00015 \\ 0.22522 \pm 0.00061 & 0.97343 \pm 0.00015 & 0.0414 \pm 0.0012 \\ 0.00886 \pm 0.00033 & 0.0405 \pm 0.0012 & 0.99914 \pm 0.00005 \end{pmatrix}.
$$

(1.20)

The results are consistent with the unitary relations

$$
|V_{ud}|^2 + |V_{us}|^2 + |V_{ub}|^2 = 0.9999 \pm 0.0006 \ ,
$$
$$
|V_{cd}|^2 + |V_{cs}|^2 + |V_{cb}|^2 = 1.024 \pm 0.032 \ ,
$$
$$
|V_{ud}|^2 + |V_{cd}|^2 + |V_{td}|^2 = 1.000 \pm 0.004 \ ,
$$
$$
|V_{us}|^2 + |V_{cs}|^2 + |V_{ts}|^2 = 1.025 \pm 0.032 \ .
$$

(1.21)

The current measurements of the unitary triangle (**db**) and (**sb**) angles including indirect and direct constraints are $\alpha = (90.4^{+2.0}_{-1.0})^\circ$, $\beta = (22.62^{+0.44}_{-0.42})^\circ$, $\gamma = (67.01^{+0.88}_{-1.99})^\circ$ and $\beta_s = (1.078^{+0.021}_{-0.024})^\circ$ [29]. The sum of the three angles of the unitary triangle (**db**), $\alpha + \beta + \gamma = (180.03 \pm 3)^\circ$, is also consistent with the SM expectation.

The combination of the experimental results and the constraints on the $(\bar{\rho}, \bar{\eta})$ and $(\bar{\rho}_{sb}, \bar{\eta}_{sb})$ planes for the unitary triangle (**db**) (left) and unitary triangle (**sb**) (right) respectively are shown in Figure 1.3. Note that the $\bar{\rho}_{sb}$ and $\bar{\eta}_{sb}$ coordinates are defined in the same way as $\bar{\rho}$ and $\bar{\eta}$ for the **sb** unitary triangle.
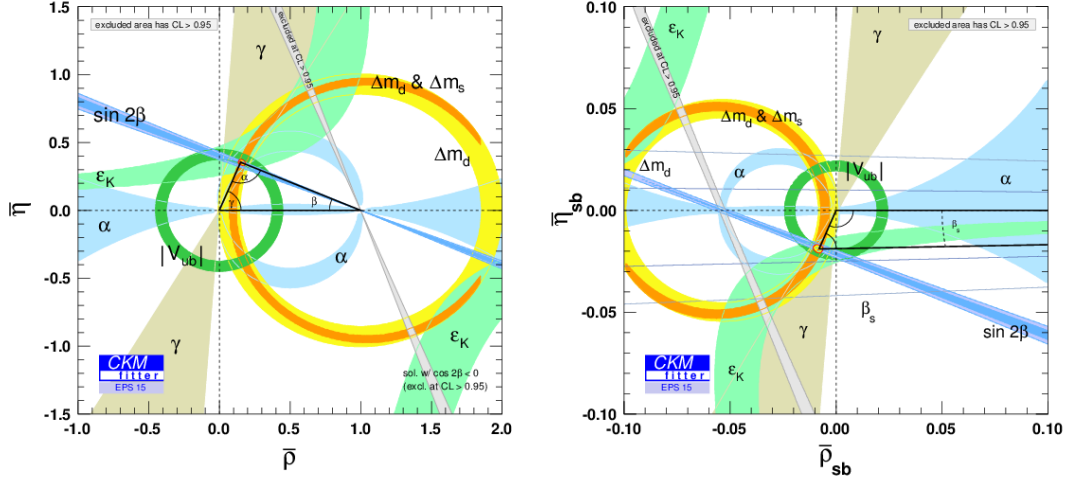
Figure 1.3: Constraints on the $(\overline{\rho}, \overline{\eta})$ plane (left) and the $(\overline{\rho}_s, \overline{\eta}_s)$ plane (right) as preliminary results of Summer 2015 [29].

1.3 Neutral *B* meson system

In this section we derive the quantum formalism to describe the neutral *B* mesons mixing, and we introduce three types of *CP* violation such as *CP* violation in decay, *CP* violation in mixing and *CP* violation in the interference between decay and mixing.

1.3.1 Neutral *B* meson mixing

Due to weak interactions, the transitions $B_q^0 \rightarrow \overline{B}_q^0$ and $\overline{B}_q^0 \rightarrow B_q^0$ ($q \in d, s$) are allowed. This mixing process happens through the box diagrams shown in Figure 1.4.

Let us start at time $t = 0$ in the $(B_q^0, \overline{B}_q^0)$ system: at this time ($t = 0$) these particles
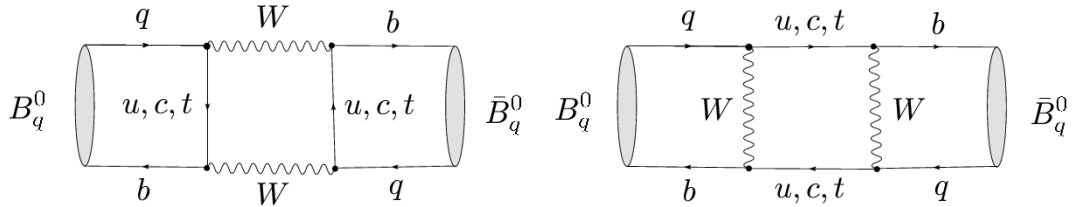
Figure 1.4: Box diagrams for the $B_q^0 \rightarrow \overline{B}_q^0$ transitions ($q \in d, s$).

have definite flavour; but for $t > 0$, weak interaction come into play and B_q^0 oscillate to $\overline{B}_q^0$ and vice versa according to Figure 1.4. Starting with a B_q^0 (or a $\overline{B}_q^0$), it develops in

the subspace defined by $|B_q^0\rangle$ and $|\overline{B}_q^0\rangle$

$$\psi(t) = a(t)|B_q^0\rangle + b(t)|\overline{B}_q^0\rangle \ , \tag{1.22}$$

where $a(t)$ and $b(t)$ are time-independent coefficients.

The wave function $\psi(t)$ must satisfy the Schrödinger equation

$$i\frac{\partial\psi(t)}{\partial t} = \mathbf{H}_{\text{eff}}\psi(t) \ , \tag{1.23}$$

where $\mathbf{H}_{\text{eff}}$ is the effective Hamiltonian governs the time evolution. Equation (1.23) can be rewritten as

$$i\frac{\partial}{\partial t}\begin{pmatrix} a(t) \\ b(t) \end{pmatrix} = \begin{pmatrix} M_{11} - \frac{i}{2}\Gamma_{11} & M_{12} - \frac{i}{2}\Gamma_{12} \\ M_{21} - \frac{i}{2}\Gamma_{21} & M_{22} - \frac{i}{2}\Gamma_{22} \end{pmatrix}\begin{pmatrix} a(t) \\ b(t) \end{pmatrix}$$
$$= \left(\mathbf{M} - \frac{i}{2}\mathbf{\Gamma}\right)\begin{pmatrix} a(t) \\ b(t) \end{pmatrix} \ , \tag{1.24}$$

where the 2×2 matrices $\mathbf{M}$ and $\mathbf{\Gamma}$ are often referred to as the mass and decay matrices. Both $\mathbf{M}$ and $\mathbf{\Gamma}$ are Hermitian matrices while $\mathbf{H_{eff}}$ is not Hermitian. This would open the way to mixing ans *CP* violation.

If now we assume that *CPT* is conserved then it follow that $M_{11} = M_{22}$, $M_{21} = M_{12}^*$ and $\Gamma_{11} = \Gamma_{22}$, $\Gamma_{21} = \Gamma_{12}$ meaning that mass and total decay width of particle and anti-particle are identical. The effective Hamiltonian becomes

$$\mathbf{H}_{\text{eff}} = \begin{pmatrix} M - \frac{i}{2}\Gamma & M_{12} - \frac{i}{2}\Gamma_{12} \\ M_{12}^* - \frac{i}{2}\Gamma_{12}^* & M - \frac{i}{2}\Gamma \end{pmatrix} \ . \tag{1.25}$$

The diagonal elements M of the mass matrix are dominated by the eigenvalue m_0 of the unperturbed Hamiltonian $(H_{\text{st}} + H_{\text{em}})$[1] which contains information on the quark masses and the strong interaction that bind the quarks into the mesons. The off-diagonal elements of the mass matrix, M_{12} and M_{21}, contributes to the transition amplitude from B_q^0 to $\overline{B}_q^0$ and $\overline{B}_q^0$ to B_q^0 via virtual intermediate states. In the SM these transitions correspond to second order term with respect to the weak interaction coupling constant expansion.

The off-diagonal elements of the decay matrix, Γ_{12} and Γ_{21}, are due to transition $\overline{B}_q^0 \to f \to B_q^0$ and $B_q^0 \to f \to \overline{B}_q^0$, where f is an on-shell intermediate state. The

---

[1]H_{st} and H_{em} being the Hamiltonians of strong and electromagnetic interactions.

diagonal elements Γ of the decay matrix are due to all allowed decay $B_q^0 \to f$ and $\overline{B}_q^0 \to f$.

With these assumption we will find the eigenvalues and eigenstates of the Hamiltonian. These will describe the masses and decay width and the linear combination of B_q^0 and $\overline{B}_q^0$ that describes the physical particles.

Mass eigenstates

To obtain the "physical" eigenstates, we must diagonalize the effective Hamiltonian. Once this is done, the eigenstates of Schödinger Equation (1.24) are the mass eigenstates defined as

$$|B_{H,L}\rangle = p|B_q^0\rangle \mp q|\overline{B}_q^0\rangle \ , \tag{1.26}$$

with the normalization condition $|q|^2 + |p|^2 = 1$, where p and q are complex coefficients and H and L stand for heavy and light respectively. They are eigenstates of H_{em} and correspond to two eigenvalues that can be written as

$$\lambda_{H,L} = m_{H,L} - \frac{i}{2}\Gamma_{H,L} \ . \tag{1.27}$$

The mass difference Δm and the width difference $\Delta\Gamma$ between the neutral B mesons are defined as follows:

$$\Delta m = m_H - m_L > 0, \qquad \Delta\Gamma = \Gamma_L - \Gamma_H \ . \tag{1.28}$$

By solving the equation

$$\begin{pmatrix} M - \frac{i}{2}\Gamma & M_{12} - \frac{i}{2}\Gamma_{12} \\ M_{12}^* - \frac{i}{2}\Gamma_{12}^* & M - \frac{i}{2}\Gamma \end{pmatrix} \begin{pmatrix} p \\ \pm q \end{pmatrix} = \lambda_{L,H} \begin{pmatrix} p \\ \pm q \end{pmatrix}, \tag{1.29}$$

one can find constraints for p and q as

$$\frac{q}{p} = \sqrt{\frac{M_{12}^* - \frac{i}{2}\Gamma_{12}^*}{M_{12} - \frac{i}{2}\Gamma_{12}}} \ . \tag{1.30}$$

Note that we have chosen $\Delta m > 0$. With our choice, Γ_L and Γ_H correspond to the long-lived and short-lived B mesons, $\Delta\Gamma$ is expected to be positive in the SM.

From Equation (1.26) we can rewrite the B_q^0 and $\overline{B}_q^0$ states as

$$|B_q^0\rangle = \frac{1}{2p}[|B_H\rangle + |B_L\rangle] ,$$
$$|\overline{B}_q^0\rangle = \frac{1}{2q}[|B_H\rangle - |B_L\rangle] . \tag{1.31}$$

Time evolution

The evolution of the mass eigenstates $|B_H\rangle$ and $|B_L\rangle$, starting from a state at $t = 0$ is governed by

$$|B_L(t)\rangle = e^{-im_L t - \frac{1}{2}\Gamma_L t}|B_L\rangle ,$$
$$|B_H(t)\rangle = e^{-im_H t - \frac{1}{2}\Gamma_H t}|B_H\rangle . \tag{1.32}$$

Combining Equations (1.26), (1.31) and (1.32) we obtain

$$|B_q^0(t)\rangle = g_+(t)|B_q^0\rangle + \frac{q}{p}g_-(t)|\overline{B}_q^0\rangle ,$$
$$|\overline{B}_q^0(t)\rangle = g_+(t)|\overline{B}_q^0\rangle + \frac{p}{q}g_-(t)|B_q^0\rangle , \tag{1.33}$$

where

$$g_\pm(t) = \frac{1}{2}\left[e^{-i(m_L - \frac{i}{2}\Gamma_L)t} \pm e^{-i(m_H - \frac{i}{2}\Gamma_H)t}\right] . \tag{1.34}$$

Thus, the probability to measure the state $|\overline{B}_q^0\rangle$ at time t after the state $|B_q^0\rangle$ was produced is

$$|\langle\overline{B}_q^0|B_q^0(t)\rangle|^2 = |g_-(t)|^2 \left|\frac{q}{p}\right|^2 , \tag{1.35}$$

with

$$|g_\pm(t)|^2 = \frac{e^{-\Gamma t}}{2}\left(\cosh\frac{\Delta\Gamma t}{2} \pm \cos\Delta m t\right) . \tag{1.36}$$

Figure 1.5 shows the oscillation probability of B^0 (left) and B_s^0 (right). Since the mass eigenstates B_H and B_L of B_d^0 happen to have almost equal lifetimes, $\Delta\Gamma_{B^0} = 0$ and since $\Delta m_d \sim m_t^2|V_{tb}V_{td}|^2 \sim m_t^2\lambda^6$ (m_t is the mass of the top quark) is small, we can see the sum of the B^0 and $\overline{B}^0$ distributions (left) have the shape of exponential distribution. On other hand $\Delta m_s \sim m_t^2|V_{tb}V_{ts}|^2 \sim \frac{1}{\lambda^2}\Delta m_d$, then B_s^0 oscillation (right) is about 35
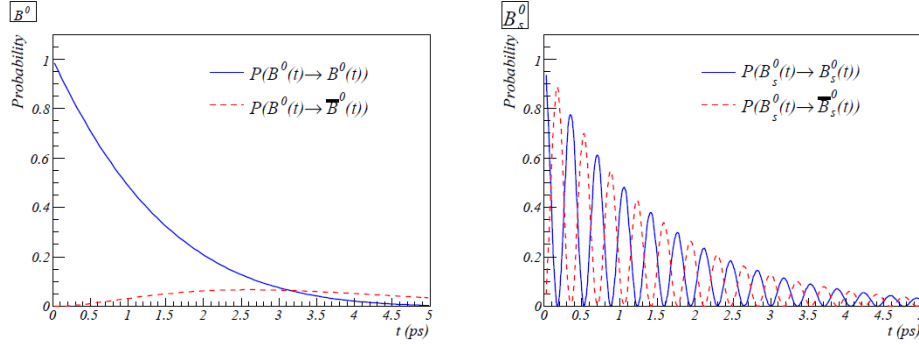
times faster than B^0 oscillation. In the absence of *CP* violation in mixing, $|q/p| = 1$, the time-integrated mixing probability is defined as

$$\chi_q = \frac{\int |g_-(t)|^2 dt}{\int |g_-(t)|^2 dt + \int |g_+(t)|^2 dt} = \frac{x_q^2 + y_q^2}{2(x_q^2 + 1)} \; ,$$

$$\text{where} \quad x_q = \frac{\Delta m_q}{\Gamma_q}, \qquad y_q = \frac{\Delta \Gamma_q}{2\Gamma_q} \; . \tag{1.37}$$

The oscillation parameters of the neutral B mesons, B^0 and B_s^0, are summarized in Table 1.3 [9].

Figure 1.5: Probability for a bottom meson produced as B_q^0 to decay as B_q^0 or $\overline{B}_q^0$ for the B^0 system (left) and the B_s^0 system (right) [30].

Parameter	B^0	B_s^0
$\Delta m \; (\mathrm{ps}^{-1})$	0.510 ± 0.003	17.761 ± 0.021
$\Delta m / \Gamma$	0.774 ± 0.006	26.85 ± 0.13
$\Delta \Gamma / \Gamma$	$(0.1 \pm 1.0)\%$	$(13.8 \pm 1.2)\%$

Table 1.3: Oscillation parameters of the neutral mesons B^0 and B_s^0 [9].

1.3.2   Decay rates

We now consider the B^0 meson decays into a final state f. The two decay amplitudes corresponding to $\overline{B}_q^0$ and $\overline{B}_q^0$ decays to the final state f are defined as

$$A_f = \langle f|T|B_q^0 \rangle, \qquad \overline{A}_f = \langle f|T|\overline{B}_q^0 \rangle \; , \tag{1.38}$$

where T is the transition matrix.

The general expression for the time-dependent decay rate of a $|B_q^0\rangle$ born at time $t = 0$ and evolving until time t of its decay according to equation (1.33) is

$$\Gamma_{B_q^0 \to f}(t) = |\langle f|T|B_q^0(t)\rangle|^2 = |g_+(t)A_f + \frac{q}{p}g_-(t)\overline{A}_f|^2 \ . \tag{1.39}$$

Similarly, the decay rate of a $|\overline{B}_q^0\rangle$ born at time $t = 0$ is

$$\Gamma_{\overline{B}_q^0 \to f}(t) = |\langle f|T|\overline{B}_q^0(t)\rangle|^2 = |g_+(t)\overline{A}_f + \frac{p}{q}g_-(t)A_f|^2 \ . \tag{1.40}$$

Noting by $\overline{f}$ the $\mathcal{C}'_{conjugate}$ state of f, all the possible decay rates can be written as

$$\Gamma_{B^0 \to f}(t) = |A_f|^2 \left(|g_+(t)|^2 + |\lambda_f|^2|g_-(t)|^2 + 2\Re[\lambda_f g_+^*(t)g_-(t)]\right) \ ,$$

$$\Gamma_{B^0 \to \overline{f}}(t) = |\overline{A}_{\overline{f}}|^2 \left|\frac{q}{p}\right|^2 \left(|g_-(t)|^2 + |\overline{\lambda}_{\overline{f}}|^2|g_+(t)|^2 + 2\Re[\overline{\lambda}_{\overline{f}} g_+(t)g_-^*(t)]\right) \ ,$$

$$\Gamma_{\overline{B}^0 \to f}(t) = |A_f|^2 \left|\frac{p}{q}\right|^2 \left(|g_-(t)|^2 + |\lambda_f|^2|g_+(t)|^2 + 2\Re[\lambda_f g_+(t)g_-^*(t)]\right) \ ,$$

$$\Gamma_{\overline{B}^0 \to \overline{f}}(t) = |\overline{A}_{\overline{f}}|^2 \left(|g_+(t)|^2 + |\overline{\lambda}_{\overline{f}}|^2|g_-(t)|^2 + 2\Re[\overline{\lambda}_{\overline{f}} g_+^*(t)g_-(t)]\right) \ , \tag{1.41}$$

where

$$\lambda_f = \frac{q}{p}\frac{\overline{A}_f}{A_f} \ , \qquad \lambda_{\overline{f}} = \frac{q}{p}\frac{\overline{A}_{\overline{f}}}{A_{\overline{f}}} \ , \quad \text{and} \quad \overline{\lambda}_{\overline{f}} = \frac{1}{\lambda_{\overline{f}}} \ , \tag{1.42}$$

and

$$|g_\pm(t)|^2 = \frac{1}{2}e^{-\Gamma t}\left(\cosh\frac{\Delta\Gamma t}{2} \pm \cos\Delta mt\right) \ ,$$

$$g_+^*(t)g_-(t) = \frac{1}{2}e^{-\Gamma t}\left(\sinh\frac{\Delta\Gamma t}{2} + i\sin\Delta mt\right) \ , \tag{1.43}$$

$$g_+(t)g_-^*(t) = \frac{1}{2}e^{-\Gamma t}\left(\sinh\frac{\Delta\Gamma t}{2} - i\sin\Delta mt\right) \ ."$$

1.4   *CP* Violation in *B* meson decays

There are three possible manifestation of *CP* symmetry violation within the B^0 meson system and they can be classified in a model-independent way as follows [31]

1. *CP* violation in decay (also call direct *CP* violation): it occurs in both charged and neutral system, when a decay and its *CP* eigenstate process have different

amplitude.

2. *CP* violation in mixing (also called indirect *CP* violation): it occurs when the $B_q^0 \to \overline{B}_q^0$ transition is not the same as the $\overline{B}_q^0 \to B_q^0$ transition.

3. *CP* violation in the interference between mixing and decays: it occurs in a decay to a final state that is common to B_q^0 and $\overline{B}_q^0$ meson, where B_q^0 can decay to the final state f directly ($B_q^0 \to f$) or after having oscillated ($B_q^0 \to \overline{B}_q^0 \to f$).

Let us present now in more details the above *CP* violation possibilities.

1.4.1 *CP* Violation in decays

To study this type of *CP* violation, the quantity $|\frac{\overline{A}_{\overline{f}}}{A_f}|$ is considered since it is independent of phases convention and physically meaningful. A_f ($\overline{A}_{\overline{f}}$) is the amplitude of B_q^0 ($\overline{B}_q^0$) which decays into a final state f ($\overline{f}$). There are two type of phases that can appear in A_f and $\overline{A}_{\overline{f}}$:

- The weak phases: they contribute to the amplitude A_f and $\overline{A}_{\overline{f}}$ with opposite signs. These phases appear in the CKM matrix in the SM.

- The strong phase: comes from the possible contribution related to strong interactions. Since strong interaction conserve *CP*, these phases appear in A_f and $\overline{A}_{\overline{f}}$ with the same sign.

We now can factorize each contribution to the amplitudes in three parts: the magnitude A_i, the weak phase terms $e^{i\phi_i}$ and the strong terms $e^{i\delta_i}$. Then if several amplitudes contribute to $B_q^0 \to f$, the amplitude A_f and $\overline{A}_{\overline{f}}$ are given by

$$A_f = \sum_i A_i e^{i(\delta_i + \phi_i)} \ , \qquad \overline{A}_{\overline{f}} = \sum_i A_i e^{i(\delta_i - \phi_i)} \ . \qquad (1.44)$$

The amplitude ratio is then

$$\left| \frac{\overline{A}_{\overline{f}}}{A_f} \right| = \left| \frac{\sum_i A_i e^{i(\delta_i - \phi_i)}}{\sum_i A_i e^{i(\delta_i + \phi_i)}} \right| \ . \qquad (1.45)$$

In the case where all weak phase ϕ_i are the same or where all the strong phase δ_i are the same, then *CP* is conserved in decay, $|\frac{\overline{A}_{\overline{f}}}{A_f}| = 1$. If both the weak phase and the strong

phase are different one from the other then *CP* is violated in decays with the condition

$$\left| \frac{\overline{A}_{\overline{f}}}{A_f} \right| \neq 1 \quad \Rightarrow \quad CP \text{ violation.} \tag{1.46}$$

Conclusion: for *CP* violation in decays (direct *CP* violation) to be apparent, one needs at least two amplitudes which differ by their weak phases and by a strong phase which remain invariant under *CP* transformation.

An example of *CP* violation in decay is shown in the flavour specific decay $B^0 \rightarrow K^+\pi^-$ where several amplitudes (isospin and penguin contribution) are present. A *CP* asymmetry has been observed in the processes $B^0 \rightarrow K^+\pi^-$ and its *CP* conjugate $\overline{B}^0 \rightarrow K^-\pi^+$ [32]

$$
\begin{aligned}
A_{K\pi} &= \frac{\Gamma(\overline{B}^0 \rightarrow K^+\pi^-) - \Gamma(B^0 \rightarrow K^+\pi^-)}{\Gamma(\overline{B}^0 \rightarrow K^+\pi^-) + \Gamma(B^0 \rightarrow K^+\pi^-)} \\
&= -0.080 \pm 0.007(\text{stat}) \pm 0.003(\text{syst}) \ .
\end{aligned} \tag{1.47}
$$

1.4.2 *CP* Violation in mixing

Consider Equation (1.30) which is independent of any phase convention

$$\left| \frac{q}{p} \right|^2 = \left| \frac{M_{12}^* - \frac{i}{2}\Gamma_{12}^*}{M_{12} - \frac{i}{2}\Gamma_{12}} \right| \ . \tag{1.48}$$

If *CP* is conserved, $M_{12} = M_{12}^*$ and $\Gamma_{12} = \Gamma_{12}^*$ implying that M_{12} and Γ_{12} are real the quantity $|q/p| = 1$.

If *CP* is violated

$$\left| \frac{q}{p} \right| \neq 1 \quad \Rightarrow \quad CP \text{ Violation.} \tag{1.49}$$

This is *CP* violation in mixing. It arises because the mass eigenstates are different from the *CP* eigenstates. *CP* violation in mixing has been observed in the neutral Kaon system.

To measure experimentally this kind of *CP* violation for the neutral *B* mesons, one can study the semi-leptonic decays (where a positive charged lepton identifies a B_q^0 and a

negative charged lepton identifies a $\overline{B}_q^0$). The semi-leptonic asymmetry is defined as

$$A_{SL} = \frac{N(\overline{B}_q^0(t) \to l^+ \nu_l X) - N(\overline{B}^0(t) \to l^- \overline{\nu}_l X)}{N(\overline{B}_q^0(t) \to l^+ \nu_l X) + N(\overline{B}^0(t) \to l^- \overline{\nu}_l X)} \simeq 1 - \left| \frac{q}{p} \right| . \tag{1.50}$$

The combined value as measured at the *B*-factories yields [33]

$$A_{SL}^d = -0.0009 \pm 0.0021, \quad \text{or} \quad \left| \frac{q}{p} \right|_d = 1.0005 \pm 0.0011 \ ,$$

$$A_{SL}^s = -0.0077 \pm 0.0042, \quad \text{or} \quad \left| \frac{q}{p} \right|_s = 1.0039 \pm 0.0021 \ .$$

Thus, no *CP* violation in mixing is observed in the neutral *B* mesons.

1.4.3 *CP* Violation in the interference between mixing and decay

Let us consider the neutral *B* mesons decay to the final state f which is eigenstate of *CP*. This state is accessible from both B_q^0 and $\overline{B}_q^0$ decays. Even, one can still observe *CP* violation if $\Im \left(\frac{q}{p} \cdot \frac{\overline{A}_f}{A_f} \right) \neq 0$ (equation (1.42)). We now represent the time-dependent decay rate for the neutral *B* mesons (see section 1.3.2), $B_q^0(t) \to f$ and $\overline{B}_q^0(t) \to f$. By combining Equation (1.42) and (1.43), the decay rates can be rewritten as

$$\Gamma_{B_q^0 \to f}(t) = |A_f|^2 (1 + |\lambda_f|^2) \frac{e^{-\Gamma t}}{2} \left(\cosh \frac{\Delta \Gamma t}{2} + D_f \sinh \frac{\Delta \Gamma t}{2} + C_f \cos \Delta m t - S_f \sin \Delta m t \right) ,$$

$$\Gamma_{\overline{B}_q^0 \to f}(t) = |A_f|^2 \left| \frac{q}{p} \right|^2 (1 + |\lambda_f|^2) \frac{e^{-\Gamma t}}{2} \left(\cosh \frac{\Delta \Gamma t}{2} + D_f \sinh \frac{\Delta \Gamma t}{2} - C_f \cos \Delta m t + S_f \sin \Delta m t \right) ,$$

$$\tag{1.51}$$

with

$$D_f = \frac{2 \Re \lambda_f}{1 + |\lambda_f|^2} \ , \quad C_f = \frac{1 - |\lambda_f|^2}{1 + |\lambda_f|^2} \ , \quad S_f = \frac{2 \Im \lambda_f}{1 + |\lambda_f|^2} \ . \tag{1.52}$$

If we consider that $|q/p| = 1$ and use Equation (1.51), the time-dependent *CP* asymmetry is given by

$$A_f(t) = \frac{\Gamma(B_q^0 \to f) - \Gamma(\overline{B}_q^0 \to f)}{\Gamma(B_q^0 \to f) + \Gamma(\overline{B}_q^0 \to f)} = \frac{C_f \cos \Delta m t - S_f \sin \Delta m t}{\cosh \frac{\Delta \Gamma t}{2} + D_f \sinh \frac{\Delta \Gamma t}{2}} \ . \tag{1.53}$$

If the *CP* violation in decays is absent, $|\overline{A}_f| = |A_f|$ then $D_f = \Re\lambda_f$, $C_f = 0$ and $S_f = \Im\lambda_f$, the asymmetry reduces to

$$A_f(t) = \frac{-\Im\lambda_f \sin\Delta mt}{\cosh\frac{\Delta\Gamma t}{2} + \Re\lambda_f \sinh\frac{\Delta\Gamma t}{2}} \ . \tag{1.54}$$

So that one can still observe *CP* violation even if the *CP* violation in decay and mixing are not present when the following condition is satisfied

$$\Im\lambda_f = \Im\left(\frac{q}{p}\frac{\overline{A}_f}{A_f}\right) \neq 0 \ . \tag{1.55}$$

This is called *CP* violation in the interference between mixing and decay.

CP violation in the interference between decay and mixing occurs in the so-called gold plated channels $B^0 \rightarrow J/\psi K_{\mathrm{S}}^0$ and $B_s^0 \rightarrow J/\psi\phi$. Both decays proceed via $b \rightarrow c\bar{c}s$ transition to a common eigenstate either directly or after having oscillated. The phases that can be determined via the measurement of the *CP* asymmetry are (Equation 1.17)

$$\begin{aligned}
\text{for } B^0 \ : \quad & \beta = \arg\left[-\frac{V_{cd}V_{cb}^*}{V_{td}V_{tb}^*}\right] \text{ and} \\
\text{for } B_s^0 \ : \quad & \beta_s = \arg\left[-\frac{V_{ts}V_{tb}^*}{V_{cs}V_{cb}^*}\right] \ .
\end{aligned} \tag{1.56}$$

The lasted LHCb results give

$$\sin(2\beta) = 0.731 \pm 0.035(\text{stat}) \pm 0.020(\text{syst}) \ [34] \ , \tag{1.57}$$

$$\phi_s = -2\beta_s = -0.058 \pm 0.049(\text{stat}) \pm 0.006(\text{syst})[\text{rad}] \ [35] \ . \tag{1.58}$$

Chapter 2

The LHCb experiment

2.1 The LHC

The Large Hadron Collider (LHC) [36] is a large superconducting hadron accelerator and collider located underground at the Swiss-French border at the European Organization for Nuclear Research, known as CERN near Geneva, Switzerland. It was constructed from 2000 to 2008 in the circular underground tunnel of 27 km of the old Large Electron-Positron Collider (LEP) which operated very successfully from 1989 to 2000 before being decommissioned to build the LHC. The machine was designed for pp collisions at a centre-of-mass energy can go up to 14 TeV and a design luminosity of $\mathcal{L} = 1 \times 10^{34} \, \mathrm{cm}^{-2} \, \mathrm{s}^{-1}$. Two beams of protons are accelerated and shaped into bunches. At nominal configuration, each beam have 2808 bunches, with $\sim 10^{11}$ protons per bunch. The magnetic fields to hold the beams in orbit are supplied by superconducting magnets cooled down to 1.9 K and operating at a nominal magnetic field strength of 8.34 T. The collisions occur in eight interaction points, where the two bunches cross each other, four of which correspond to the positions of the four major particle detectors. ATLAS [37] and CMS [38] are general purpose experiments, mainly designed to search for the Higgs boson and for direct evidence of physics beyond the Standard Model. The LHCb experiment [39] is designed for the study on beauty and charm physics, especially for the precise measurements of CP violation. The ALICE experiment [40] will operate during dedicated heavy-ion runs (*e.g.* Pb-Pb or p-Pb) to study the behavior of nuclear matter in extreme conditions and the formation of quark-gluon plasma. The others three experiments are LHCf, MoEDAL and TOTEM.

The LHC collected data at a center-of-mass energy of 7 TeV in 2010-2011; the energy was increased to 8 TeV in 2012. Before being injected into the main ring, the beams
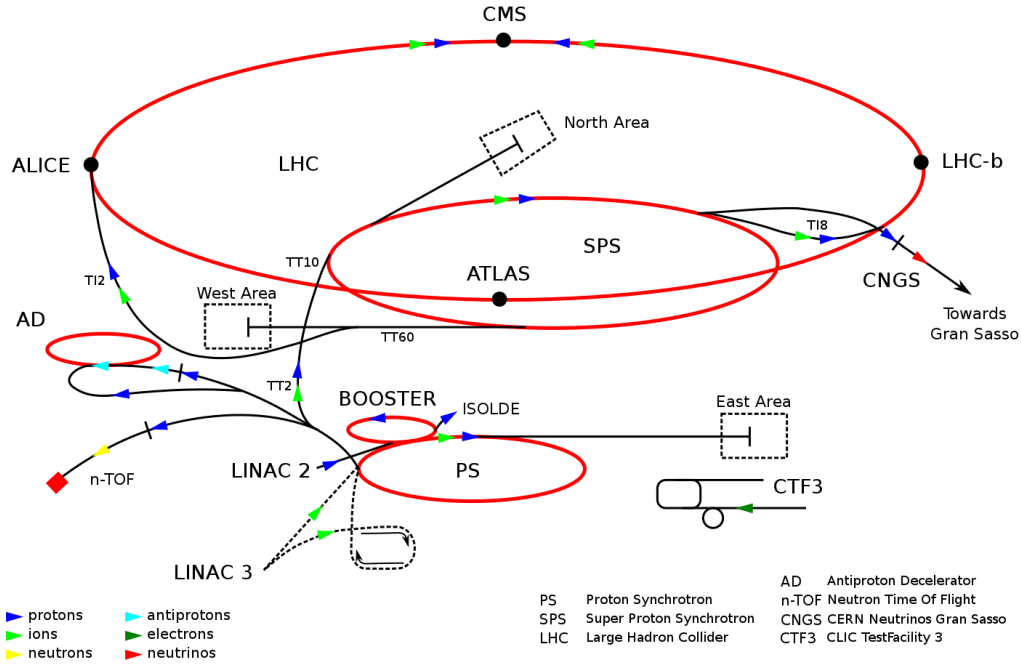
Figure 2.1: Layout of the LHC accelerator complex.

have been accelerated via a series of different system. First, protons are accelerated by the linear accelerator (LINAC) at the energy of 50 MeV, from which they are injected into the Proton Synchrotron Booster (PBS) to acquire an energy of 1 GeV. Next, they travel to the Proton Synchrotron (PS) and Super Proton Synchrotron (SPS) where they are accelerated to the energies of 26 GeV and 450 GeV, respectively, before injected into the LHC. The LHC then accelerates the protons to the desired collision energy.

2.2 The LHCb experiment

The LHCb experiment [39] is dedicated to studying CP-violation in the b and c sectors as well as precision measurements of Standard Model observables. As the production of $b\bar{b}$ pair has a large cross-section in the forward or backward directions, LHCb has been designed as a single-arm forward spectrometer with an acceptance of 10-300 mrad in the horizontal plane and 10-250 mrad vertical plane. This corresponds to a pseudo-rapidity region $2 < \eta < 5$, where pseudo-rapidity η is defined as $\eta = -\log(\tan\frac{\theta}{2})$, θ being the angle between the particle momentum and the beam axis. The detector, illustrated in Figure 2.2, is composed of several layers of sub-detectors each having a specific purpose, they will be discussed in the following sections.
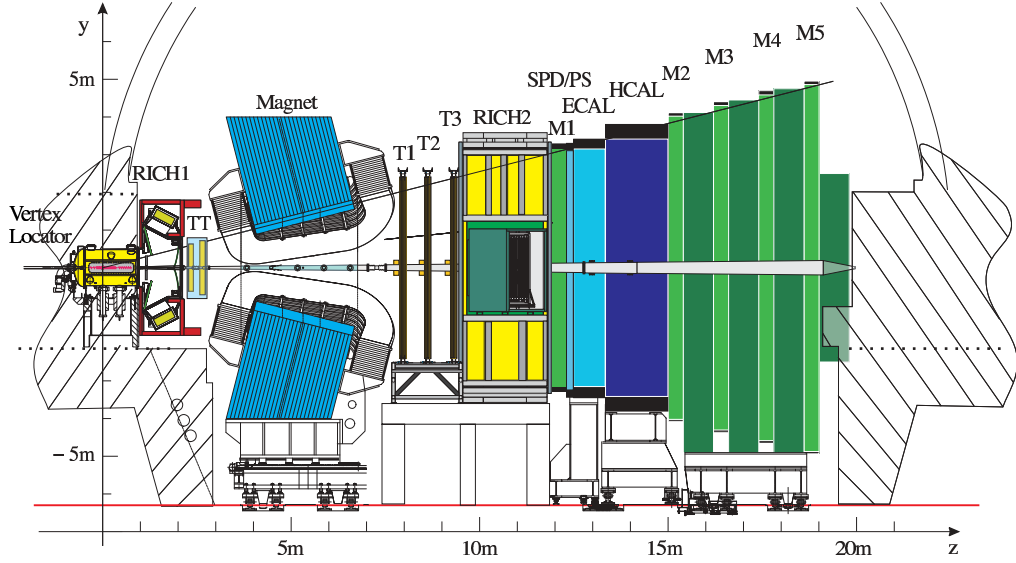
Figure 2.2: The LHCb detector layout.

The first successful *pp* collisions were recorded in December 2009 at the centre-of-mass energy of $\sqrt{s} = 900$ GeV. In 2010 and 2011 data were recorded at $\sqrt{s} = 7$ TeV and at $\sqrt{s} = 8$ TeV in 2012. The integrated luminosities collected in LHCb during the three years of running are summarized in Table 2.1

Years	Integrated Lumi. $\left(\text{fb}^{-1}\right)$	Center-of-mass energy
2010	0.04	7 TeV
2011	1.10	7 TeV
2012	2.08	8 TeV

Table 2.1: Summary of the integrated luminosity in LHCb during the three years of LHC running [41].

2.2.1 The VELO

The LHCb VErtex LOcator (VELO) [42] is built around the *pp* interaction point. It provides precise measurements of track coordinates close to the interaction region. These in turn are used to reconstruct the production and decay vertices of beauty and charm hadrons in order to provide an accurate measurement of their proper time and to measure the impact of the particles. The VELO, based on the silicon micro-strip technology, consists of 21 stations positioned perpendicular to the direction of the beam axis with a distance of 4 cm between them. Each station is divided in two independent halves which consists of two types of 300 μm thick sensors: the *r*-sensors to measure the radial

coordinate r and the ϕ-sensors to measure the azimuthal angle ϕ. All modules of the VELO are designed to be retractable. This allows the sensors to be located far enough to avoid the very high radiation hazard during the beam injection and ramping and to be close enough to the interaction point during data taking. In the opened position, each half station retracts by 3 cm. In closed position, the first silicon strips are at 8 mm from the beam and one halve is shifted along z by 1.5 cm relative to the opposite halve in order to ensure full azimuthal coverage. The fully opened and closed position are illustrated in Figure 2.3. The sensors are located inside a vacuum vessel which is separated from the machine vacuum by a corrugated aluminium foil which also sets as a RF shield. Two special stations of the VELO, so-called pile-up sensors, each consists of two r-sensor modules, are located upstream of the interaction point in order to quickly determine the number of primary vertices that can be used in the first level of trigger. In fact, these pile-up VETO stations are not currently used by the experiment.

The LHCb VELO performance results based on 2011 data have been reported in Reference [43]. The best single hit resolution of 4 μm is achieved. A primary vertex resolution of 13 μm in the transverse plane and 71 μm along the beam axis is achieved for vertices with 25 tracks. Figure 2.4 shows plot of the Impact Parameter (IP) resolution of the x coordinate versus $1/p_\mathrm{T}$ and compared with simulation. As we can see they are asymptotic at high p_T tending to 12 μm and an IP resolution of less than 35 μm is archived for tracks with transverse momentum greater than 1 GeV/c.

2.2.2   The magnet

The large dipole magnet [44], placed right after Tracker Turicensis (see Section 2.2.3) is intended to bend the tracks of charged particles and allow the measurement of their momentum by the tracking system. The tracking system provides momentum measurement for charged particles with a momentum resolution $\delta p/p = 0.4\%$ for momenta up to 200 GeV/c. An integrated field of 4 Tm for tracks originating near the primary interaction point is therefore needed.

The LHCb magnet is quite large, the total weight of the yoke is 1500 tons with the two coils having a combined weight of 54 tons, a perspective view of the dipole magnet is shown in Figure 2.5. Each coil is constituted from 15 individual mono-layer pancakes. In each pancake, the conductor is a 290 m long piece, corresponding to 15 turns. For reasons of costs, aluminium is chosen as conductor material for the coils.

The magnetic field is vertical and the magnet can be exploited in both polarities. This
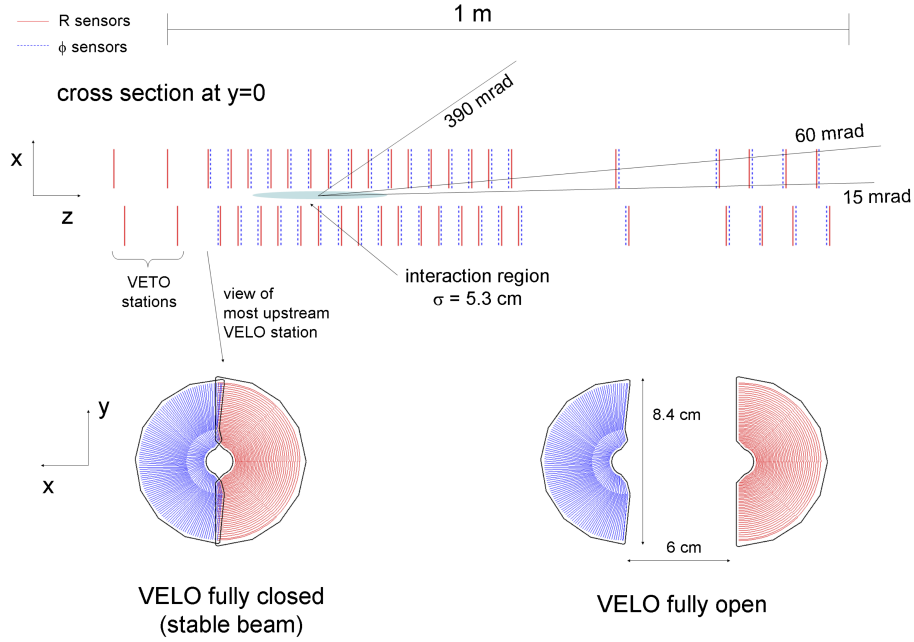
Figure 2.3: VELO detector cross section (top) and layout of the first modules when the VELO is fully closed and opened positions (bottom).
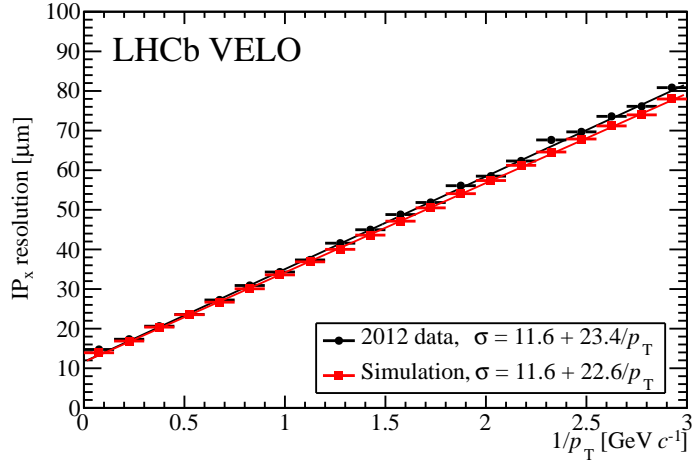
Figure 2.4: IP resolution of the x coordinate as a function of $1/p_T$ using 2012 data compared with simulation [43].

allows to control systematic uncertainties that are inherent to a detector devoted to CP asymmetry measurements. The y component of the magnetic field dependence on the z coordinate, B_y, is shown in Figure 2.5 for both polarities.
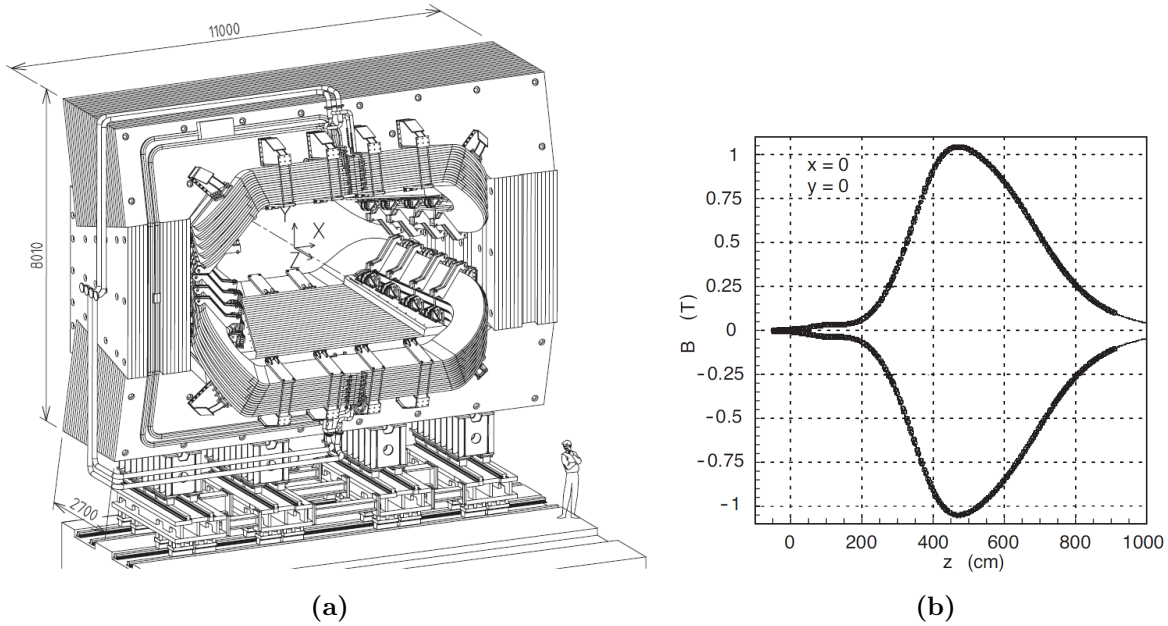
Figure 2.5: a) Perspective view of the LHCb dipole magnet. Dimensions are given in mm; b) Magnetic field along the z axis [39].

2.2.3   The tracking system

The tracking system in LHCb consists of the VELO, described in Section 2.2.1, and four planar tracking stations: the Tracker Turicensis (TT) located upstream of the dipole magnet and the other three stations T1, T2 and T3 located downstream. The T-stations include two type of detectors: the Inner Tracker (IT) and Outer Tracker (OT). VELO and TT use silicon microstrip sensors. In T1-T3, silicon microstrips are used in IT which covers the region close to the beam pipe, whereas straw-tubes are employed in the outer region of the stations.

The Tracker Turicensis

The Tracker Turicensis (TT) [45], formerly known as the Trigger Tracker, is located between the RICH1 (see Section 2.2.4) and the magnet. Besides providing additional information on the tracks recorded in the VELO that traverse the tracking stations, the TT is also used in the following two cases. First, it participates in the Level-1 trigger to assign transverse momentum information to large impact parameter tracks. Second, it is used in the offline analysis to reconstruct the trajectories of low momentum particles that are bent out of the acceptance by the magnetic field and not reaching the tracking stations T1-T3; long-lived neutral particles decaying outside of the VELO, such as K_s^0, Λ, also benefit from the TT information.

The TT consists of four detection layers, grouped in two stations TTa, TTb. Each station contains two layer and is separated by 27 cm. The first and the fourth layer have vertical detection strips, while the second and the third layer have detection strips rotated by a stereo angle of $+5°$ and $-5°$, respectively as shown in Figure 2.6. The silicon sensors in the TT are single sided p^+-on-n 500 μm thick sensors. The sensors have size of (9.64×9.44) cm in width and length and carry 512 silicon microstrips with a pitch of 183 μm.
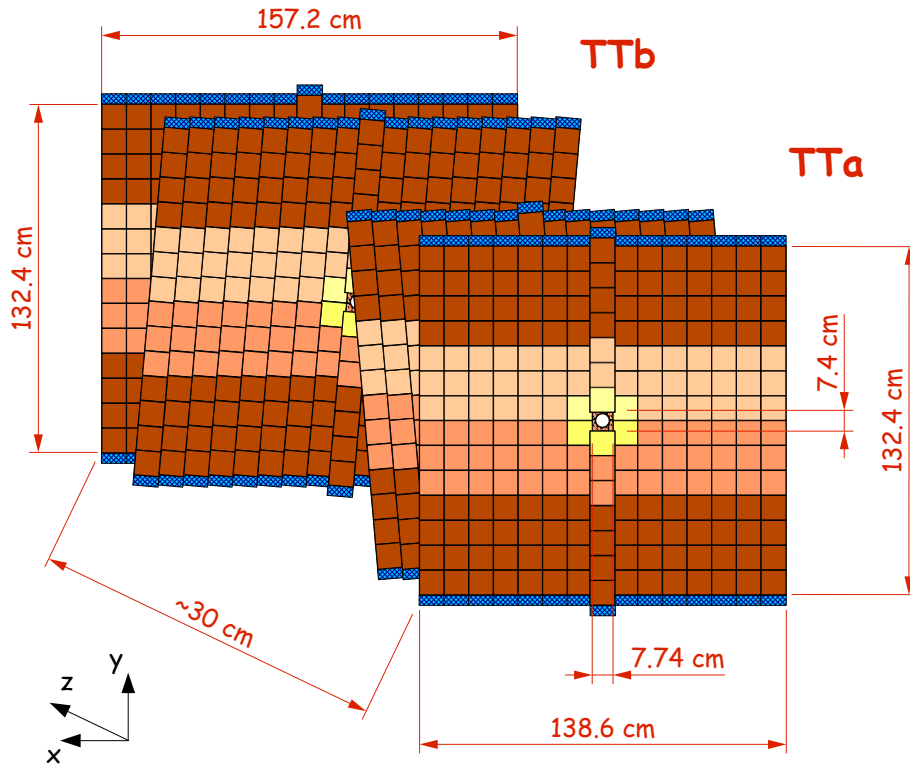
Figure 2.6: Layout of four TT layers.

The Inner Tracker

The Inner Tracker (IT) [46] covers the region close to the beam pipe where the occupancy is high. Similar to the TT, the IT use silicon microstrip sensors with a strip pitch of 198 μm. The thickness of the IT sensors are of 320 μm when they are not ganged together and 410 μm when the two sensors are assembled to form a "long" module: having a larger thickness allows to maintain the S/N ratio above 15. As illustrated in Figure 2.7, each station of the IT is composed of four boxes in a cross-shaped layout. Each box
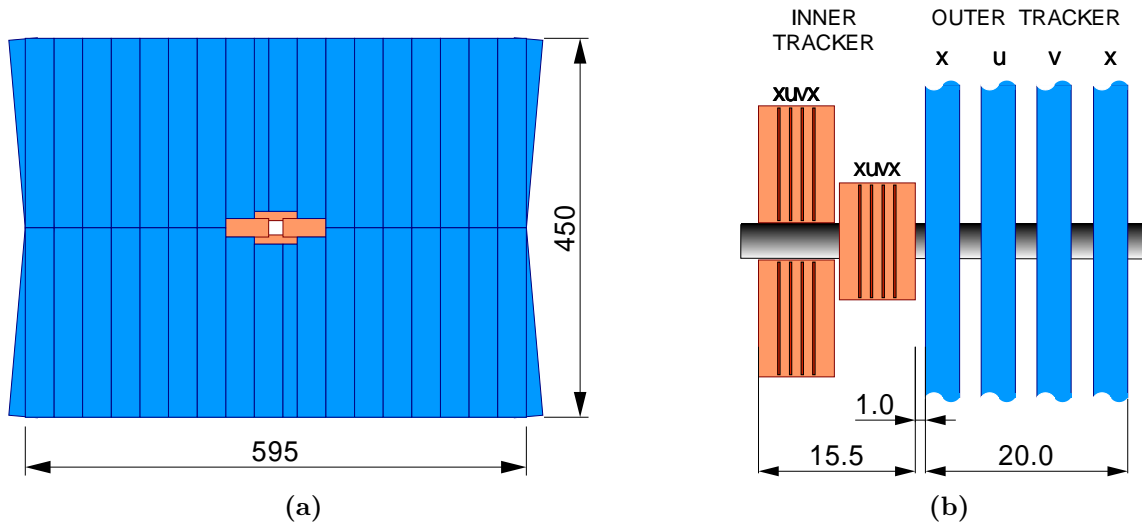
Figure 2.7: Front view (a) and top view (b) of a tracking station. The IT is shown in orange and the OT in blue. Dimensions are given in cm.
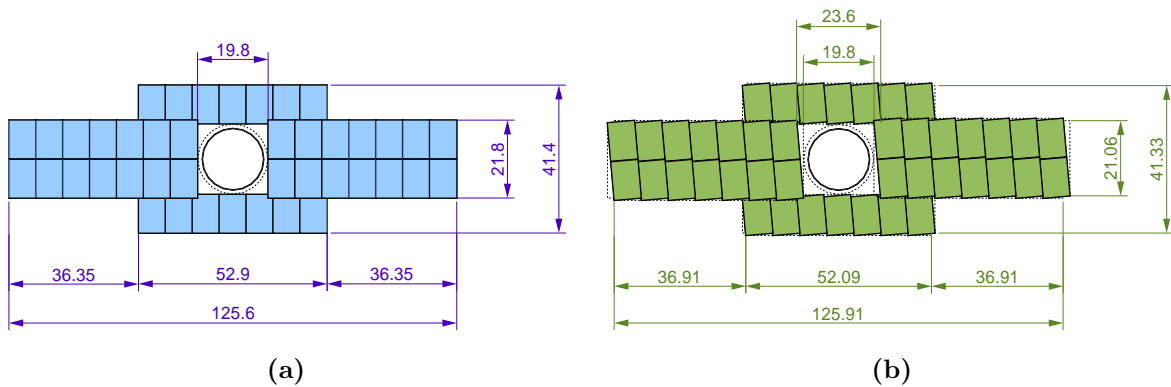
Figure 2.8: Layout of x-layer (a) and stereo layer (b) in a IT station. Dimensions are given in cm. The single sensors (at the top and bottom) are 320 µm thick, the two sensor modules are 410 µm thick.

consists of four layers of silicon sensors which arrange in x-u-v-x configuration where the x-layers have the microstrips vertical whereas the u- and v-layer are rotated by ±5°. The layout of an x-layer and of a stereo layer (u- or v-layer) in a IT station are shown in Figure 2.8.

The IT covers only 1.3% of the total acceptance around the beam pipe, but approximately 20% of all charged particles produced at the interaction point do pass through its area.
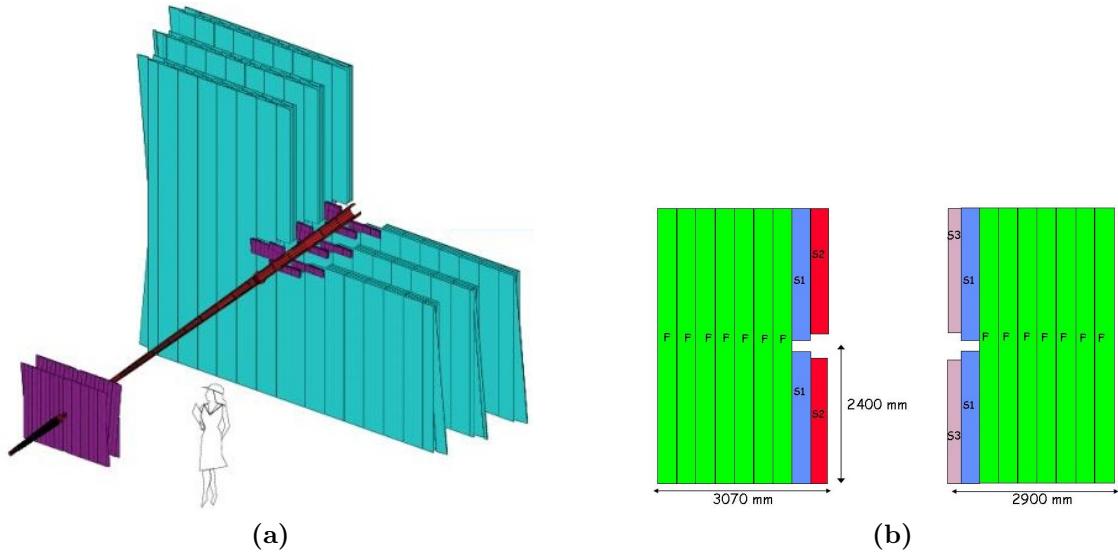
Figure 2.9: (a) Perspective view of the three OT stations (blue) surrounding the IT stations (purple); (b) The OT layout of a vertical layer.

The Outer Tracker

The Outer Tracker (OT) [47] covers the outer region of the three T-stations with an active area of $6\,\text{m} \times 5\,\text{m}$, surrounding the Inner Tracker. As for the IT, the layout of the OT consists of four layers in a x-u-v-x arrangement (see Figure 2.7): the modules in the x-layers are oriented vertically, whereas those in the u- and v- layers are tilted by $\pm 5°$ with respect to the vertical.

An OT detector is designed as an array of individual straw-tube modules. Each module contains two staggered layers (monolayers) of drift-tubes with inner diameters of 4.9 mm. A combination of Argon (70%) and CO_2 (30%) is used in order to have the drift time is shorter than 50 ns and a sufficient drift-coordinate resolution of about 190 μm.

Each detector plane is divided into two types of modules: full (F) and short (S) modules (see Figure 2.9b). The F modules have an active length of 4850 mm and contain a total of 256 straws. The S modules, located above and below the beam pipe, have about half the length of the F modules and contain 128 drift tubes. Each detector plane consists of 14 long and 8 short modules. In total, the complete OT is composed of 168 long and 96 short modules corresponding to about 55000 channels.

Track reconstruction

To find the particle trajectories from the VELO to the calorimeters, the correct hits in the VELO, the TT, the IT, and the OT are combined by the track reconstruction software.

The software aims to find all tracks in the event which leave sufficient detector hits. Depending on their trajectories in the LHCb tracking system, the tracks are classified in different types as depicted in Figure 2.10 and described in the following

- **Long tracks** traverse all the tracking system from the VELO up to the T-stations. These have the most precise momentum measurement, therefore are the most useful for physics. These long tracks are reconstructed in 95 % of the cases using the "forward tracking" algorithm when the inputs are the VELO seeds to which a cluster in the T-stations is added to define a trajectory in the T-stations. Additional clusters are searched for in the T-stations. The track candidate is then kept if it satisfies some quality criteria. The "track matching" algorithm matches the T-seeds with the VELO seeds which have not been used in the "forward tracking" algorithm. The algorithm estimates the momentum of the T-seed using the "p_T kick" method and a "good" match is chosen according to a χ^2 criterion. This "track matching" algorithm allows to reconstruct about 5 % of the long tracks.

- **Upstream tracks** traverse only the VELO and the TT stations. They are mostly low momentum tracks that are bent out of the acceptance by the magnetic field before reaching the T-stations.

- **Downstream tracks** traverse only the TT and the T-stations, and have no hits in the VELO. They allow reconstruction of decay products that decay outside the VELO acceptance, such as K_s^0, Λ.

- **VELO tracks** traverse only the VELO. They have a large polar angle and are very useful for the primary vertex reconstruction.

- **T tracks** traverse only the T-stations. They are typically produced in secondary interactions, and are used in the RICH2 reconstruction.

Once tracks have been found, their trajectories are refitted with a Kalman filter [48] which accounts for multiple scattering and corrects for dE/dx energy loss. The quality of the reconstructed tracks is estimated by the χ^2 of the fit.

2.2.4 The RICH detectors

Particle identification in the LHCb is performed by two Ring Imaging Cherenkov detectors (RICH1 and RICH2). The purpose of these two detectors is to identify charged particles by measuring their velocity that depends on the angle of the Cherenkov light cone. These
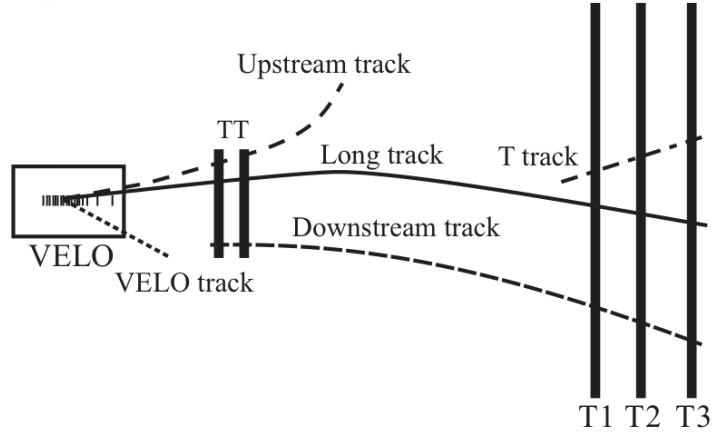
**Figure 2.10:** Track types reconstructed at LHCb.

two detectors are designed to cover the momentum spectrum of the tracks produced in the collisions.

Figure 2.11 shows the configuration of the two RICH detectors. The RICH1 detector [49] is located between the VELO and the dipole magnet. RICH1 has a wide acceptance covering the full LHCb acceptance. It covers the low momentum range, approximately 1-60 GeV/c, using aerogel and C_4F_{10} radiators. The RICH2 detector [50] is located between the last T-stations and the calorimeters. The RICH2 has a limited angular acceptance of ±15 mrad to ±120 mrad (horizontal) and ±100 mrad (vertical). It uses a CF_4 gas radiator and provides particle identification for high momentum tracks from approximately 15 up to 100 GeV/c.

In both RICH detectors, the Cherenkov light is reflected out of the spectrometer acceptance using a set of spherical and flat mirrors. Finally, the emitted Cherenkov photons are detected with Hybrid Photon Detectors (HPDs) in the wavelength range 200-600 nm. The Cherenkov rings are reconstructed using data collected by HPDs and the velocity of the charged particle is estimated.

2.2.5 The calorimeters

The calorimetry system [51] is located between the first M1 and the second M2 muon stations and consists of four sub-detectors, the Scintillating Pad Detector (SPD), the Pre-Shower (PS), the Electromagnetic CALorimeter (ECAL) and the Hadronic CALorimeter (HCAL). All calorimeter sub-detectors are based on the same detection principle: particles interact electromagnetically or strongly in the absorber, a passive material (lead for the ECAL, iron for the HCAL) used to transform the incident particle to a cascade of
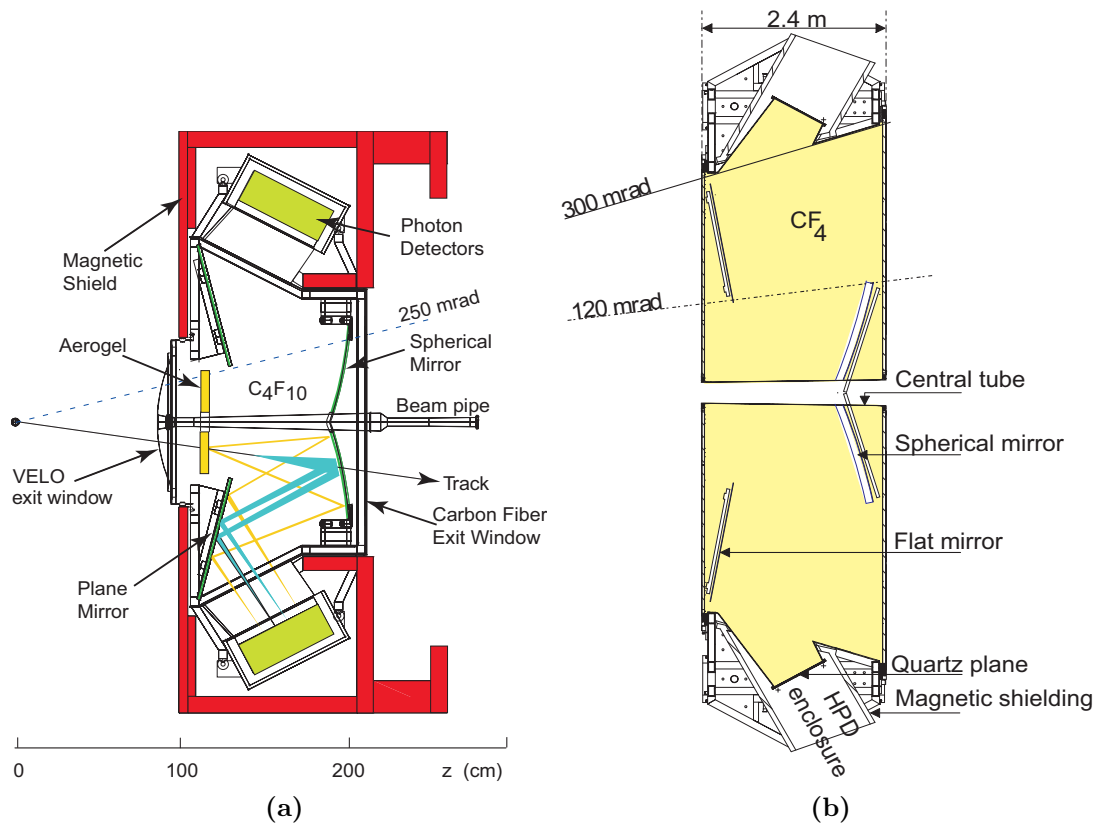
Figure 2.11: Side view schematic of the RICH1 (a) and Top view schematic of the RICH2 (b).

shower particles; the active medium for the ECAL and HCAL is scintillator whose light is brought outside the sub-detectors by WaveLength-Shifting fibers (WLS).

The LHCb calorimeters perform several functions. They select transverse energy hadron, electron and photon candidates for the first trigger level (L0), which makes a decision 4 μs after the beam crossing. They are used to identify electrons, photons and hadrons as well as to measure their energies and positions. Furthermore, the calorimeters are used to reconstruct the energy and position of the π^0 and prompt photons with a good accuracy which is essential for the study of B-meson decays.

The SPD and the PS are located behind the first muon station M1. They are both built of 15 mm thick scintillator pads. A lead layer of 12 mm (2.14 radiation length) is placed between the SPD and the PS to initiate the electromagnetic showers. The PS is used to distinguish between electrons and charged pions, while the SPD is used for the separation of electrons and photons and is used to reject high-E_T π^0 background in the trigger.

The ECAL is located right behind the SPD/PS. It is used to detect electrons and

photons and measure their transverse energy E_T in the first level trigger. It employs the "Shashlik" technology [52] and consists of 66 layers of lead absorber (2mm) and scintillator (4mm), corresponding in total to about 25 radiation lengths. With the "Shashlik" technology, the electromagnetic shower energies can be measured with a resolution of $\sigma(E)/E = 10\%/\sqrt{E} \otimes 1\%$ [39] (E in GeV and the $\otimes$ sign means that the summation is in quadrature). Together with preshower information the energy use for the separation of electrons and hadrons at the trigger level as well as the reconstruction stage.

The HCAL is located after the ECAL detector. It is used to detect hadrons and estimate their energy. It is based on an iron/scintillating tile technology and is composed of layers of 16 mm thick of iron tiles and 4 mm thick scintillator plates orientated parallel to the beam. The overall HCAL structure is built as a wall with dimensions of 8.4 m in height, 6.8 m in width and 1.65 m in length. With the detector thickness of 1.20 m is only 5.6 interaction lengths, the energy resolution is measured as: $\sigma(E)/E = (69 \pm 5)\%/\sqrt{E} \otimes (9 \pm 2)\%$ [39], E being in GeV.

2.2.6 The muon detectors

The muon system [53] is the last sub-detector in the LHCb. It consists of five muon stations (M1-M5), see Figure 2.12. The first station M1 is located upstream of the calorimeters, while the muon stations M2-M5 located after the calorimeters and are separated by 800 mm thick iron filters. The full system comprises 1380 chambers and covers a total area of 435 m^2. The total angular acceptances are 20-306 mrad horizontally and 16-258 mrad vertically. The muon system provides information about the transverse momentum p_T of the muon candidates at the first-level trigger and the muon identification is used for high level triggers and offline reconstruction.

Multi-wire proportional chambers (MWPC) are used for all regions of the muon detectors except for the central region of station M1 where the particle flux is the highest and prevent to achieve the desired detection efficiency with MWPCs. In this innermost part of the M1 station triple-GEM (Gas Electron Multiplier) technology is used. In order to achieve a time resolution of about 5 ns, the system is equipped with the MWPC with 2 mm wire spacing and a small 5 mm gas gap which are filled a gas mixture of Ar:CO$_2$:CF$_4$ in the proportions (40:55:5)%. The triple-GEM detector is made from three GEM foils sandwiched between anode and cathode planes. The GEM foils are made from 50 µm thick Kapton foils with two sides coated by 5 µm of copper. The gas mixture used is also Ar/CO$_2$/CF$_4$ in the proportion (45:15:40)% allowing to achieve a time resolution better than 3 ns. Both MWPC and triple-GEM detectors are able to collect the signal

in less than 20 ns with an efficiency larger than 95%.
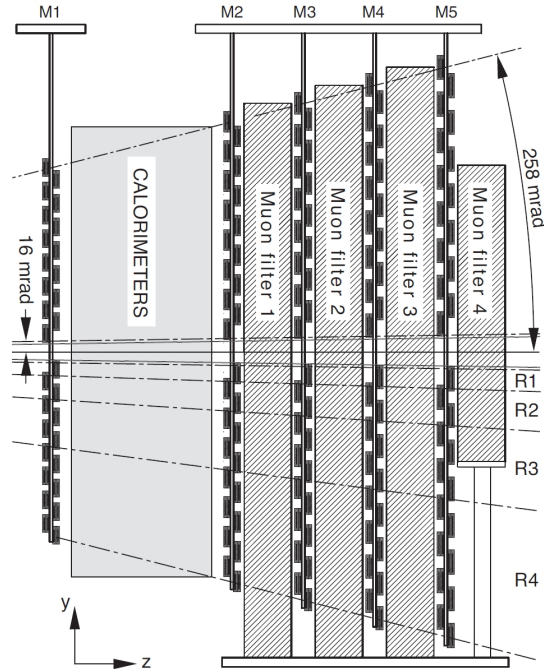
Figure 2.12: Side view of the muon system.

2.2.7   The trigger

At a luminosity of $2 \times 10^{32}\,\mathrm{cm^{-2}s^{-1}}$ the 10 MHz of bunch crossings with visible pp interaction[1] are expected to contain about 100 kHz with a $b\bar{b}$ pair: this is therefore impossible to record all the events. This rate is reduced to a few Hz for interesting events where all the decay products of the B meson go inside the LHCb acceptance.

The offline analysis uses event selections based on the masses of the B-mesons, their proper time and other cuts to improve the signal over background. Hence a trigger system [54] is developed to achieve the highest efficiency for selected events and to reduce the rate of recorded data. The trigger system in the LHCb consists of three levels called Level-0 (L0), High Level Trigger 1 (HLT1) and High Level Trigger 2 (HLT2). The L0 trigger is implemented using an electronic system, while the HLT1 and HLT2 are done by software application run on a large processor farm. All the three levels are described in the following.

---

[1]By "visible pp interaction, we mean those producing at least two charged particles with enough information in the VELO and in the tracking stations to be re-constructible.
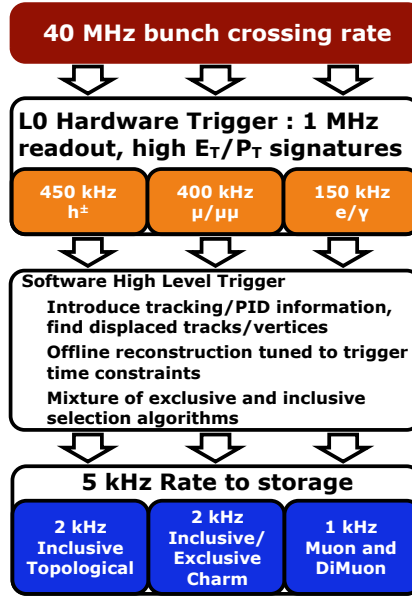
Figure 2.13: Schematic description of the LHCb trigger.

Level-0 Trigger

The first trigger level, L0, is completely implemented in hardware to be able to reduce the rate from the initial 40 MHz to 1 MHz at which the entire detector can be read out. This output rate is composed of approximately 450 kHz of hadron triggers, 400 kHz muon triggers and 150 kHz photon and electron triggers (see Figure 2.13). The L0 consists of three subsystems: the pile-up, the calorimeter trigger and the muon trigger systems. Due to their large mass, B-mesons decays often produce particles with large transverse momentum (p_T) and energy (E_T). The L0 attempts to reconstruct: the highest E_T hadron, electron and photon clusters in the calorimeters and the two highest p_T muons in the muon chambers. These informations are collected by the L0 Decision Unit (DU) in order to evaluate the final decision to select events.

The pile-up system situated upstream the VELO; it uses two r-sensitive Si planes located perpendicular to the beam axis to provide the position of the primary vertices candidates along the beam axis and a measure of the total backward charged track multiplicity. It allows to deduce the origin track and reject events with multiple vertices.

The L0 calorimeter system uses the informations from the SPD, PS, ECAL and HCAL. It computes the transverse energy (E_T) deposited in clusters of 2×2 cells. Then the

clusters with the highest E_T are identified as hadron, photon or electron candidates. The hadron candidate (`L0Hadron`) is defined from the highest E_T HCAL cluster. The photon candidate (`L0Photon`) is the highest E_T ECAL cluster with 1 or 2 PS cells hit and no hit in the corresponding SPD cells. The electron candidate (`L0Electron`) has the same requirements as the photon candidate with in addition at least one hit in the corresponding SPD cell.

The L0 muon trigger searches for muon tracks with the highest p_T (`L0Muon` and `L0DiMuon` lines). These lines select muons with $p_T > 1.3$ GeV/c or in the case of the `DiMuon` lines, muons for which $\sqrt{p_{T1} \times p_{T2}}$ (p_{T1}, p_{T2} are the highest p_T of the two muons) is higher than 1.48 GeV/c [55].

High Level Trigger 1

The HLT1 reduces the 1MHz rate at the output of L0 to about 43 kHz. At this rate the HLT2 can perform a more complete event reconstruction. The HLT1 aims to reconstruct particles in the VELO and T-stations corresponding to the L0 objects, or in the case of L0 γ and π^0 candidates, it confirms the absence of a charged particle which could be associated to these objects. Depending on the L0 trigger type, the HLT1 executes different sets of algorithms, called "alleys". These are ECAL, hadron, muon and muon+track alleys which are described in [56–59]. Only about 15% of the L0 events are selected by multiple triggers, and will consequently pass by more than one alley.

High Level Trigger 2

The output rate of the HLT1 is sufficiently low to allow the forward tracking of all VELO tracks can be performed in HLT2. The HLT2 fully reconstructs tracks in the event with $p > 3$ GeV/c and $p_T > 0.3$ GeV/c. In addition, it selects candidates based on lepton identification, lifetime information and invariant mass. The output rate of the HLT2 is about 5 kHz, which is composed of 40% inclusive hadronic triggers, 40% triggers on leptons and 20% from exclusive triggers, mainly on charmed hadrons.

The HLT2 performs various inclusive and exclusive selections. The inclusive lines have been designed to trigger on partially reconstructed b-hadron decays. These lines, called "topological" trigger lines, cover all b-hadrons based on displaced vertices of at least two charged tracks. The exclusive trigger lines are also implemented in HLT2. These lines require all decay particles to be reconstructed in HLT2 and use narrow mass windows to reduce their rate.

The decisions of the topological trigger lines are based on the properties of combinations of 2, 3, or 4 "Topo-Tracks". Topo-Tracks are a subset of HLT2 tracks selected with additional requirements on their track fit quality (χ^2/ndf) and IP and muon or electron identification. To select a n-body candidate, cuts are applied to the following variables: $\sum |p_{\mathrm{T}}|$, $p_T^{\min}$, n-body invariant mass (m), distance of closest approach (DOCA), IP significance (IPχ^2), flight distance significance (FDχ^2) and corrected mass (m_{corr}), where the corrected mass accounts for the missing momentum transverse to the direction of flight. This allows the topological trigger to select heavy favour decays even in the cases where not all the final state particles are reconstructed.

A Boosted Decision Tree (BDT) [60] has been chosen to combine all the variables mentioned above. All multivariate classifiers select n-dimensional regions of a multivariate space by learning from the training samples provided to them. If the selected regions are small relative to the resolution of the detector, the signal could oscillate between regions. This could lead to a less efficient trigger or even a not confident trigger decision. To solve this problem, all of the variables are mapped onto discrete variables. The application of the BDT with discrete variables is known as Bonsai BDT (BBDT). The BBDT ensures that the smallest interval that can be used satisfies $\Delta x_{min} > \delta x$ for all x values, where $\delta_x = \mathrm{MIN}|x_i - x_j| : x_i, x_j \in x_{discrete}$. Table 2.2 shows the discretisation scheme for each of the variables used in the BBDT and the selections for `HLT2Topon Body` lines, where $\boldsymbol{n} = 2, 3, 4$.

Variable	Cuts(2,3,4-body)	Interval used in BBDT
$\sum |p_{\mathrm{T}}|$ [GeV/c]	> 3, 4, 4	3.5, 4, 4.5, 5, 6, 7, 8, 9, 10, 15, 20
$p_T^{\min}$ [GeV/c]	> 0.5	0.6, 0.7, 0.8, 0.9, 1, 1.25, 1.5, 1.75, 2, 2.5, 3, 4, 5, 10
m [GeV/c^2]	< 7	2.5, 4.75
m_{corr} [GeV/c^2]		2, 3, 4, 5, 6, 7, 8, 9, 10, 15
DOCA [mm]	< 0.2	0.05, 0.1, 0.15
IPχ^2		20
FDχ^2/100	> 1	2, 3, 4, 5, 6, 7, 8, 9, 10, 25, 50, 100

Table 2.2: Selections for `HLT2Topon Body` lines, where $\boldsymbol{n}$ = 2,3,4 (middle column) and the discretisation scheme for each of the variables used in the BBDT (last column) [55].

The study of all topological trigger lines (`HLT2Topon Body`) on $B^0 \to \phi K^*(892)^0$ decays will be performed in Section 4.2 in order to find the best sufficient lines to use for the analysis.

2.2.8   LHCb and the analysis software

The Monte Carlo simulation is performed using the LHCb simulation framework [61] which is based on the GAUDI framework, an Object Oriented framework using C++ language. The simulations is performed in several steps which are depicted in Figure 2.14. First, proton-proton collisions are generated by GAUSS, the generated particles after that will be propagated through the detectors. Second, the simulation phase emulates the response of the real detector. All the simulated data are then digitized by BOOLE and then sent to the reconstruction step performed by BRUNEL. At this stage, the real data can also enter into the reconstruction process to build an event. In the following step, the analysis step, the physics parameters are extracted from the reconstructed events and tracks using DAVINCI. The different programs used for the generation, simulation and analysis are described in the following:
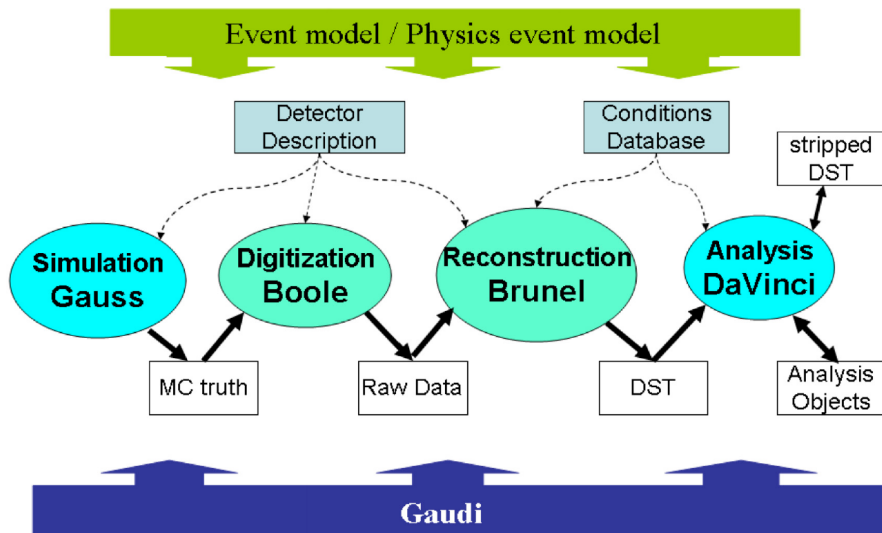
Figure 2.14: The LHCb data processing applications and data flow. Underlying all of the applications is the GAUDI framework and the event model describes the data expected. Picture is taken from [61].

- GAUSS [62] is the program which generate (Monte Carlo) simulated events. At this stage, it integrates two independent phases: the "Generator Phase" and "Simulation Phase". The Generator Phase consists of the generation of the *pp* collisions by the PYTHIA [63] package and the decay of the particles produced using EVTGEN [64]. The GEANT4 [65] package is used in the Simulation Phase to track the particles in the detector; it includes the magnetic field effects and the physics processes occurring in the experimental setup.

- BOOLE [66] is the final stage of the detector simulation. It digitalizes the data produced in the simulation phase and applies the detector response to the Monte Carlo hits previously generated by GAUSS. Other hits are added to account for the spill-over events and the LHC background. The digitization step includes the simulation of the detector responses and efficiencies and of the read-out electronics, as well as of the L0 trigger hardware. The output has the same format as the real data coming from the detector.

- BRUNEL [67] is the LHCb reconstruction application. At this phase, the simulated tracks given by BOOLE or the real data from the LHCb DAQ system are reconstructed from hits in all parts of the sub-detector. The tracks passed to the Calorimeter, Rich, and Muon detectors are used to define Particle ID reconstruction. It can process either the output of the detector digitization with BOOLE, or real data from the LHCb DAQ system.

- DAVINCI [68] is the physics analysis software of the LHCb experiment. This program is used to perform the selection of particles and the gathering of all the data needed to perform the event selection. Selection criteria are applied to the particle object such as their ID, p_T or impact parameter *etc.* These particles are then combined to form vertices, resonances, *etc.* These selections of particles can be easily performed by using a special toolkit named LOKI [69].

- Many other programs have been developed to perform the analysis in LHCb, like PANORAMIX [70] which is the graphical application of the experiment: it can display the detector and the event data objects. BENDER [71] provides end-users with a user-friendly physics analysis environment, and MOORE [72] used for the trigger studies.

All the above tasks require large amounts of computing power; therefore, LHCb is part of the Worldwide LHC Computing Grid (WLCG) project [73]. The WLCG project is a global computer network infrastructure connecting over 170 computing centers in 42 countries, with over 2 million jobs running every day. The simulation framework as well as the reconstruction and stripping of the raw data are done on this Grid. Then all the output is stored on the Grid in a large data storage estimated to be over 150 petabytes. The Grid will allow the data to be available to all the institutes that participate in the LHCb experiment, making it possible for them to perform computations that no single local cluster of computers could perform.

Chapter 3

Angular analysis

In this chapter, we will detail the angular decomposition of the $B^0 \to \phi K^{*0}$ amplitudes. The decay rate is built as a function of the helicity angles and masses; this expression of the decay rate will be used to fit the data. The acceptance of the detector plays an important role in the analysis; we have developed the method of expanding this acceptance as a four-dimensional function that depends on the three helicity angles and $K\pi$ invariant mass in term of orthogonal functions. To take the acceptance effects into account we use the method of "normalization weights" which will be described in the second section. Triple-product asymmetries, another powerful tool for displaying CP violation in weak four-body decays, are also introduced in the last section.

3.1 Angular-Mass formalism of decay $B^0 \to \phi K^*(892)^0$

### 3.1.1 Angular distribution

The angular distribution in the $B^0 \to \phi K^*(892)^0$ decay with $\phi \to K^+ K^-$ and $K^*(892)^0 \to K^+ \pi^-$ is described by the three helicity angles θ_1, θ_2, and Φ, which are depicted in Figure 3.1. The angle θ_1 (θ_2) is defined as the angle between the direction of the K^+ from the $K^{*0} \to K^+ \pi^-$ ($\phi \to K^+ K^-$) and the reverse of the B^0 direction in the K^{*0} (ϕ) rest frame. Φ is the angle between the K^{*0} and ϕ meson decay planes. This defines the helicity basis.

Let us consider a pseudo-scalar B-meson P_0 decaying to two vector particles V_1 and V_2,

$$P_0(J, M) \to V_1(s_1, \lambda_1) + V_2(s_2, \lambda_2), \tag{3.1}$$

where $(J, M) = (0, 0)$ is the spin state of the B-meson, $s_1 = s_2 = 1$ and $\lambda_{1,2}$ are the spins and the helicities of the two vector mesons respectively.
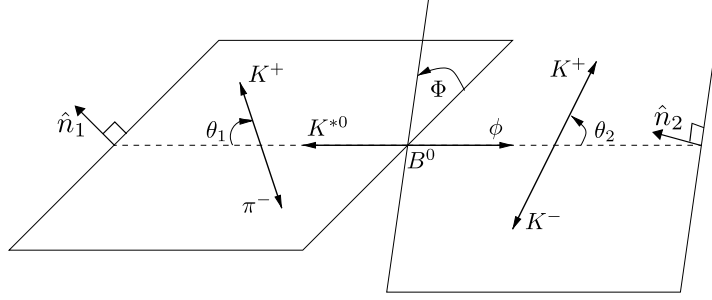
Figure 3.1: Helicity angles for the decay $B^0 \to \phi K^*(892)^0$.

As the spin of P_0 is zero, sum of the spin projection of the final vector particles on the decay axis in the P_0 rest frame has to be zero. It means V_1 and V_2 will have the same helicity ($\lambda_1 = \lambda_2$). Since $V_{1(2)}$ has spin one, $\lambda_{1(2)}$ can take three values $-1, 0, +1$. Thus there are three possible helicity states:

$$(\lambda_1, \lambda_2) = (+1, +1), \quad (0, 0) \quad \text{or} \quad (-1, -1) . \tag{3.2}$$

We can define the final helicity state as:

$$
\begin{aligned}
|f_{+1}\rangle &\equiv |JM, +1 + 1\rangle , \\
|f_0\rangle &\equiv |JM, 00\rangle , \qquad \text{(with } J = M = 0 \text{ for the three cases)} \\
|f_{-1}\rangle &\equiv |JM, -1 - 1\rangle .
\end{aligned}
\tag{3.3}
$$

The final state can be written as $|\Psi_f\rangle = \sum H_\lambda |f_\lambda\rangle$, where H_λ is the amplitude for each helicity state corresponding to $\lambda = +1, 0, -1$. Accordingly, one can write the amplitude of the decay

$$H_\lambda = \langle f_\lambda | H_{eff} | B \rangle , \tag{3.4}$$

where H_{eff} if the effective Hamiltonian.

The daughter particles decay into two pseudo-scalar. Using the angular formalism of B decays, the decay amplitude can be written as [74] [1]

$$\mathcal{A} = \sum_\lambda H_\lambda e^{i\lambda\Phi} d^{s_1}_{\lambda, \lambda_{11} - \lambda_{12}}(\theta_1) d^{s_2}_{\lambda, \lambda_{21} - \lambda_{22}}(\theta_2) , \tag{3.5}$$

---

[1] We will note by $\mathcal{A}$ the "general" decay amplitudes, in contrast with A the transversity amplitude which will be introduced in Section 3.1.3.

where d is the Wigner (small) d-matrix [75], λ_{ij} is the helicity of the daughter j from the decay of V_i, θ_1, θ_2 and Φ are three helicity angles defined in Figure 3.1.

In our case $\lambda_{ij} = 0$ and the amplitude form equation (3.5) becomes

$$\begin{aligned}
\mathcal{A} &= \sum_\lambda H_\lambda e^{i\lambda\Phi} d^1_{\lambda,0}(\theta_1) d^1_{\lambda,0}(\theta_2) \\
&= H_{+1} \frac{1}{2} \sin\theta_1 \sin\theta_2 e^{i\Phi} + H_0 \cos\theta_1 \cos\theta_2 + H_{-1} \frac{1}{2} \sin\theta_1 \sin\theta_2 e^{-i\Phi} \ .
\end{aligned} \tag{3.6}$$

Equation 3.6 would have been exact if there were a single final set of resonances and if these resonances were infinitely narrow. In our case, the $K^+\pi^-$ system can come from a resonance at a mass of 892 MeV/c^2 ($J^P = 1^-$) (P–wave), a resonance at 1430 MeV/c^2 ($J^P = 0^+$) (S–wave), or from a non-resonant background. For the K^+K^- system, it can come from the $\phi(1020)$ resonance ($J^P = 1^-$) or from the S–wave resonance $f_0(980)$ ($J^P = 0^+$) or from non-resonant background. With these possibilities, the decay amplitude (3.6) with the contribution of the $K^+\pi^-$ and K^+K^- S–wave becomes dependent on the masses and has the new form:

$$\begin{aligned}
\boldsymbol{\mathcal{M}}(\cos\theta_1, \cos\theta_2, \Phi, m_{K\pi}, m_{KK}) &= \mathcal{A}(\cos\theta_1, \cos\theta_2, \Phi, m_{K\pi}, m_{KK}) \\
&+ \mathcal{A}_S^{K\pi}(\cos\theta_1, \cos\theta_2, \Phi, m_{K\pi}, m_{KK}) \\
&+ \mathcal{A}_S^{KK}(\cos\theta_1, \cos\theta_2, \Phi, m_{K\pi}, m_{KK}) \ ,
\end{aligned} \tag{3.7}$$

where $m_{K\pi}$ (m_{KK}) is invariant mass of $K\pi$ (KK) system.

In this expression we have kept in $\mathcal{A}$ the dominant contribution of $K\pi$ and KK of P–wave:

$$\begin{aligned}
\mathcal{A}(\cos\theta_1, \cos\theta_2, \Phi, m_{K\pi}, m_{KK}) = \sum_{\lambda=0,\pm1} H_\lambda e^{i\lambda\Phi} d^1_{\lambda,0}(\theta_1) d^1_{\lambda,0}(\theta_2) \\
\times M_1^{K\pi}(m_{K\pi}) M_1^{KK}(m_{KK}) \ .
\end{aligned} \tag{3.8}$$

For the $K\pi$ and KK S–waves, the amplitudes $\mathcal{A}_S^{K\pi}$ and $\mathcal{A}_S^{KK}$ are given by [2]:

$$\begin{aligned}
\mathcal{A}_S^{K\pi}(\cos\theta_1, \cos\theta_2, \Phi, m_{K\pi}, m_{KK}) &= H_0^{K\pi} e^{i0\Phi} d^0_{0,0}(\theta_1) d^1_{0,0}(\theta_2) \\
&\times M_0^{K\pi}(m_{K\pi}) M_1^{KK}(m_{KK}) \\
&= H_0^{K\pi} \cos\theta_2 \times M_0^{K\pi}(m_{K\pi}) M_1^{KK}(m_{KK}) \ , \quad (3.9)
\end{aligned}$$

---

[2] A fourth set of amplitudes involves both $K\pi$ S–wave and KK S–wave. However, having two S–waves leads to the Wigner d-matrix element $d^0_{0,0}$ which does not exhibit any angular dependence and which we will discard in this angular analysis.

$$
\begin{aligned}
\mathcal{A}_S^{KK}(\cos\theta_1, \cos\theta_2, \Phi, m_{K\pi}, m_{KK}) =\ & H_0^{KK} e^{i0\Phi} d_{0,0}^1(\theta_1) d_{0,0}^0(\theta_2) \\
& \times M_1^{K\pi}(m_{K\pi}) M_0^{KK}(m_{KK}) \\
=\ & H_0^{KK} \cos\theta_1 \times M_1^{K\pi}(m_{K\pi}) M_0^{KK}(m_{KK})\ . \quad (3.10)
\end{aligned}
$$

We now deal with the parametrization of the masses that appear in the above equations.

3.1.2 Mass distribution

The $K\pi$ P–wave

In the case of the $K\pi$ P–wave amplitudes, the resonant masses are parametrized with a relativistic spin-1 Breit-Wigner [7], [14].

$$
M_1^{K\pi}(m_{K\pi}) = N_1 \frac{m_{K\pi}}{q} R_1^{K\pi}(m_{K\pi})\ , \tag{3.11}
$$

where N_1 is a normalisation factor and q the momentum of a daughter particle in the resonant vector meson rest frame

$$
q(m, m_a, m_b) = \frac{\sqrt{(m^2 - (m_a + m_b)^2)(m^2 - (m_a - m_b)^2)}}{2m}\ , \tag{3.12}
$$

where m_a and m_b are the daughter masses (*e.g.* $m_a = m_K$, $m_b = m_\pi$).
The Breit-Wigner amplitude is

$$
R_1^{K\pi}(m_{K\pi}) = \frac{m_0^{K^*} \Gamma_1^{K\pi}(m_{K\pi})}{\left(m_0^{K^*}\right)^2 - m_{K\pi}^2 - i m_0^{K^*} \Gamma_1^{K\pi}(m_{K\pi})}\ , \tag{3.13}
$$

with a mass-dependent width

$$
\Gamma_1^{K\pi}(m_{K\pi}) = \Gamma_0^{K^*} \frac{m_0^{K^*}}{m_{K\pi}} \frac{1 + r^2 q_0^2}{1 + r^2 q^2} \left(\frac{q}{q_0}\right)^3\ . \tag{3.14}
$$

In formula 3.14, $m_0^{K^*}$ is the K^{*0} resonance mass (895.81 MeV/c^2), $\Gamma_0^{K^*}$ is the K^{*0} resonance width (50.8 MeV/c^2). q_0 is the momentum of a daughter particle evaluated at $m_{K\pi} = m_0^{K^*}$ and r is the interaction radius [76] ($r \simeq 3.4$ GeV^{-1}).

The Equation (3.13) can be more conveniently rewritten as:

$$
R_1^{K\pi}(m_{K\pi}) = \frac{1}{\cot \delta_1^{K\pi}(m_{K\pi}) - i} = \sin \delta_1^{K\pi}(m_{K\pi}) e^{i\delta_1^{K\pi}(m_{K\pi})}\ , \tag{3.15}
$$

where

$$\cot \delta_1^{K\pi}(m_{K\pi}) = \frac{(m_0^{K^*})^2 - m_{K\pi}^2}{m_0^{K^*}\Gamma_1^{K\pi}(m_{K\pi})} \ , \tag{3.16}$$

$\delta_1^{K\pi}$ is the phase shift.

The $K\pi$ S–wave

The $K\pi$ S–wave component takes into account the spin-0 resonance $K_0^*(1430)$ contribution and a non-resonant contribution. Studies performed by the LASS experiment show that the $K\pi$ scattering is elastic up to about 1.5-1.6 GeV/c^2 and its amplitude can be parametrized as [14]

$$R_0^{K\pi}(m_{K\pi}) = \sin \delta_0 e^{i\delta_0} \ , \tag{3.17}$$

where the phase δ_0 can be splitted into a resonant part and a non-resonant part

$$\delta_0 = \Delta R + \Delta B \ .$$

The resonant part ΔR depends upon the mass via a Breit-Wigner parametrization

$$\cot \Delta R = \frac{(m_0^{K_0^*})^2 - m_{K\pi}^2}{m_0^{K_0^*}\Gamma_0^{K\pi}(m_{K\pi})} \ , \tag{3.18}$$

where $m_0^{K_0^*}$ is the resonance mass and $\Gamma_0^{K\pi}$ the mass-dependent width

$$\Gamma_0^{K\pi}(m_{K\pi}) = \Gamma_0^{K_0^*}\frac{m_0^{K_0^*}}{m_{K\pi}}\frac{q}{q_0} \ , \tag{3.19}$$

$\Gamma_0^{K_0^*}$ is the resonance width.

The non-resonant part ΔB is parametrized as

$$\cot \Delta B = \frac{1}{aq} + \frac{1}{2}bq \ , \tag{3.20}$$

where a is the scattering length and b is the effective range.

The amplitude $M_0^{K\pi}(m_{K\pi})$ is then, up to the normalization factor N_2

$$M_0^{K\pi}(m_{K\pi}) = N_2\frac{m_{K\pi}}{q}[\frac{1}{\cot \Delta B - i} + e^{2i\Delta B}\frac{1}{\cot \Delta R - i}] \ . \tag{3.21}$$

The values for parameters of the $K\pi$ S–wave and P–wave used in this analysis are summarized in Table 3.1 [14].

Due to the large width of the K^{*0} mesons it is assumed that resolution effects are negligible.

Parameter	$(K\pi)_0^*$ $J = 0$	$K^*(892)^0$ $J = 1$
$m_J\,(\,\mathrm{MeV}/c^2)$	$1435 \pm 5 \pm 5$	895.94 ± 0.25
$\Gamma_J\,(\,\mathrm{MeV}/c^2)$	$279 \pm 6 \pm 21$	50.3 ± 0.6
$r\,(\mathrm{GeV}^{-1})$	...	3.4 ± 0.7
$a\,(\mathrm{GeV}^{-1})$	$1.95 \pm 0.09 \pm 0.06$	...
$b\,(\mathrm{GeV}^{-1})$	$1.76 \pm 0.36 \pm 0.67$	...

Table 3.1: Values for the parametrization the K^+K^- invariant mass [14].

The KK P–wave

It has been shown in [77] that for a vector resonance decaying to two pseudo-scalar mesons with equal masses, the decay rate can be factorised in two terms: one describing the creation of the resonance R and other describing its decay. For the $\phi \to K^+K^-$ we use that term describing the resonance decay which corresponds to a relativistic spin-1 Breit-Wigner:

$$M_1^{KK}(m_{KK}) = N_3 \sqrt{\frac{m_{KK}}{q}} R_1^{KK}(m_{KK}) \ , \tag{3.22}$$

where N_3 is a normalization constant, and

$$R_1^{KK}(m_{KK}) = \frac{\sqrt{m_{KK}\Gamma_1^{KK}(m_{KK})}}{\left(m_0^\phi\right)^2 - m_{KK}^2 - im_0^\phi\Gamma_1^{KK}(m_{KK})} \ , \tag{3.23}$$

with the mass-dependent width given by

$$\Gamma_1^{KK}(m_{KK}) = \Gamma_0^\phi \frac{m_0^\phi}{m_{KK}} \frac{1 + r^2 q_0^2}{1 + r^2 q^2} \left(\frac{q}{q_0}\right)^3 \ , \tag{3.24}$$

with m_0^ϕ and Γ_0^ϕ are the ϕ resonance mass width respectively. q is the momentum of a daughter particle in the rest frame of the resonance, q_0 this momentum evaluated at $m = m_0^\phi$. The values for the parameters can be found in Table 3.2. The equation (3.23)

can be rewritten as:

$$R_1^{KK}(m_{KK}) = \frac{1}{m_0^\phi}\sqrt{\frac{m_{KK}}{\Gamma_1^\phi(m_{KK})}}\frac{1}{\cot\delta_1^{KK}(m_{KK}) - i}$$
$$= \frac{1}{m_0^\phi}\sqrt{\frac{m_{KK}}{\Gamma_1^\phi(m_{KK})}}\sin\delta_1^{KK}(m_{KK})e^{i\delta_1^{KK}(m_{KK})} \ , \qquad (3.25)$$

where

$$\cot\delta_1^{KK}(m_{KK}) = \frac{(m_0^\phi)^2 - m_{KK}^2}{m_0^\phi\Gamma_1^{KK}(m_{KK})} \ . \qquad (3.26)$$

To include the effect of experimental mass resolution in the KK invariant mass, the line-shape of KK resonance is convolved with a Gaussian distribution. The width of the Gaussian $(1.23 \pm 0.015\,\mathrm{MeV}/c^2)$, known as average resolution, is determined from the simulation data (see Appendix B). The acceptance regarding KK invariant mass will be studied in Section 3.2.

The KK S–wave

The KK S–wave is described by the Flatté parametrization describing the $f_0(980)$ meson close to KK threshold [78], [79]

$$M_0^{KK}(m_{KK}) = N_4 \frac{1}{m_{f_0}^2 - m_{KK}^2 - im_{f_0}(g_{\pi\pi}\rho_{\pi\pi} + g_{KK}\rho_{KK})} \ , \qquad (3.27)$$

where N_4 is a normalization factor, the constants $g_{\pi\pi}$ and g_{KK} are the $f_0(980)$ couplings to $\pi\pi$ and KK final states respectively. The ρ_{KK} and $\rho_{\pi\pi}$ factors account for the Lorentz-invariant phase space and are given as

$$\rho_{KK,(\pi\pi)} = \begin{cases} (1 - 4m_{K,(\pi)}^2/m^2)^{1/2} & \text{above } KK \text{ threshold} \\ i(4m_{K,(\pi)}^2/m^2 - 1)^{1/2} & \text{below } KK \text{ threshold.} \end{cases} \qquad (3.28)$$

In the angular-mass fit the KK S–wave line-shape is also convolved with a Gaussian distribution to include detector resolution. The resolution is the same as the KK P–wave described above.

All the values for the parameters of the Flatté parametrization are taken from [80] and shown in Table 3.2.

Parameter	$\phi(1020)$ $J = 1$	$(KK)_0$ $J = 0$
m_J (MeV/c^2)	1019.455 ± 0.020	965 ± 10
Γ_J (MeV/c^2)	4.26 ± 0.04	...
r (GeV^{-1})	3.0 ± 1.0	...
$g_{\pi\pi}$ (MeV/c^2)	...	165 ± 18
g_{KK} (MeV/c^2)	...	$(4.21 \pm 0.33)g_{\pi\pi}$

Table 3.2: Values for the parametrization the K^+K^- invariant mass. The *P–wave* parameters are taken from Reference [27] while the *S–wave* parameters from Reference [80].

3.1.3   Angular-Mass distribution

At this point we can write down the matrix element squared:

$$
\begin{aligned}
|\boldsymbol{\mathcal{M}}(\cos\theta_1, \cos\theta_2, \Phi, m_{K\pi}, m_{KK})|^2 = \ & |\mathcal{A}(\cos\theta_1, \cos\theta_2, \Phi, m_{K\pi}, m_{KK}) \\
& + \mathcal{A}_S^{K\pi}(\cos\theta_1, \cos\theta_2, \Phi, m_{K\pi}, m_{KK}) \\
& + \mathcal{A}_S^{KK}(\cos\theta_1, \cos\theta_2, \Phi, m_{K\pi}, m_{KK})|^2 \ ,
\end{aligned}
\tag{3.29}
$$

where the amplitudes $\mathcal{A}$ have been expressed in term of the helicity amplitudes in equations (3.8) to (3.10).

In a study of *CP* violation, one often want to identify the *CP* components which contribute to the measured amplitudes. This can not be done in the helicity basis by construction. One then uses the so-called "transversity basis" in which the amplitudes are linear combination of the helicity amplitudes:

$$
\begin{aligned}
&CP\text{-even longitudinal} & A_0 &= H_0 \ , \\
&CP\text{-even transverse} & A_\parallel &= \frac{H_{+1} + H_{-1}}{\sqrt{2}} \ , \\
&CP\text{-odd transverse} & A_\perp &= \frac{H_{+1} - H_{-1}}{\sqrt{2}} \ .
\end{aligned}
\tag{3.30}
$$

A_0 selects $CP = 1$ components, whereas $A_\parallel$ and $A_\perp$ allow $CP = \pm 1$ components. One has the normalization condition $A_0^2 + A_\parallel^2 + A_\perp^2 = 1$.

The decay rate for the $B^0 \rightarrow \phi K^*(892)^0$ decay as a function of the K^+K^- and $K^+\pi^-$ invariant masses and the helicity angles (depicted in Figure 3.1) is given by

$$
d^5\Gamma \propto |\boldsymbol{\mathcal{M}}(\cos\theta_1, \cos\theta_2, \Phi, m_{K\pi}, m_{KK})|^2 \times d\Omega_4(KKK\pi) \ ,
\tag{3.31}
$$

where $d\Omega_4(KKK\pi)$ is the four body phase space factor, which is further discussed in Section 3.1.4. By using the definition of the transervesity amplitude from equation (3.30)

for the three amplitudes $\mathcal{A}$, $\mathcal{A}_S^{K\pi}$ and $\mathcal{A}_S^{KK}$ ((3.8), (3.9) and (3.10)) and then substituting into the matrix element squared $|\mathcal{M}|^2$ (3.29), the decay rate (3.31) now becomes

$$d^5\Gamma = \frac{9}{8\pi} d\Omega_4(KKK\pi)$$

$$\times \left| \left(A_0 \cos\theta_1 \cos\theta_2 + \frac{A_\parallel}{\sqrt{2}} \sin\theta_1 \sin\theta_2 \cos\Phi + i\frac{A_\perp}{\sqrt{2}} \sin\theta_1 \sin\theta_2 \sin\Phi \right) \right.$$

$$\times M_1^{K\pi}(m_{K\pi}) M_1^{KK}(m_{KK})$$

$$\frac{A_S^{K\pi}}{\sqrt{3}} \cos\theta_2 \times M_0^{K\pi}(m_{K\pi}) M_1^{KK}(m_{KK})$$

$$\left. \frac{A_S^{KK}}{\sqrt{3}} \cos\theta_1 \times M_1^{K\pi}(m_{K\pi}) M_0^{KK}(m_{KK}) \right|^2 , \qquad (3.32)$$

where A_0, $A_\parallel$, $A_\perp$ are the complex amplitudes for the P–wave states. The amplitudes $A_S^{K\pi}$ A_S^{KK} are the S–wave amplitudes corresponding to the $K^+\pi^-$ or K^+K^- states. These amplitudes are defined as

$$A_0 = |A_0|e^{i\delta_0} ,$$
$$A_\parallel = |A_\parallel|e^{i\delta_\parallel} ,$$
$$A_\perp = |A_\perp|e^{i\delta_\perp} , \qquad (3.33)$$
$$A_S^{K\pi} = |A_S^{K\pi}|e^{i\delta_S^{K\pi}} ,$$
$$A_S^{KK} = |A_S^{KK}|e^{i\delta_S^{KK}} .$$

The phase δ_0 can be chosen to be zero as only the relative phase differences can be measured. The mass amplitudes are given by $M_i(m_{K\pi})$ and $M_i(m_{KK})$, where i $= 0, 1$ represents the spin of the $K^+\pi^-$ (K^+K^-) system. The mass distributions have been discussed in Section 3.1.2. To do the analysis, the mass distribution and the amplitudes in equation (3.32) must be normalised:

$$\int_{m_{K\pi}^L}^{m_{K\pi}^H} |M_i^{K\pi}(m_{K\pi})|^2 dm_{K\pi} = 1 ,$$
$$\int_{m_{KK}^L}^{m_{KK}^H} |M_i^{KK}(m_{KK})|^2 dm_{KK} = 1 , \qquad (3.34)$$

where $m_{K\pi}^{L,H}$ ($m_{KK}^{L,H}$) are the low and high mass limits for the $K^+\pi^-$ (K^+K^-) masses. We now define the fraction of P–wave F_P and the total fraction of S–waves $F_S =$

$f_{\mathrm{S}}(K\pi) + f_{\mathrm{S}}(KK)$, where $f_{\mathrm{S}}(K\pi)$ ($f_{\mathrm{S}}(KK)$) is the $K^+\pi^-$ (K^+K^-) S–wave fraction:

$$F_{\mathrm{P}} = |A_0|^2 + |A_\parallel|^2 + |A_\perp|^2 \, , \quad F_{\mathrm{S}} = |A_{\mathrm{S}}^{K\pi}|^2 + |A_{\mathrm{S}}^{KK}|^2 \, , \quad F_{\mathrm{P}} + F_{\mathrm{S}} = 1 \, . \quad (3.35)$$

For the charge conjugate process $\overline{B}^0 \to \phi \overline{K}^*(892)^0$, the differential decay rate is obtained by applying the transformation

$$\begin{aligned} A_0 &\to \overline{A}_0 \, , \\ A_\parallel &\to \overline{A}_\parallel \, , \\ A_\perp &\to -\overline{A}_\perp \, , \\ A_{\mathrm{S}}^{K\pi} &\to \overline{A}_{\mathrm{S}}^{K\pi} \, , \\ A_{\mathrm{S}}^{KK} &\to \overline{A}_{\mathrm{S}}^{KK} \, , \end{aligned} \qquad (3.36)$$

with normalised conditions

$$\overline{F}_{\mathrm{P}} = |\overline{A}_0|^2 + |\overline{A}_\parallel|^2 + |\overline{A}_\perp|^2 \, , \quad \overline{F}_{\mathrm{S}} = |\overline{A}_{\mathrm{S}}^{K\pi}|^2 + |\overline{A}_{\mathrm{S}}^{KK}|^2 \, , \quad \overline{F}_{\mathrm{P}} + \overline{F}_{\mathrm{S}} = 1 \, . \quad (3.37)$$

Now, we can rewrite equation (3.32) in a more explicit way as a sum of 15 terms

$$d^5\Gamma = \frac{9}{8\pi} \sum_{i=1}^{15} h_i \; f_i(\theta_1, \theta_2, \Phi) \mathcal{M}_i(m_{K\pi}, m_{KK}) d\Omega_4(KKK\pi) \, , \qquad (3.38)$$

where h_i are functions of the polarisation parameters, f_i are the functions of helicity angles, $\mathcal{M}_i$ are the functions of the invariant masses which modulate the amplitudes. These terms are written explicitly in Table 3.3.

With the phase convention $\delta_0 = 0$, all the measured parameters are defined in [8] and are shown in Table 3.4. The first eight parameters are the measured polarization parameters, which are defined under the assumption of no CP violation in the decay. They are often obtained by averaging between the B and $\overline{B}$ parameters. The parameters for the P–wave are the longitudinal (perpendicular) polarization fraction f_{L} ($f_\perp$), the relative phase of the perpendicular (parallel) amplitude $\delta_\perp$ ($\delta_\parallel$) to the longitudinal amplitude while for the S–wave are the $K\pi$ (KK) S–wave fraction $f_{\mathrm{S}}(K\pi)$ ($f_{\mathrm{S}}(KK)$) and the phase of the $K\pi$ (KK) S–wave amplitude $\delta_{\mathrm{S}}^{K\pi}$ (δ_{S}^{KK}). The last eight are CP asymmetry parameters, $i.e.$, the differences between the B and $\overline{B}$ meson decay parameters.

i	h_i	$f_i(\theta_1, \theta_2, \Phi)$	$\mathcal{M}_i(m_{K\pi}, m_{KK})$
1	$|A_0|^2$	$\cos\theta_1^2 \cos\theta_2^2$	$|M_1^{K\pi}(m_{K\pi})|^2 |M_1^{KK}(m_{KK})|^2$
2	$|A_\parallel|^2$	$\frac{1}{4}\sin\theta_1^2 \sin\theta_2^2(1+\cos(2\Phi))$	$|M_1^{K\pi}(m_{K\pi})|^2 |M_1^{KK}(m_{KK})|^2$
3	$|A_\perp|^2$	$\frac{1}{4}\sin\theta_1^2 \sin\theta_2^2(1-\cos(2\Phi))$	$|M_1^{K\pi}(m_{K\pi})|^2 |M_1^{KK}(m_{KK})|^2$
4	$|A_\perp||A_\parallel^*|e^{i(\delta_\perp - \delta_\parallel)}$	$-\frac{1}{2}\sin\theta_1^2 \sin\theta_2^2 \sin(2\Phi)$	$|M_1^{K\pi}(m_{K\pi})|^2 |M_1^{KK}(m_{KK})|^2$
5	$|A_\parallel||A_0^*|e^{i\delta_\parallel}$	$\sqrt{2}\cos\theta_1 \sin\theta_1 \cos\theta_2 \sin\theta_2 \cos\Phi$	$|M_1^{K\pi}(m_{K\pi})|^2 |M_1^{KK}(m_{KK})|^2$
6	$|A_\perp||A_0^*|e^{i\delta_\perp}$	$-\sqrt{2}\cos\theta_1 \sin\theta_1 \cos\theta_2 \sin\theta_2 \sin\Phi$	$|M_1^{K\pi}(m_{K\pi})|^2 |M_1^{KK}(m_{KK})|^2$
7	$|A_S^{K\pi}|^2$	$\frac{1}{3}\cos\theta_2^2$	$|M_0^{K\pi}(m_{K\pi})|^2 |M_1^{KK}(m_{KK})|^2$
8	$|A_0||A_S^{*K\pi}|e^{-i\delta_S^{K\pi}}$	$\frac{2}{\sqrt{3}}\cos\theta_1 \cos\theta_2^2$	$|M_1^{KK}(m_{KK})|^2 M_1^{K\pi}(m_{K\pi})M_0^{*K\pi}(m_{K\pi})$
9	$|A_\parallel||A_S^{*K\pi}|e^{i(\delta_\parallel - \delta_S^{K\pi})}$	$\frac{\sqrt{6}}{3}\sin\theta_1 \cos\theta_2 \sin\theta_2 \cos\Phi$	$|M_1^{KK}(m_{KK})|^2 M_1^{K\pi}(m_{K\pi})M_0^{*K\pi}(m_{K\pi})$
10	$|A_\perp||A_S^{*K\pi}|e^{i(\delta_\perp - \delta_S^{K\pi})}$	$-\frac{\sqrt{6}}{3}\sin\theta_1 \cos\theta_2 \sin\theta_2 \sin\Phi$	$|M_1^{KK}(m_{KK})|^2 M_1^{K\pi}(m_{K\pi})M_0^{*K\pi}(m_{K\pi})$
11	$|A_S^{KK}|^2$	$\frac{1}{3}\cos\theta_1^2$	$|M_0^{KK}(m_{KK})|^2 |M_1^{K\pi}(m_{K\pi})|^2$
12	$|A_0||A_S^{*KK}|e^{-i\delta_S^{KK}}$	$\frac{2}{\sqrt{3}}\cos\theta_1^2 \cos\theta_2$	$|M_1^{K\pi}(m_{K\pi})|^2 M_1^{KK}(m_{KK})M_0^{*KK}(m_{KK})$
13	$|A_\parallel||A_S^{*KK}|e^{i(\delta_\parallel - \delta_S^{KK})}$	$\frac{\sqrt{6}}{3}\sin\theta_1 \cos\theta_1 \sin\theta_2 \cos\Phi$	$|M_1^{K\pi}(m_{K\pi})|^2 M_1^{KK}(m_{KK})M_0^{*KK}(m_{KK})$
14	$|A_\perp||A_S^{*KK}|e^{i(\delta_\perp - \delta_S^{KK})}$	$-\frac{\sqrt{6}}{3}\sin\theta_1 \cos\theta_1 \sin\theta_2 \sin\Phi$	$|M_1^{K\pi}(m_{K\pi})|^2 M_1^{KK}(m_{KK})M_0^{*KK}(m_{KK})$
15	$|A_S^{K\pi}||A_S^{*KK}|e^{i(\delta_S^{K\pi} - \delta_S^{KK})}$	$\frac{2}{3}\cos\theta_1 \cos\theta_2$	$M_1^{KK}(m_{KK})M_0^{K\pi}(m_{K\pi})M_0^{*KK}(m_{KK})M_1^{*K\pi}(m_{K\pi})$

Table 3.3: The individual terms of equation (3.38). Note that the *P–wave* interference terms $i = 4$ and $i = 6$ involve the imaginary parts, while $i = 5$ involves the real part of h_i. Similarly, the interference terms between *P–wave* and *S–wave* $i = 10$ and $i = 14$ entail the imaginary parts, and the terms $i = 8, 9, 12, 13$ entail the real parts of $h_i \mathcal{M}_i(m_{K\pi}, m_{KK})$. Finally, the interference term between the two *S–wave* ($i = 15$) involves the real part of $h_i \mathcal{M}_i(m_{K\pi}, m_{KK})$.

3.1.4   Four body phase space

The partial decay rate of a particle of mass M into n-bodies in its rest frame is given in terms of the Lorentz-invariant matrix element $\mathcal{M}$ by [81]

$$d\Gamma = \frac{(2\pi)^4}{2M}|\mathcal{M}|^2 d\Omega_n(P; p_1, ..., p_n) \ , \qquad (3.39)$$

where $d\Omega_n$ is an element of n-body phase space given by

$$d\Omega_n(P; p_1, ..., p_n) = \delta^4(P - \sum_{i=1}^{n} p_i) \prod_{i=1}^{n} \frac{d^3 p_i}{(2\pi)^3 2E_i} \ , \qquad (3.40)$$

where the units $c = \hbar = 1$ are used. P is the four momentum of the mother particle, p_i is the four momentum of the daughter particles. This phase space can be generated recursively

$$d\Omega_n(P; p_1, ..., p_n) = d\Omega_j(q; p_1, ..., p_j) \times d\Omega_{n-j+1}(P; q, p_{j+1}, ..., p_n)(2\pi)^3 dq^2 \ , \qquad (3.41)$$

where $q^2 = \left(\sum_{i=1}^{j} E_i\right)^2 - \left|\sum_{i=1}^{j} \boldsymbol{p}_i\right|^2$.

For the case B^0 decays into four particles, $B^0 \to \phi(K^+ K^-)K^*(K^+\pi^-)$, the decay rate is

Parameter	Definition
f_{L}	$\frac{1}{2}(|A_0|^2/F_{\mathrm{P}} + |\overline{A}_0|^2/\overline{F}_{\mathrm{P}})$
$f_{\perp}$	$\frac{1}{2}(|A_{\perp}|^2/F_{\mathrm{P}} + |\overline{A}_{\perp}|^2/\overline{F}_{\mathrm{P}})$
$f_{\mathrm{S}}(K\pi)$	$\frac{1}{2}(|A_{\mathrm{S}}^{K\pi}|^2 + |\overline{A}_{\mathrm{S}}^{K\pi}|^2)$
$f_{\mathrm{S}}(KK)$	$\frac{1}{2}(|A_{\mathrm{S}}^{KK}|^2 + |\overline{A}_{\mathrm{S}}^{KK}|^2)$
$\delta_{\perp}$	$\frac{1}{2}(\arg A_{\perp} + \arg \overline{A}_{\perp})$
$\delta_{\parallel}$	$\frac{1}{2}(\arg A_{\parallel} + \arg \overline{A}_{\parallel})$
$\delta_{\mathrm{S}}(K\pi)$	$\frac{1}{2}(\arg A_{\mathrm{S}}^{K\pi} + \arg \overline{A}_{\mathrm{S}}^{K\pi})$
$\delta_{\mathrm{S}}(KK)$	$\frac{1}{2}(\arg A_{\mathrm{S}}^{KK} + \arg \overline{A}_{\mathrm{S}}^{KK})$
$\mathcal{A}_0^{CP}$	$(|A_0|^2/F_{\mathrm{P}} - |\overline{A}_0|^2/\overline{F}_{\mathrm{P}})/(|A_0|^2/F_{\mathrm{P}} + |\overline{A}_0|^2/\overline{F}_{\mathrm{P}})$
$\mathcal{A}_{\perp}^{CP}$	$(|A_{\perp}|^2/F_{\mathrm{P}} - |\overline{A}_{\perp}|^2/\overline{F}_{\mathrm{P}})/(|A_{\perp}|^2/F_{\mathrm{P}} + |\overline{A}_{\perp}|^2/\overline{F}_{\mathrm{P}})$
$\mathcal{A}_{\mathrm{S}}(K\pi)^{CP}$	$(|A_{\mathrm{S}}^{K\pi}|^2 - |\overline{A}_{\mathrm{S}}^{K\pi}|^2)/(|A_{\mathrm{S}}^{K\pi}|^2 + |\overline{A}_{\mathrm{S}}^{K\pi}|^2)$
$\mathcal{A}_{\mathrm{S}}(KK)^{CP}$	$(|A_{\mathrm{S}}^{KK}|^2 - |\overline{A}_{\mathrm{S}}^{KK}|^2)/(|A_{\mathrm{S}}^{KK}|^2 + |\overline{A}_{\mathrm{S}}^{KK}|^2)$
$\delta_{\perp}^{CP}$	$\frac{1}{2}(\arg A_{\perp} - \arg \overline{A}_{\perp})$
$\delta_{\parallel}^{CP}$	$\frac{1}{2}(\arg A_{\parallel} - \arg \overline{A}_{\parallel})$
$\delta_{\mathrm{S}}(K\pi)^{CP}$	$\frac{1}{2}(\arg A_{\mathrm{S}}^{K\pi} - \arg \overline{A}_{\mathrm{S}}^{K\pi})$
$\delta_{\mathrm{S}}(KK)^{CP}$	$\frac{1}{2}(\arg A_{\mathrm{S}}^{KK} - \arg \overline{A}_{\mathrm{S}}^{KK})$

Table 3.4: The measurement parameters in the angular analysis. The first eight parameters are the polarization parameters and the last eight are *CP* asymmetry parameters.

obtained according to equation (3.39):

$$dΓ_{B^0 \to KKK\pi} = \frac{(2\pi)^4}{2m_B}|\mathcal{M}_{KKK\pi}|^2 d\Omega_4(P; p_1, p_2, p_3, p_4) \, , \qquad (3.42)$$

where m_B is the mass of the B meson and p_1, p_2, p_3 and p_4 are the four momentum of the K^+, K^- from the ϕ decay and the K and π from the $K^*(892)^0$ decay. Using formula (3.41), we have the four body phase space for the decay $B^0 \to KKK\pi$:

$$d\Omega_4(P; p_1, p_2, p_3, p_4) = (2\pi)^6 d\Omega_2(m_{12}; p_1, p_2) d\Omega_2(m_{34}; p_3, p_4) d\Omega_2(m_B; m_{12}, m_{34}) dm_{12}^2 dm_{34}^2 \, . \qquad (3.43)$$

Defining $p_{ij} = p_i + p_j$, $m_{ij}^2 = p_{ij}^2$ and using the two body phase space from [81]

$$d\Omega_2(P; p_1, p_2) = \frac{1}{4(2\pi)^6} \frac{|\boldsymbol{p_1}|}{M} d\cos\theta d\varphi \, , \qquad (3.44)$$

with p_1 is the the 3-momentum of the particle 1 in the center of mass system of the mother particle with mass M. Taking θ^* as the angle between $\hat{\boldsymbol{p}}_1$ (the unit vector along $\boldsymbol{p}_1$) and the $\hat{\boldsymbol{z}}$ axis, φ^* is the angle between the $\hat{\boldsymbol{x}}\hat{\boldsymbol{y}}$ plane and the plane formed by the

particle 1 with the $\hat{\boldsymbol{z}}$ axis, formula (3.43) becomes

$$d\Omega_4(P; p_1, p_2, p_3, p_4) = \frac{1}{12(2\pi)^{12}} \frac{|\boldsymbol{p_1^*}|}{m_{12}} \frac{|\boldsymbol{p_3^*}|}{m_{34}} \frac{|\boldsymbol{p_{12}}|}{m_B} dm_{12}^2 dm_{34}^2 d\omega_1^* d\omega_3^* d\omega_{12} , \qquad (3.45)$$

where $d\omega_1^* = d\cos\theta_1^* d\varphi_1^*$, $d\omega_3^* = d\cos\theta_3^* d\varphi_3^*$ and $d\omega_{12} = d\cos\theta_{12} d\varphi_{12}$. $|\boldsymbol{p_1^*}|$, $\boldsymbol{p_3^*}|$, $|\boldsymbol{p_{12}}|$ are the momentum of the particles in their mother rest frame. Noting that $\theta_{12} = 0$ in the mother rest frame, a trivial integration of φ_3 and φ_{12} transforms the formula (3.45) into

$$d\Omega_4(P; p_1, p_2, p_3, p_4) = \frac{1}{3(2\pi)^{10} m_B} |\boldsymbol{p_1^*}||\boldsymbol{p_3^*}||\boldsymbol{p_{12}}| dm_{12} dm_{34} d\cos\theta_1^* d\varphi_1^* d\cos\theta_3^* , \quad (3.46)$$

where $|\boldsymbol{p_1^*}|$, $|\boldsymbol{p_3^*}|$ and $|\boldsymbol{p_{12}}|$ are obtained according to equation (3.12):

$$|\boldsymbol{p_1^*}| = \frac{1}{2m_{12}} \left[(m_{12}^2 - (m_K + m_\pi)^2)(m_{12}^2 - (m_K - m_\pi)^2) \right]^{1/2} ,$$

$$|\boldsymbol{p_3^*}| = \frac{1}{2m_{34}} \left[(m_{34}^2 - (m_K + m_K)^2)(m_{34}^2 - (m_K - m_K)^2) \right]^{1/2} , \qquad (3.47)$$

$$|\boldsymbol{p_{12}}| = \frac{1}{2m_B} \left[(m_B^2 - (m_{12} + m_{34})^2)(m_B^2 - (m_{12} - m_{34})^2) \right]^{1/2} .$$

Finally, we can make a re-definition of the angles, masses and momenta to match the physics of our decay channel

$$\begin{array}{lll} \theta_1^* \to \theta_1 & |\boldsymbol{p_1^*}| \to q_{K^*} & m_{12} \to m_{K\pi} \\ \theta_3^* \to \theta_2 & |\boldsymbol{p_3^*}| \to q_\phi & m_{34} \to m_{KK} . \\ \varphi_1^* \to \Phi & |\boldsymbol{p_{12}}| \to q_B \end{array} \qquad (3.48)$$

And the 4-body phase space now becomes a function of the helicity angles $(\theta_1, \theta_2, \Phi)$ and the invariant masses $(K\pi, KK)$

$$d\Omega_4(P; p_1, p_2, p_3, p_4) = \frac{2}{3(2\pi)^{10} m_B} q_{K^*} q_\phi q_B d\cos\theta_1 d\cos\theta_2 d\Phi dm_{K\pi} dm_{KK} , \qquad (3.49)$$

where q_{K^*} is the momentum of the K or π in the K^{*0} rest frame. q_ϕ is the momentum of the K^+ or K^- in the ϕ rest frame and q_B is the momentum of the K^{*0} or ϕ in the B

rest frame. The momenta are obtained according to equation (3.12):

$$q_{K^*} = \frac{1}{2m_{K\pi}} \left[(m_{K\pi}^2 - (m_K + m_\pi)^2)(m_{K\pi}^2 - (m_K - m_\pi)^2) \right]^{1/2} ,$$

$$q_\phi = \frac{1}{2m_{KK}} \left[(m_{KK}^2 - (m_K + m_K)^2)(m_{KK}^2 - (m_K - m_K)^2) \right]^{1/2} , \qquad (3.50)$$

$$q_B = \frac{1}{2m_B} \left[(m_B^2 - (m_{K\pi} + m_{KK})^2)(m_B^2 - (m_{K\pi} - m_{KK})^2) \right]^{1/2} .$$

3.1.5 Triple-product asymmetries

Another tool to study CP violation in weak decays is the investigation of the triple-product asymmetries as proposed by A. Datta and D. London [20] and by M. Gronau and J. L. Rosner [21].

These authors introduced the T-odd triple-product (TP)

$$\sin \Phi = (\hat{n}_1 \times \hat{n}_2) \cdot \hat{z} , \qquad (3.51)$$

$$\sin 2\Phi = 2(\hat{n}_1 \cdot \hat{n}_2)(\hat{n}_1 \times \hat{n}_2) \cdot \hat{z} , \qquad (3.52)$$

where $\hat{n}_{1(2)}$ is a unit vector perpendicular to the K^{*0} (ϕ) decay plane and $\hat{z}$ is unit vector in the direction of the K^{*0} in the B^0 rest frame. Φ is the angle between the K^{*0} and ϕ decay planes (see Figure 3.1).

In this section, a study of the triple-product asymmetries in the $B^0 \to \phi K^{*0}$ will be presented. All triple-product asymmetries will be assigned with the two observables.

$$V = s_{(\theta_1\theta_2)} \sin \Phi , \qquad (3.53)$$

$$U = \sin 2\Phi , \qquad (3.54)$$

where $s_{(\theta_1\theta_2)}$ is the function returning the sign of $\cos\theta_1 \cos\theta_2$. These variables correspond to the interference terms $f_4 \propto \sin^2\theta_1 \sin^2\theta_2 \sin 2\Phi$ and $f_6 \propto \sin 2\theta_1 \sin 2\theta_2 \sin \Phi$ in the decay rate (see Table 3.3).

Experimentally, a triple-product (or more precisely, a T-odd) asymmetry in the decay can be defined by an asymmetry between the number of decays involving positive and negative value of $\sin 2\Phi$ or $\sin \Phi$ [20], [21] and this asymmetry is expected to be non-zero in the presence of CP-violating or T-violating phases.

The first triple-product asymmetry concerns $U = \sin 2\Phi$

$$\mathcal{A}_T^2 \equiv \frac{\Gamma(U > 0) - \Gamma(U < 0)}{\Gamma(U > 0) + \Gamma(U < 0)}$$
$$= \frac{\left(\int_0^{\pi/2} + \int_\pi^{3\pi/2}\right) G(\Phi)d\Phi - \left(\int_{\pi/2}^\pi + \int_{3\pi/2}^{2\pi}\right) G(\Phi)d\Phi}{\int_0^{2\pi} G(\Phi)d\Phi} \ , \quad (3.55)$$

where

$$G(\Phi) = \frac{1}{2\pi}\left(|A_0|^2 + 2|A_\parallel|^2\cos^2\Phi + 2|A_\perp|^2\sin^2\Phi - 2\Im(A_\perp A_\parallel^*)\sin 2\Phi + |A_S^{K\pi}|^2 + |A_S^{K\pi}|^2\right) \quad (3.56)$$

is the distribution in Φ obtained by integrating the decay rate of Equation (3.38) over $\cos\theta_1$, $\cos\theta_2$, $m_{K\pi}$ and m_{KK}. Using the normalizing conditions (3.34) and (3.35) gives

$$\mathcal{A}_T^2 = -\frac{4}{\pi}\Im(A_\perp A_\parallel^*) \ . \quad (3.57)$$

The second triple-product asymmetry involves the interference term between $A_\perp$ and A_0 and is defined as

$$\mathcal{A}_T^1 \equiv \frac{\Gamma(V > 0) - \Gamma(V < 0)}{\Gamma(V > 0) + \Gamma(V < 0)} \ . \quad (3.58)$$

Here again, by integrating the decay rate in the range $V > 0$ and $V < 0$ one obtains

$$\mathcal{A}_T^1 = -\frac{2\sqrt{2}}{\pi}\Im(A_\perp A_0^*) \ . \quad (3.59)$$

Denoting ϕ_λ and δ_λ ($\lambda = \perp, 0, \parallel$) as the weak and strong phases, respectively (see equation (3.63) hereafter), the two triple-product asymmetries, given in (3.57) and (3.59) in terms of transversity amplitudes, can be rewritten as

$$\mathcal{A}_T^{1(2)} \propto |A_\perp A_{0(\parallel)}|\sin[(\delta_\perp - \delta_{0(\parallel)}) + (\phi_\perp - \phi_{0(\parallel)})] \ . \quad (3.60)$$

These triple-product asymmetries may be non-zero due to a strong phase difference $(\delta_\perp - \delta_{0(\parallel)} \neq 0)$ while the weak phase difference vanishes $(\phi_\perp - \phi_{0(\parallel)} = 0)$. Thus they are not genuine CP-violating or T-violating observables. Fortunately, the $B^0 \to \phi K^{*0}$ decay is a self-tagged decay whose triple-product asymmetry can be computed separately for B^0 and $\overline{B}^0$ ($\mathcal{A}_{T,B}^{1,2}$, $\mathcal{A}_{T,\overline{B}}^{1,2}$), the triple-product asymmetry therefore can be classified into two

types: "true" CP-violating triple-product asymmetry and "fake", *i.e.* not CP-violating triple-product asymmetry

$$\mathcal{A}^i_{T(\text{true})} = \frac{1}{2}(\mathcal{A}^i_{T,B} + \mathcal{A}^i_{T,\overline{B}}) \ , \tag{3.61}$$

$$\mathcal{A}^i_{T(\text{fake})} = \frac{1}{2}(\mathcal{A}^i_{T,B} - \mathcal{A}^i_{T,\overline{B}}) \ , \tag{3.62}$$

where $i = 1, 2$. By rewriting the transversity amplitudes in term of their magnitude, weak phase and strong phase

$$A_\lambda = |A_\lambda| e^{i\delta_\lambda} e^{i\phi_\lambda} \ , \qquad \overline{A}_\lambda = |A_\lambda| e^{i\delta_\lambda} e^{-i\phi_\lambda} \qquad (\lambda = \perp, 0, \|) \ , \tag{3.63}$$

and substituting Equation (3.57), (3.59) into (3.61), one gets

$$\mathcal{A}^{1(2)}_{T(\text{true})} \propto \Im(A_\perp A^*_{0(\|)} - \overline{A}_\perp \overline{A}^*_{0(\|)}) \tag{3.64}$$

$$= 2|A_\perp A_{0(\|)}| \cos(\delta_\perp - \delta_{0(\|)}) \sin(\phi_\perp - \phi_{0(\|)}) \ . \tag{3.65}$$

These "true" CP-violating quantities are non-zero even when the CP-conserving phase differences $(\delta_\perp - \delta_{0(\|)})$ vanish and, thus, are pointing to the CP-violating phase difference $(\phi_\perp - \phi_{0(\|)})$.

Similarly, the "fake" asymmetries or not CP-violating triple-product asymmetries can be expressed as follows

$$\mathcal{A}^{1(2)}_{T(\text{fake})} \propto \Im(A_\perp A^*_{0(\|)} + \overline{A}_\perp \overline{A}^*_{0(\|)}) \tag{3.66}$$

$$= 2|A_\perp A_{0(\|)}| \sin(\delta_\perp - \delta_{0(\|)}) \cos(\phi_\perp - \phi_{0(\|)}) \ . \tag{3.67}$$

They can be different from zero even when the weak phase differences $(\phi_\perp - \phi_{0(\|)})$ vanish. In the SM the value of $\mathcal{A}^i_{T(\text{true})}$ is predicted to be zero and any non-zero value obtained would indicate physics beyond the SM. Non-zero values of $\mathcal{A}^i_{T(\text{fake})}$ reflect the importance of strong phase and final-state interactions. In this analysis we can measure both "true" and "fake" triple-product asymmetries which are obtained via angular analysis of $B^0 \to \phi K^{*0}$ decay.

Two additional triple-product asymmetries (and their associated "true" and "fake") will be defined as a result of the contributions of the $K\pi$ and KK *S–wave*. These new triple-product asymmetries are produced by the interference between $A_\perp$ and $A^{K\pi}_S$ or

A_S^{KK} and can be obtained from the term h_{10} and h_{14} of Table 3.3

$$\mathcal{A}_T^3 = \frac{\Gamma(s_{\theta_2} \sin \Phi > 0) - \Gamma(s_{\theta_2} \sin \Phi < 0)}{\Gamma(s_{\theta_2} \sin \Phi > 0) + \Gamma(s_{\theta_2} \sin \Phi < 0)}$$
$$= -\sqrt{\frac{3}{2}} \int |M_1^{KK}(m_{KK})|^2 \Im\left(A_\perp A_S^{*K\pi} M_1^{K\pi}(m_{K\pi}) M_0^{*K\pi}(m_{K\pi})\right) dm_{K\pi} dm_{KK} ,$$

$$(3.68)$$

and

$$\mathcal{A}_T^4 = \frac{\Gamma(s_{\theta_1} \sin \Phi > 0) - \Gamma(s_{\theta_1} \sin \Phi < 0)}{\Gamma(s_{\theta_1} \sin \Phi > 0) + \Gamma(s_{\theta_1} \sin \Phi < 0)}$$
$$= -\sqrt{\frac{3}{2}} \int |M_1^{K\pi}(m_{K\pi})|^2 \Im\left(A_\perp A_S^{*KK} M_1^{KK}(m_{KK}) M_0^{*KK}(m_{KK})\right) dm_{K\pi} dm_{KK} ,$$

$$(3.69)$$

where $s_{\theta_i} = \text{sign}(\cos \theta_i)$ for i = 1, 2. Note that the normalization from Equations (3.34) (3.35) have been used. $\mathcal{A}_{T(\text{true})}^{3,4}$ and $\mathcal{A}_{T(\text{fake})}^{3,4}$ are defined using Equation (3.61) and (3.62).

3.2 Determination and treatment of the angular acceptance

3.2.1 Acceptance determination and corrections

Due to the detector geometry and kinematic cuts, the acceptance of the detector is not uniform as a function of the decay angles and invariant masses. To take the acceptance effects into account, the signal Probability Distribution Function (PDF) that we form from Equation (3.38) and that we will use to fit the data, needs to be modified.

Normally, in order to take into account the acceptance effect, the theoretical PDF needs to be multiplied by an acceptance function which is determined by the ratio of the generated distribution of the events after and before selections. With this method, a number of problems can arise: first, the method can cause large statistical uncertainties in some angular domains except if we use a very large data sample; second, the multi-dimensional acceptance function is very difficult to parametrize accurately (in this analysis, a four-dimensional acceptance function has been used); third, the fit process can consume a

large amount of CPU time.

To solve these problems, we are using the method of "normalization weights" which has been described and used by the BaBar [82] as well as the LHCb [83] experiment. However, these experiments used only six normalization factors of the angular functions from Monte Carlo data. For the present analysis we therefore have to extend this method to determine the 15 normalization factors corresponding to the terms of Equation (3.32).

The polarisation amplitudes and phases are determined by an unbinned log likelihood fit to the data. The fit is performed by maximising the log likelihood

$$\frac{d \ln \mathcal{L}}{d\lambda_n} = \frac{d}{d\lambda_n} \sum_e \ln \frac{s(\vec{x}_e|\vec{\lambda})}{\int s(\vec{x}|\vec{\lambda})d\vec{x}} = 0 \ , \tag{3.70}$$

where the index "e" denotes the event, $\vec{x}_e$ is the set of observables for a given event, $\vec{\lambda}$ is the set of parameters to be measured, $s(\vec{x}|\vec{\lambda})$ indicates the unnormalized signal PDF.

When we include the acceptance, $\epsilon(\vec{x})$, Equation (3.70) becomes

$$\frac{d \ln \mathcal{L}}{d\lambda_n} = \frac{d}{d\lambda_n} \sum_e \ln \frac{s(\vec{x}_e|\vec{\lambda})\epsilon(\vec{x})}{\int s(\vec{x}|\vec{\lambda})\epsilon(\vec{x})d\vec{x}} = 0 \ . \tag{3.71}$$

Using the fact that the acceptance does not depend on the physics parameters ($\vec{\lambda}$), Equation (3.71) now becomes

$$\frac{d \ln \mathcal{L}}{d\lambda_n} = \frac{d}{d\lambda_n} \sum_e \ln \frac{s(\vec{x}_e|\vec{\lambda})}{\int s(\vec{x}|\vec{\lambda})\epsilon(\vec{x})d\vec{x}} = 0 \ . \tag{3.72}$$

In our case, the observables are the three angles θ_1, θ_2, Φ and the $K\pi$ and KK invariant masses. We note these observables by $\vec{\Omega} = (\theta_1, \theta_2, \Phi, m_{K\pi}, m_{KK})$. The normalized signal PDF can be written as a sum of angular-mass ($\vec{\Omega}$) functions which are not normalized:

$$S(\vec{\Omega}) = \frac{\sum\limits_{i=1}^{15} h_i(\vec{\lambda})\mathcal{F}_i(\vec{\Omega}_e)}{\int \sum\limits_{j=1}^{15} h_j(\vec{\lambda})\mathcal{F}_j(\vec{\Omega})d\vec{\Omega}} \ , \tag{3.73}$$

where $h_i(\vec{\lambda})$ are amplitude terms containing the physics parameters,

$$\mathcal{F}_i(\vec{\Omega}) = f_i(\theta_1, \theta_2, \Phi)\mathcal{M}_i(m_{K\pi}, m_{KK}) \tag{3.74}$$

are angular-mass functions. These functions are shown in Table 3.3. The indices i and j run from 1 to 15 and corresponds to the fifteen terms of the signal PDF. With the summation convention $h_i \mathcal{F}_i \equiv \sum_i h_i \mathcal{F}_i$, Equation (3.72) becomes

$$\frac{d}{d\lambda_n} \sum_e \ln \frac{h_i(\vec{\lambda}) \mathcal{F}_i(\vec{\Omega}_e)}{h_j(\vec{\lambda}) \int \mathcal{F}_j(\vec{\Omega}) \epsilon(\vec{\Omega}) d\vec{\Omega}} = 0 . \tag{3.75}$$

In equation (3.75), the effect of the acceptance on the fit is determined by the normalization weights ξ_j:

$$\xi_j = \int \mathcal{F}_j(\vec{\Omega}) \epsilon(\vec{\Omega}) d\vec{\Omega} . \tag{3.76}$$

Whether an event gets accepted or rejected, not only depends on the set of observables $\vec{\Omega}$, but also depends on other parameters such as momentum, impact parameters, *etc.* These may be denoted as $\vec{z}$. The acceptance can then be written as

$$\epsilon(\vec{\Omega}) = \frac{\int \epsilon(\vec{\Omega}, \vec{z}) S(\vec{\Omega}, \vec{z}|\vec{\lambda}) d\vec{z}}{S(\vec{\Omega}|\vec{\lambda})} . \tag{3.77}$$

The probability to generate an event with $\vec{\Omega}$ does not depend on $\vec{z}$, and we can write:

$$S(\vec{\Omega}|\vec{\lambda}) = \int S(\vec{\Omega}, \vec{z}|\vec{\lambda}) d\vec{z} , \tag{3.78}$$

and the Equation (3.76) becomes

$$\xi_j = \int \frac{\mathcal{F}_j(\vec{\Omega})}{S(\vec{\Omega}|\vec{\lambda})} \epsilon(\vec{\Omega}, \vec{z}) S(\vec{\Omega}, \vec{z}|\vec{\lambda}) d\vec{z} d\vec{\Omega} . \tag{3.79}$$

It should be noted that $S(\vec{\Omega}, \vec{z}|\vec{\lambda}) d\vec{z} d\vec{\Omega}$ is the probability to generate an event for given $(\vec{\lambda})$ with observables between $[\vec{\Omega}, \vec{\Omega} + d\vec{\Omega}]$ and $[\vec{z}, \vec{z} + d\vec{z}]$ that means $S(\vec{\Omega}, \vec{z}|\vec{\lambda}) d\vec{z} d\vec{\Omega}$ is the weight for the generation of the events.

Thus:

$$\begin{aligned} \xi_j &\simeq \frac{1}{N_{\text{gen}}} \sum_{e \in \{\text{generated}\}} \frac{\mathcal{F}_j(\vec{\Omega}_e) \epsilon(\vec{\Omega}_e | \vec{z}_e)}{S(\vec{\Omega}_e | \vec{\lambda})} \\ &= \frac{1}{N_{\text{acc}}} \sum_{e \in \{\text{accepted}\}} \frac{\mathcal{F}_j(\vec{\Omega}_e)}{S(\vec{\Omega}_e | \vec{\lambda})} , \end{aligned} \tag{3.80}$$

where N_{gen} (N_{acc}) are the number of generated (accepted) events.

Finally, the following equation must be solved in order to determine the physics parameters

$$\frac{d\ln\mathcal{L}(\vec{\lambda})}{d\lambda_n} = \frac{d}{d\lambda_n}\sum_e \ln\frac{h_i(\vec{\lambda})\mathcal{F}_i(\vec{\Omega}_e)}{h_j(\vec{\lambda})\xi_j} = 0 \; , \tag{3.81}$$

where the normalization weights ξ_j are found in Equation (3.80).

Figure 3.2 shows detector acceptance as a function of the three helicity angles (θ_1, θ_2 and Φ) and the two invariant masses (m_{KK} and $m_{K\pi}$). These "acceptance functions" are here simply the ratio of the simulated, fully stripped and selected (see Section 4.3) events to the simulated without any cut events. We can see that the angular acceptance of the detector is not uniform as a function of the decay angle θ_1 of the $K\pi$ system. This is due to the cut applied on the transverse momentum ($p_T > 500$ MeV/c) of the pion from the $K^*(892)^0$ meson decay and the cut on the $K\pi$ invariant mass to remove peaking background contribution from $B_s^0 \to \phi\phi$ decay, see section 5.1.2 for more details. In contrast, the acceptance is relatively uniform as a function of the decay angles θ_2 and Φ, and the $K\pi$, KK invariant mass systems.

The acceptance on the KK mass system can be assumed constant therefore the detector acceptance is modelled using a four-dimensional function that depends on the three decay angles and the $K\pi$ invariant mass ($\vec{\Omega} = (\theta_1, \theta_2, \Phi, m_{K\pi})$). Since the hardware trigger decision level (L0) is based on the p_T of the decay products, the acceptance is expected to be different for events in the TOS (Trigger On Signal) and TIS (Trigger Independent of Signal) categories (see Figure 3.2). It is clear that the acceptance depends on the trigger line selection. Hence the trigger acceptance is calculated and will be corrected separately for two categories: one category for events which pass the TOS line (`L0Hadron_TOS`), and the other category for events which pass the TIS line (`L0Global_TIS`). The events that fall in the overlap between the TOS or TIS decision (17%) are treated as TOS, and the remaining TIS candidates are called "not-TOS". The TOS, TIS trigger lines definition and further studies of trigger line acceptances will be presented in Section 4.2. In the subsequent analysis the dataset is divided into these two categories and a simultaneous fit is performed.

By using the simulated data (about 151628 events after the final selection) (see Section 4.1), we obtained the normalization weights ($\xi_{j=1..15}$ described in the text) which are used in the angular-mass analysis to correct the acceptance effect in Section 5.2. The result is shown in Table 3.5.
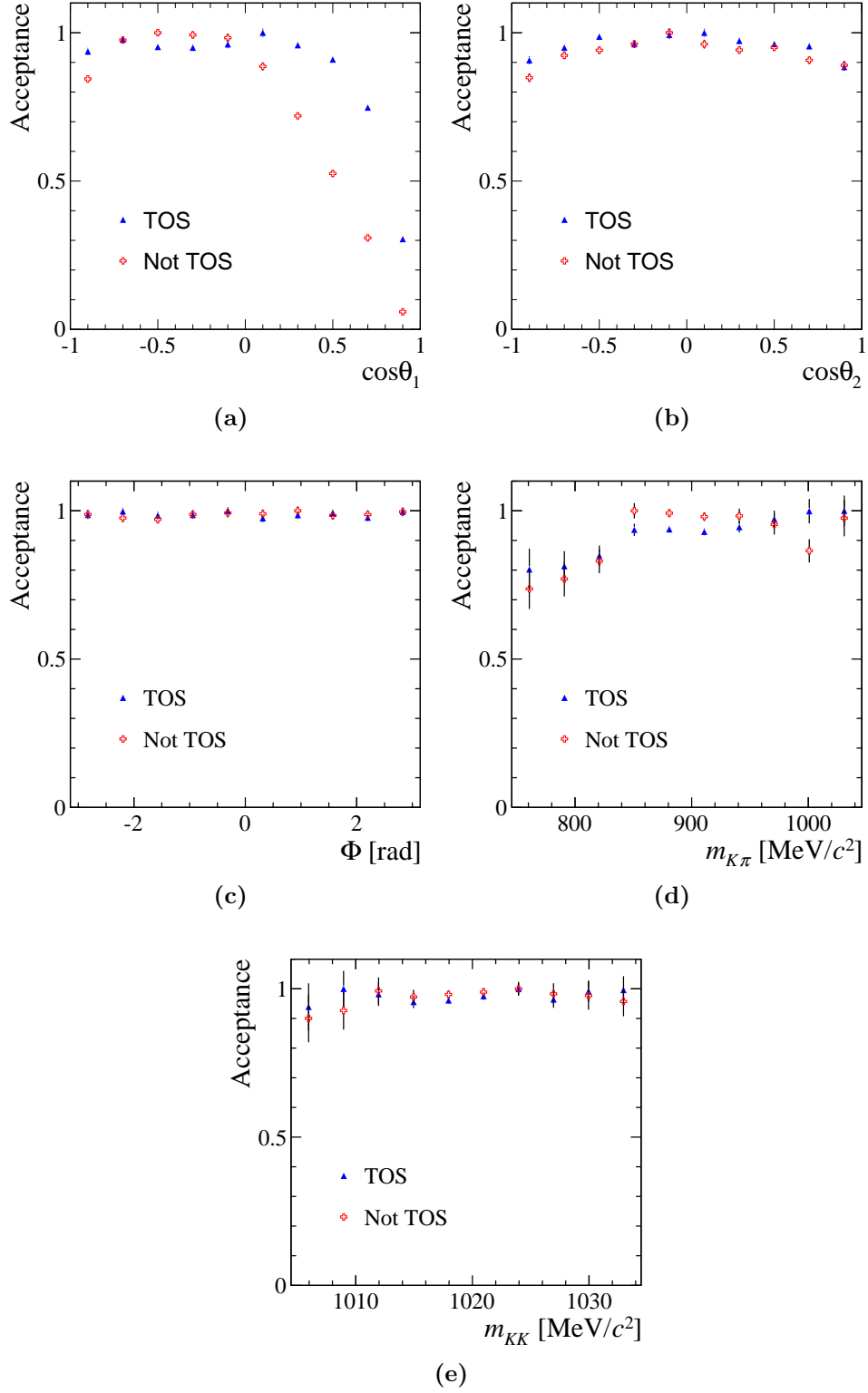
Figure 3.2: Projections of detector acceptance on the helicity angle for (a) $\cos\theta_1$, (b) $\cos\theta_2$, (c) Φ and on the invariant mass for (d) $m_{K\pi}$ and (e) m_{KK}. Simulated data with no cuts applied is used as denominator and fully stripped and selected one is used as numerator.

ξ_i	Flat Acc.	TOS weight	TIS weight
ξ_1	1	0.8860	0.8184
ξ_2	1	1.1352	1.2097
ξ_3	1	1.1507	1.2239
ξ_4	0	-0.0046	0.0131
ξ_5	0	-0.0068	-0.0099
ξ_6	0	0.0152	-0.0108
ξ_7	1	1.0395	0.9449
ξ_8	0	-0.1474	-0.4056
ξ_9	0	-0.0009	0.0013
ξ_{10}	0	0.0229	0.0035
ξ_{11}	1	0.9099	0.8237
ξ_{12}	0	-0.0137	-0.0045
ξ_{13}	0	-0.0019	0.0023
ξ_{14}	0	-0.0008	0.0005
ξ_{15}	0	-0.0085	0.0024

Table 3.5: Table showing the normalization weights ξ_j described in the text for TOS and not-TOS datasets. Values in the second column correspond to the case flat acceptance.

3.2.2   Acceptance parametrization

In this section we will introduce the parametrization of the angular acceptance with orthogonal polynomials, a method which has been used in the CDF experiment [84] and in LHCb [85], [86]. We will extent this method to include not only the three decay angles but also the $K^+\pi^-$ invariant mass.

The 3-dimensional acceptance $\epsilon(\vec{\omega})$, expressed as a function of the three helicity angles $\vec{\omega} = (\cos\theta_1, \cos\theta_2, \Phi)$, is determined using a fully simulated sample of Monte Carlo events. The acceptance can be described by an expansion in terms of Legendre polynomials $P_a(\cos\theta_1)$ and real-valued spherical harmonics $Y_{bc}(\cos\theta_2, \Phi)$[3]:

$$\epsilon(\vec{\omega}) = \sum_{abc} c^{abc} P_a(\cos\theta_1) Y_{bc}(\cos\theta_2, \Phi) \ . \tag{3.82}$$

---

[3]The product $P_a(\cos\theta_1) \times Y_{bc}(\cos\theta_2, \Phi)$ constitutes an orthonormal basis for any function of these three variables $(\cos\theta_1, \cos\theta_2, \Phi)$. The real-valued spherical harmonics are defined from the normal spherical harmonics as

$$Y_{lm} = \begin{cases} \frac{1}{\sqrt{2}}(Y_l^{-m} + (-1)^m Y_l^m) & \text{if } m > 0 \\ Y_l^0 & \text{if } m = 0 \\ \frac{i}{\sqrt{2}}(Y_l^m - (-1)^m Y_l^{-m}) & \text{if } m < 0 \end{cases}$$

The coefficient c^{abc} are determined by comparing the simulated and selected events to the "theoretical" signal distribution used in the Monte Carlo generation

$$\frac{1}{N_A} \sum_{e}^{\text{accepted}} F(\vec{\omega}_e) = \frac{1}{N_G} \sum_{e}^{\text{generated}} \epsilon(\vec{\omega}_e)F(\vec{\omega}_e)$$

$$\approx \int g(\vec{\omega})d\vec{\omega}\epsilon(\vec{\omega})F(\vec{\omega}) . \tag{3.83}$$

In this expression, N_G (N_A) are the number of generated (accepted) events, $\vec{\omega}_e$ is a set of observables, $F(\vec{\omega})$ is a set of functions which depend on $\vec{\omega}$ and $g(\vec{\omega})$ the PDF according to which the Monte Carlo sample has been generated.

In order to determine c^{abc}, we now substitute Equation (3.82) into Equation (3.83) and get

$$\frac{1}{N_A} \sum_{e}^{\text{accepted}} F(\vec{\omega}_e) = \int g(\vec{\omega})d\vec{\omega}c^{ijk}P_i(\cos\theta_1)Y_{jk}(\cos\theta_2, \Phi)F(\vec{\omega}) . \tag{3.84}$$

Using the orthogonality of the basis functions, we can now determine the coefficients c^{abc} by writing $F(\vec{\omega})$ as a product of Legendre polynomials and real-valued spherical harmonics (P_iY_{jk})[4]. Equation (3.84) becomes

$$\frac{1}{N_A} \sum_{e}^{\text{accepted}} \frac{2i+1}{2}\frac{P_iY_{jk}}{g(\vec{\omega})} = \int g(\vec{\omega})d\vec{\omega}c^{lmn}P_lY_{mn}\left(\frac{2i+1}{2}\frac{P_iY_{jk}}{g(\vec{\omega})}\right)$$

$$= c^{lmn}\frac{2i+1}{2}\int d\vec{\omega}P_lP_iY_{mn}Y_{jk} \tag{3.85}$$

$$= c^{ijk} .$$

From Equation (3.85) the coefficients c^{abc} are determined by using the simulated data; hence, the acceptance as a function of $\cos\theta_1, \cos\theta_2, \Phi$ is known.

In addition, the angular function $f_i(\vec{\omega})$, listed in Table 3.3, can be developed using the associated Legendre functions and the real-valued spherical harmonics:

$$f_i(\vec{\omega}) = \sum_{jklm} f_i^{jklm}P_j^k(\cos\theta_1)Y_{lm}(\cos\theta_2, \Phi) , \tag{3.86}$$

---

[4]P_iY_{jk} stands for $P_j(\cos\theta_1)Y_{jk}(\cos\theta_2, \Phi)$

where the P_j^k are associated Legendre functions which are related to the Legendre polynomials by

$$P_j^k(\cos\theta_1) = (-1)^k(1 - \cos^2\theta_1)^{k/2}\frac{d^k}{d(\cos\theta_1)^k}P_j(\cos\theta_1), \quad k \geqslant 0$$

and $Y_{lm}(\cos\theta_2, \Phi)$ are the real-valued spherical harmonics. The values of the coefficients f_i^{jklm} are shown in Table 3.6; thus the fifteen angular functions can also be presented in term of the associated Legendre functions and the real-valued spherical harmonics.

Consequently, we can use the acceptance $\epsilon(\vec{\omega})$ and the angular $f_i(\vec{\omega})$ in term of orthogonal function to compute the normalization for each term of the signal PDF by substituted Equations (3.86) and (3.82) into the definition $\xi_i = \int d\vec{\omega}\epsilon(\vec{\omega})f_i(\vec{\omega})$:

$$
\begin{aligned}
\xi_i = \int d\vec{\omega}\epsilon(\vec{\omega})f_i(\vec{\omega}) &= \sum_{abcjklm} c^{abc} f_i^{jklm} \int d\vec{\omega} P_a Y_{bc} P_j^k Y_{lm} \\
&= \sum_{jklma} c^{alm} f_i^{jklm} I(j, k; a, 0) ,
\end{aligned}
\tag{3.87}
$$

where $I(j, k; a, 0)$ is the integral of the overlap of Legendre polynomials [87]. Note that these normalization integrals are by construction identical to the acceptance normalization weights which is studied in Section 3.2.1 but include only the angles $(\cos\theta_1, \cos\theta_2, \Phi)$.

The technique to parametrise the angular acceptance can be trivially extended to include other dimensions such as $m_{K\pi}$. Then in this analysis the detector acceptance is modelled using a four-dimensional function that depend on the three decay angles and the $K^+\pi^-$ invariant mass, the function is given by

$$\epsilon(\vec{\Omega}, m_{K\pi}) = \sum_{abcd} c^{abcd} P_a(2\frac{m_{K\pi} - m_{K\pi}^{min}}{m_{K\pi}^{max} - m_{K\pi}^{min}} - 1)P_b(\cos\theta_1)Y_{cd}(\cos\theta_2, \Phi) . \tag{3.88}$$

The acceptance moments (c^{abcd}) are determined by summing over the fully simulated MC events to calculate the following coefficients

$$c^{abcd} = \frac{1}{N}\sum_e^N \frac{2a+1}{2}\frac{2b+1}{2}P_a(2\frac{m_{K\pi e} - m_{K\pi}^{min}}{m_{K\pi}^{max} - m_{K\pi}^{min}} - 1)P_b(\cos\theta_{1e})Y_{cd}(\cos\theta_{2e}, \Phi_e)\frac{1}{g_e} ,$$

$$\tag{3.89}$$

where g is the theoretical PDF, and $m_{K\pi}^{min(max)}$ is the minimum (maximum) value allowed for $m_{K\pi}$.

i	$f_i(\Omega) = \sum\limits_{jklm} f_i^{jklm} P_j^k(\cos\theta_1) Y_{lm}(\cos\theta_2, \Phi)$				
1	$\cos^2\theta_1 \cos^2\theta_2$	$f_1^{0000}=1$	$f_1^{0020}=\sqrt{\frac{4}{5}}$	$f_1^{2000}=2$	$f_1^{2020}=\sqrt{\frac{16}{5}}$
2	$\frac{1}{4}\sin\theta_1^2\sin\theta_2^2(1+\cos(2\Phi))$	$f_2^{2200}=\frac{1}{2}$	$f_2^{2220}=-\sqrt{\frac{1}{20}}$	$f_2^{2222}=\sqrt{\frac{3}{20}}$	
3	$\frac{1}{4}\sin\theta_1^2\sin\theta_2^2(1-\cos(2\Phi))$	$f_3^{2200}=\frac{1}{2}$	$f_3^{2220}=-\sqrt{\frac{1}{20}}$	$f_3^{2222}=-\sqrt{\frac{3}{20}}$	
4	$-\frac{1}{2}\sin\theta_1^2\sin\theta_2^2\sin(2\Phi)$	$f_4^{222-2}=-\sqrt{\frac{3}{5}}$			
5	$\sqrt{2}\cos\theta_1\sin\theta_1\cos\theta_2\sin\theta_2\cos\Phi$	$f_5^{2121}=\sqrt{\frac{6}{5}}$			
6	$-\sqrt{2}\cos\theta_1\sin\theta_1\cos\theta_2\sin\theta_2\sin\Phi$	$f_6^{212-1}=-\sqrt{\frac{6}{5}}$			
7	$\frac{1}{3}\cos\theta_2^2$	$f_7^{0000}=1$	$f_7^{0020}=\sqrt{\frac{4}{5}}$		
8	$\frac{2}{\sqrt{3}}\cos\theta_1\cos\theta_2^2$	$f_8^{1000}=2\sqrt{3}$	$f_8^{1020}=4\sqrt{\frac{3}{5}}$		
9	$\frac{\sqrt{6}}{3}\sin\theta_1\cos\theta_2\sin\theta_2\cos\Phi$	$f_9^{1121}=3\sqrt{\frac{2}{5}}$			
10	$-\frac{\sqrt{6}}{3}\sin\theta_1\cos\theta_2\sin\theta_2\sin\Phi$	$f_{10}^{112-1}=-3\sqrt{\frac{2}{5}}$			
11	$\frac{1}{3}\cos\theta_1^2$	$f_{11}^{0000}=1$		$f_{11}^{2000}=2$	
12	$\frac{2}{\sqrt{3}}\cos\theta_1^2\cos\theta_2$	$f_{12}^{0010}=2$		$f_{12}^{2010}=4$	
13	$\frac{\sqrt{6}}{3}\sin\theta_1\cos\theta_1\sin\theta_2\cos\Phi$	$f_{13}^{2111}=\sqrt{2}$			
14	$-\frac{\sqrt{6}}{3}\sin\theta_1\cos\theta_1\sin\theta_2\sin\Phi$	$f_{14}^{221-1}=-\sqrt{2}$			
15	$\frac{2}{3}\cos\theta_1\cos\theta_2$	$f_{15}^{1010}=2\sqrt{3}$			

Table 3.6: Table showing the values of coefficients f_i^{jklm} used to parametrize the angular functions $f_i(\Omega)$.

The data points on Figure 3.3 and 3.4 correspond to the Monte Carlo data which are divided by the theoretical PDF on an event-by-event basis. In order to have the best description of the acceptance, a 4th order Legendre polynomial ($b = 4$) is used to describe $\cos\theta_1$, 2nd order spherical harmonics and polynomials ($c, d, a = 2$) are used for $\cos\theta_2$, Φ and $m_{K\pi}$, respectively. The coefficients c^{abcd} of the acceptance function is calculated from Equation (3.89) using about 151628 (89709 TOS and 61919 TIS) simulated events (see Section 4.1), the results are shown in Table 3.7 and 3.8 for TOS and TIS dataset. The projections of the acceptance (red lines) on the angles and $m_{K\pi}$ are shown on Figure 3.3 and 3.4 in which the coefficients c^{abcd} are included to evaluated the acceptance for TOS and not-TOS trigger line separately.

For this the four-dimensional acceptance function parametrisation one can perform a classical fit which includes acceptance (PDF $\times \epsilon$), *i.e.* "cFit", but in this analysis we use the normalization weights method described in Section 3.2.1 to perform the angular-mass fit with acceptance correction. This acceptance PDF has been used to generate toy Monte Carlo data which includes the acceptance effect in order to study uncertainty on the acceptance correction (see Section 5.3.1). The acceptance parametrisation described in this section is used to visualize the results (see Section 5.2).
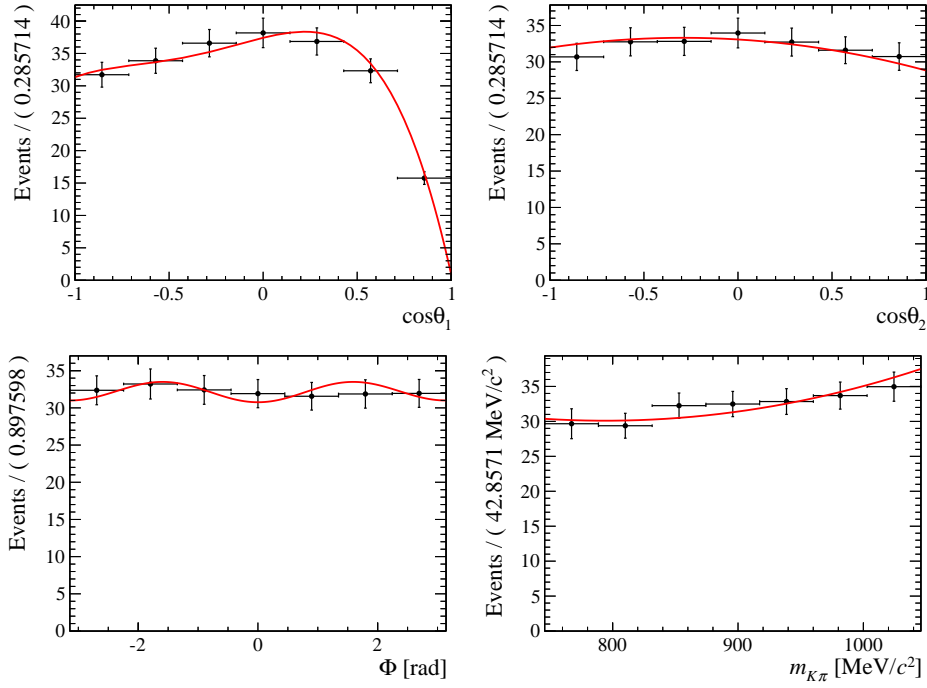
Figure 3.3: Acceptance as a function of the four variables (θ_1, θ_2, Φ, $m_{K\pi}$), corresponding to the L0 TOS line. The points correspond to the data while the red curve is a visualisation of the acceptance calculated using the method described in Section 3.2.2.
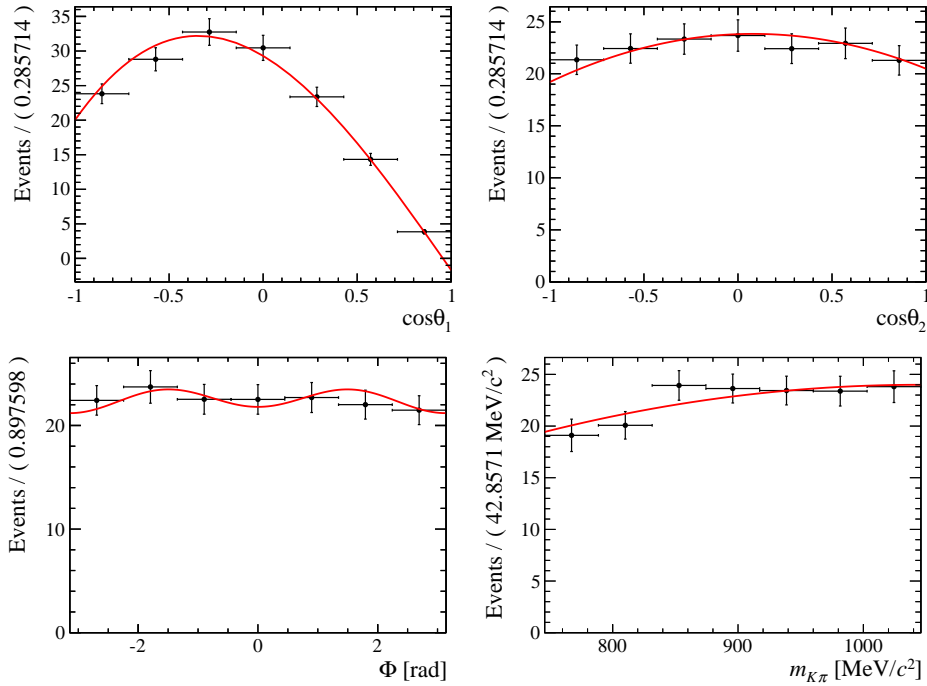
Figure 3.4: Acceptance as a function of the four variables (θ_1, θ_2, Φ, $m_{K\pi}$), corresponding to the L0 not-TOS line. The points correspond to the data while the red curve is a visualisation of the acceptance calculated using the method described in Section 3.2.2.

TOS Coeff.	Value	TOS Coeff.	Value	TOS Coeff.	Value
c^{0000}	3999.616±0.003	c^{1000}	443.196±0.007	c^{2000}	217.869±0.009
c^{0010}	-112.726±0.004	c^{1010}	-5.113±0.007	c^{2010}	48.736±0.008
c^{0011}	10.713±0.002	c^{1011}	-7.454±0.004	c^{2011}	91.882±0.006
c^{0020}	-99.797±0.003	c^{1020}	-203.844±0.007	c^{2020}	-172.825±0.008
c^{0021}	-1.780±0.002	c^{1021}	192.606±0.004	c^{2021}	-54.583±0.005
c^{0022}	-125.916±0.003	c^{1022}	-135.600±0.007	c^{2022}	-202.260±0.009
c^{0100}	-782.893±0.005	c^{1100}	-926.178±0.013	c^{2100}	176.011±0.018
c^{0110}	-192.946±0.005	c^{1110}	227.097±0.008	c^{2110}	-5.598±0.010
c^{0111}	61.341±0.004	c^{1111}	-275.472±0.009	c^{2111}	-192.384±0.012
c^{0120}	218.386±0.005	c^{1120}	444.594±0.012	c^{2120}	232.251±0.017
c^{0121}	59.629±0.003	c^{1121}	145.946±0.006	c^{2121}	181.450±0.008
c^{0122}	82.951±0.006	c^{1122}	55.417±0.016	c^{2122}	118.415±0.023
c^{0200}	-1598.811±0.007	c^{1200}	1615.420±0.018	c^{2200}	53.904±0.025
c^{0210}	148.815±0.007	c^{1210}	-261.429±0.013	c^{2210}	-233.170±0.016
c^{0211}	-79.850±0.005	c^{1211}	-21.625±0.012	c^{2211}	112.510±0.016
c^{0220}	-313.988±0.008	c^{1220}	-449.183±0.018	c^{2220}	-938.368±0.025
c^{0221}	-65.988±0.004	c^{1221}	-287.655±0.009	c^{2221}	-189.682±0.012
c^{0222}	-233.611±0.008	c^{1222}	-616.369±0.022	c^{2222}	-924.834±0.032
c^{0300}	-1110.250±0.010	c^{1300}	-1615.966±0.021	c^{2300}	-220.336±0.027
c^{0310}	349.982±0.011	c^{1310}	205.693±0.017	c^{2310}	-516.500±0.019
c^{0311}	72.145±0.005	c^{1311}	160.620±0.013	c^{2311}	-202.742±0.018
c^{0320}	31.790±0.010	c^{1320}	-87.379±0.019	c^{2320}	524.086±0.025
c^{0321}	-196.380±0.005	c^{1321}	278.072±0.011	c^{2321}	-332.359±0.014
c^{0322}	201.887±0.010	c^{1322}	791.650±0.023	c^{2322}	697.258±0.033
c^{0400}	-397.823±0.007	c^{1400}	14.673±0.017	c^{2400}	837.093±0.022
c^{0410}	3.688±0.006	c^{1410}	-74.200±0.014	c^{2410}	-88.137±0.018
c^{0411}	-6.735±0.005	c^{1411}	-228.434±0.012	c^{2411}	323.332±0.016
c^{0420}	29.680±0.008	c^{1420}	-839.892±0.018	c^{2420}	506.964±0.023
c^{0421}	77.709±0.004	c^{1421}	-297.751±0.011	c^{2421}	347.053±0.014
c^{0422}	52.967±0.008	c^{1422}	-435.310±0.019	c^{2422}	-351.677±0.026

Table 3.7: Table showing the value of the coefficients c^{abcd} calculated using the method described in Section 3.2.2 for TOS subsample.

TIS coeff.	Value	TIS coeff.	Value	TIS coeff.	Value
c^{0000}	3872.345±0.004	c^{1000}	392.657±0.010	c^{2000}	-132.026±0.014
c^{0010}	63.387±0.003	c^{1010}	-203.337±0.007	c^{2010}	339.431±0.009
c^{0011}	-38.337±0.001	c^{1011}	175.543±0.003	c^{2011}	-46.381±0.004
c^{0020}	-203.426±0.003	c^{1020}	146.398±0.008	c^{2020}	-70.276±0.012
c^{0021}	-9.119±0.002	c^{1021}	51.690±0.004	c^{2021}	-15.231±0.005
c^{0022}	-131.979±0.006	c^{1022}	398.253±0.016	c^{2022}	-578.451±0.024
c^{0100}	-2239.851±0.008	c^{1100}	-226.513±0.022	c^{2100}	-22.545±0.032
c^{0110}	-142.097±0.005	c^{1110}	273.852±0.012	c^{2110}	-692.251±0.018
c^{0111}	-7.033±0.002	c^{1111}	14.483±0.005	c^{2111}	59.461±0.006
c^{0120}	150.421±0.006	c^{1120}	-483.204±0.018	c^{2120}	265.147±0.026
c^{0121}	49.769±0.002	c^{1121}	-37.322±0.005	c^{2121}	77.475±0.006
c^{0122}	279.227±0.013	c^{1122}	-1036.525±0.038	c^{2122}	1367.863±0.056
c^{0200}	-2323.811±0.008	c^{1200}	-258.342±0.021	c^{2200}	66.931±0.031
c^{0210}	56.218±0.005	c^{1210}	4.403±0.014	c^{2210}	254.076±0.019
c^{0211}	41.539±0.003	c^{1211}	-244.995±0.007	c^{2211}	195.641±0.009
c^{0220}	44.499±0.007	c^{1220}	372.375±0.018	c^{2220}	-189.614±0.026
c^{0221}	-9.969±0.003	c^{1221}	-197.076±0.008	c^{2221}	203.286±0.010
c^{0222}	-208.959±0.013	c^{1222}	803.387±0.035	c^{2222}	-1220.012±0.052
c^{0300}	368.614±0.004	c^{1300}	109.631±0.010	c^{2300}	629.899±0.014
c^{0310}	88.820±0.005	c^{1310}	33.471±0.011	c^{2310}	388.647±0.015
c^{0311}	21.355±0.004	c^{1311}	44.575±0.008	c^{2311}	-125.090±0.010
c^{0320}	18.052±0.004	c^{1320}	410.792±0.010	c^{2320}	168.612±0.013
c^{0321}	-77.096±0.003	c^{1321}	296.523±0.008	c^{2321}	-268.596±0.010
c^{0322}	136.121±0.005	c^{1322}	79.465±0.011	c^{2322}	489.793±0.015
c^{0400}	30.262±0.009	c^{1400}	28.645±0.023	c^{2400}	-424.890±0.034
c^{0410}	-135.057±0.007	c^{1410}	121.636±0.017	c^{2410}	-594.993±0.023
c^{0411}	-61.980±0.004	c^{1411}	21.325±0.009	c^{2411}	-149.296±0.012
c^{0420}	147.608±0.008	c^{1420}	-740.591±0.020	c^{2420}	456.374±0.029
c^{0421}	-22.900±0.004	c^{1421}	268.392±0.010	c^{2421}	-180.587±0.013
c^{0422}	168.649±0.014	c^{1422}	-662.846±0.038	c^{2422}	1168.509±0.055

Table 3.8: Table showing the value of the coefficients c^{abcd} calculated using the method described in Section 3.2.2 for not-TOS subsample.

Chapter 4

Reconstruction and selection

The events are selected in three stages. First, the raw data is required to pass the trigger selections including the Level-0 hardware trigger (L0), the Hight Level Triggers HLT1 and HLT2. For the trigger lines used in this analysis are introduced further in Section 2.2.7. Second, a loose selection, called the stripping and offline selection, is applied to retain the majority of signal events and reduce a large fraction of the background. After these steps the signal from the $B^0 \to \phi K^*(892)^0$ decay is formed and clearly appears. Finally, a multivariate method is used to further reduce the background.

4.1   The data samples

The analysis of $B^0 \to \phi K^*(892)^0$ presented in this thesis uses data of pp collisions at a centre-of-mass energy of $\sqrt{s} = 8\,\text{TeV}$ corresponding to an integrated luminosity of $2.08\,\text{fb}^{-1}$. The data was recorded at the LHCb experiment during the year 2012.

Simulated data are used in this analysis to understand and correct the detector acceptance, to validate the fit model and to model invariant mass distributions. The $B^0 \to \phi K^*(892)^0$ events are generated for P–wave only with helicity amplitudes given in Table 4.1. These values are based on the previous results of the Belle and BaBar collaborations. The transversity amplitudes are obtained by using the transformation given in Equation (3.30). The simulated data was generated at a centre-of-mass energy of $\sqrt{s} = 8\,\text{TeV}$ and is known as Monte Carlo 2012. The generation procedure is described in Section 2.2.8. Ten millions of generated events are required to pass the same selection criteria as the real data such as offline (see Section 4.3) and BDT selection (see Section 4.4). After all the selections, 151628 simulated events remain.

Helicity basis		Transversity basis	
Amplitude	Phase	Amplitude	Phase
$H_+ = 0.69$	$\delta_+ = 1.39$	$f_L = 0.521$	$\delta_\perp = 1.426$
$H_0 = 0.72$	$\delta_0 = 0.0$	$f_\perp = 0.251$	$\delta_\parallel = 1.352$
$H_- = 0.03$	$\delta_- = 0.74$		

Table 4.1: Polarisation amplitudes and phases in helicity and transversity basis which were used in the generation of the simulated data.

4.2   Triggers

The tracks from each $B^0 \to \phi K^*(892)^0$ decay are required to pass the subsets of the trigger algorithm that accept the majority of the signal events. At the L0 trigger stage, the signal candidate is required to pass L0Hadron algorithm with transverse energy $E_T > 3.5$ GeV for the highest E_T HCAL cluster. If there is a highest E_T ECAL cluster located in front of the E_T of the HCAL and ECAL clusters, the E_T of the hadron candidate is the sum of the E_T of the HCAL and ECAL clusters. At the HLT1 stage, the signal candidate is required to pass the `HLT1TrackAllL0` algorithm whose requirements are summarized in Table 4.2.

Variable	`HLT1TrackAllL0` line
Track IP (mm)	> 0.1
VELO Hits	> 9
VELO Missing Hits	< 3
Track p (GeV/c)	> 10
Track p_T (GeV/c)	> 1.6
Track fit χ^2/ndf	< 3
Track minimum IP χ^2	> 16

Table 4.2: Requirements for `HLT1TrackAllL0` trigger line.

At the final stage (HLT2), the signal candidate must activate the 3-body Topological trigger (see HLT2 in Section 2.2.7), `HLT2Topo3BodyBBDT`, or the inclusive ϕ line (`HLT2IncPhi`). The `HLT2IncPhi` algorithm selects detached (*i.e.* non originating from the primary vertex) ϕ mesons built from pairs of oppositely charged kaons, where each of kaon track is required to satisfy track quality χ^2/ndf < 5, minimum IP $\chi^2 > 6$, transverse momentum $p_T > 800$ MeV/c, DLL$_{K\pi} > 0$ and the KK system is required to satisfy $p_T > 1800$ MeV/c, vertex quality χ^2/ndf < 20, the distance of closest approach < 0.2 mm and $|m - m_\phi| < 20$ MeV/c^2 [88].

Trigger categories

The event candidates passing the trigger can be classified in three categories, which are defined as follows:

- Trigger On Signal (TOS): contains candidates which are sufficient to trigger the experiment.

- Trigger Independent of Signal (TIS): the activated trigger lines are not associated to the signal.

- Trigger On Both (TOB): contains candidates in which both signal and non-signal particles are necessary to trigger; they are however neither TOS nor TIS.

In this analysis, all events are required to pass `L0Hadron_TOS` line or `L0Global_TIS` line, where "Global" stands for Level-0 (L0) trigger. These events are also required to be in TOS categories for the High Level Trigger HLT1 and HLT2.

Angular acceptance of HLT2 trigger lines

In the following, the effect of HLT2 trigger lines on the angular acceptance will be studied in order to decide which lines are sufficient to use for the analysis.

Figure 4.1 shows the distribution of the angular acceptance of the L0, HLT1 and HLT2 trigger lines. The acceptances are obtained from simulated events and are defined as the ratio of the number of events passing the main selection (Table 4.4) and each trigger line (Figure 4.1) to the generated number. In these plots an event can appear in several histograms, since an event can simultaneously satisfy more than one trigger line. From Figure 4.1 one can see a clear dependency of the angular acceptance on the trigger line. Figure 4.2 shows projections of the angular acceptance of the HLT1 and HLT2 lines, divided by the acceptance of the `L0Hadron_TOS` or `L0Global_TIS` line, depending on which line the event was triggered. This allows to show the acceptance of the line corrected by L0 and stripping selection. Analogously, Figure 4.3 shows the distributions of the angular acceptance of the HLT1 and HLT2 lines, divided by the acceptance of the `L0Hadron_TOS` or `L0Global_TIS` line, depending on which line the event was triggered. But in this case an event is selected with the following priority order: `HLT2IncPhi_TOS` + `Hlt2Topo3BodyBBDT_TOS`, `Hlt2Topo2BodyBBDT_TOS` then `Hlt2Topo4BodyBBDT_TOS`. In other word, an event is assigned to the `Hlt2Topo2BodyBBDT_TOS` histogram if it is not selected into the `HLT2IncPhi_TOS` + `Hlt2Topo3BodyBBDT_TOS` line and finally an event which is not assigned to those two histograms, goes into `Hlt2Topo4BodyBBDT_TOS`. As one

can see on Figure 4.3, the trigger lines `Hlt2Topo3BodyBBDT_TOS` and `Hlt2IncPhi_TOS`
have similar acceptance shapes and the trigger lines `HLT2Topo2BodyBBDT_TOS` and
`HLT2Topo4BodyBBDT_TOS` have very large angular acceptance effects. In conclusion, the
trigger lines `Hlt2Topo3BodyBBDT_TOS` and `Hlt2IncPhi_TOS` are selected for this analysis.
Finally, all the trigger lines used in the analysis are summarized in Table 4.3.

Trigger Level	Trigger Line
Level-0	`L0Hadron_TOS` or `L0Global_TIS`
HLT1	`Hlt1TrackAllL0_TOS`
HLT2	`Hlt2Topo3BodyBBDT_TOS` or `Hlt2IncPhi_TOS`

Table 4.3: Trigger lines used to select $B^0 \to \phi K^*(892)^0$ candidates.
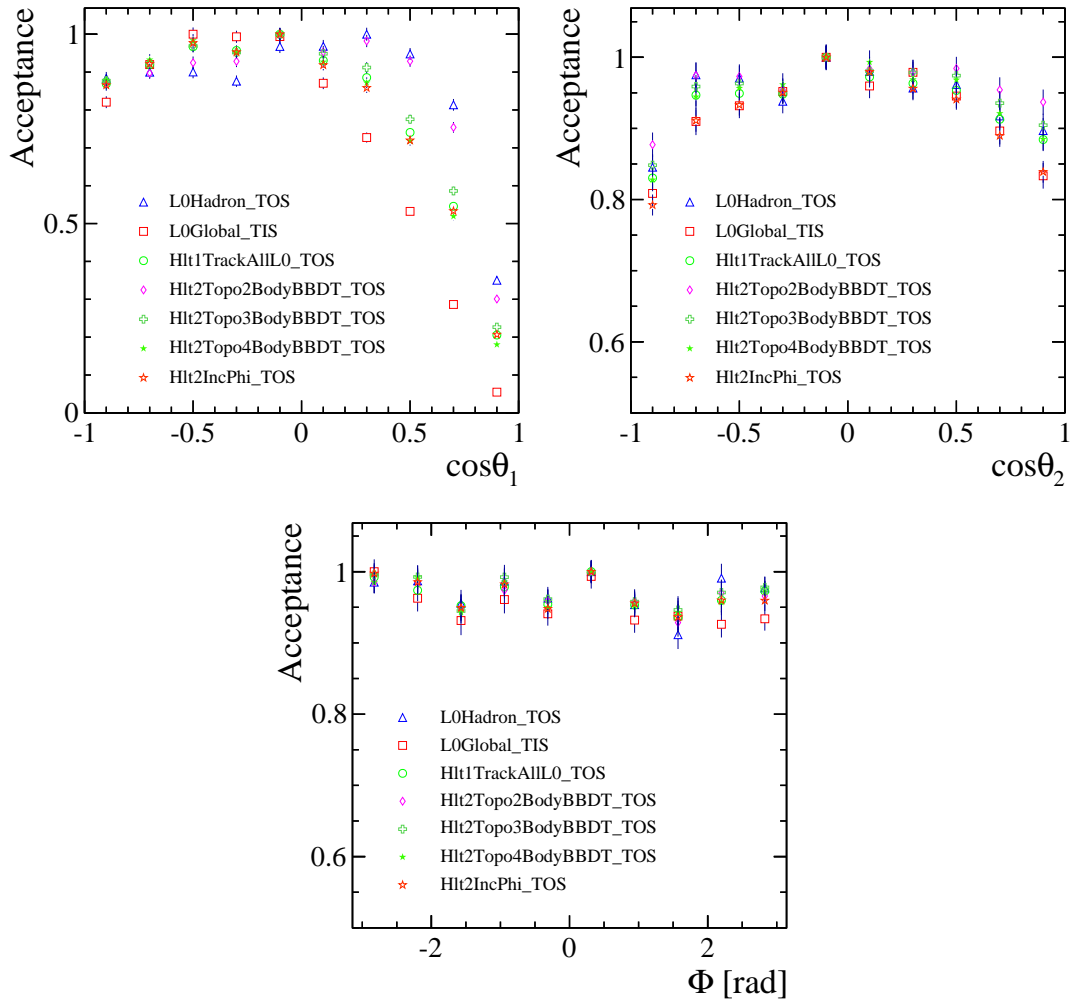
Figure 4.1: Distributions of the angular acceptance on $\cos\theta_1$, $\cos\theta_2$ and Φ. Simulated data with no cuts applied, fully stripped and selected are used in the calculation.
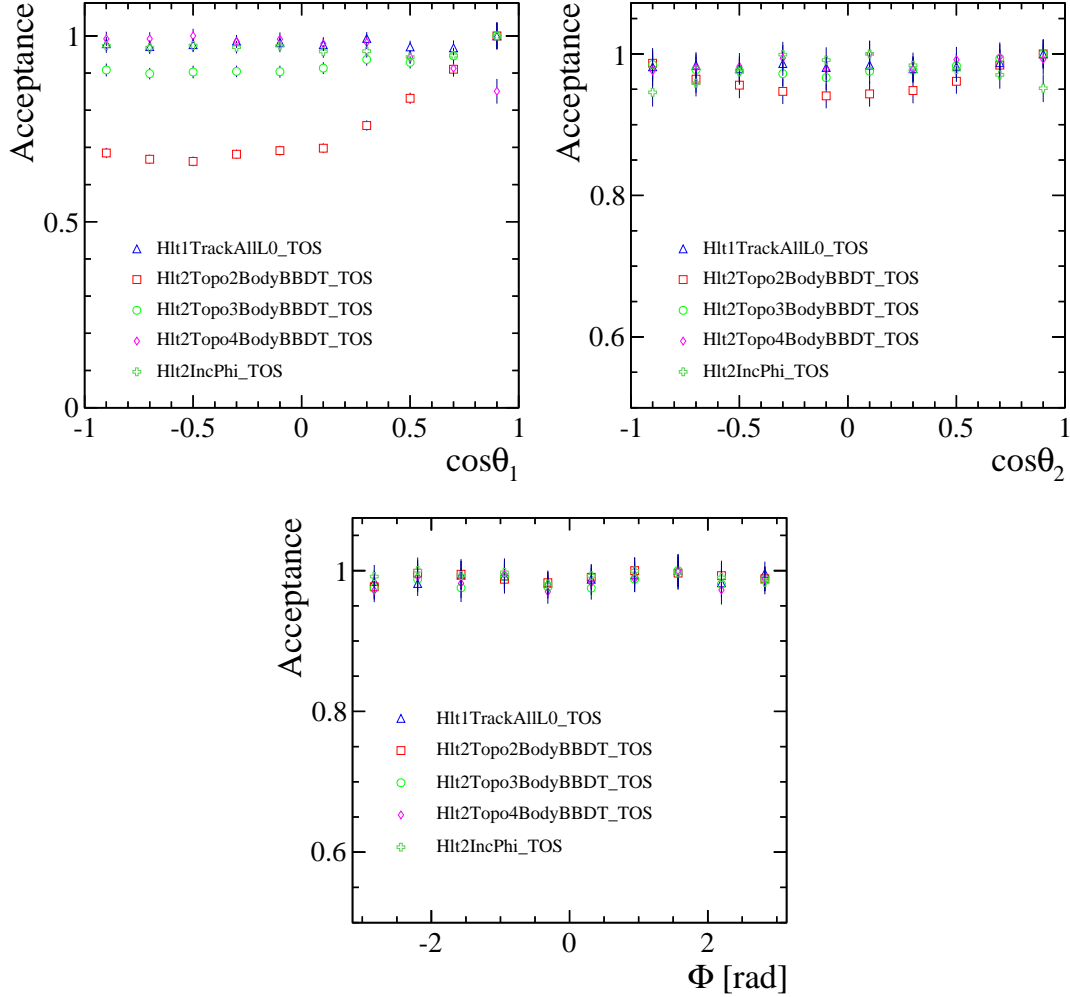
Figure 4.2: Distributions of the angular acceptance on $\cos\theta_1$, $\cos\theta_2$ and Φ. Simulated data with no cuts applied, fully stripped and selected are used in the calculation. Each line is then divided by the L0 acceptance, `L0Hadron_TOS` or `L0Global_TIS` depending on which trigger line the event is accepted. Since an event can simultaneously satisfy more than one trigger line, a single event can fill more than one histogram.
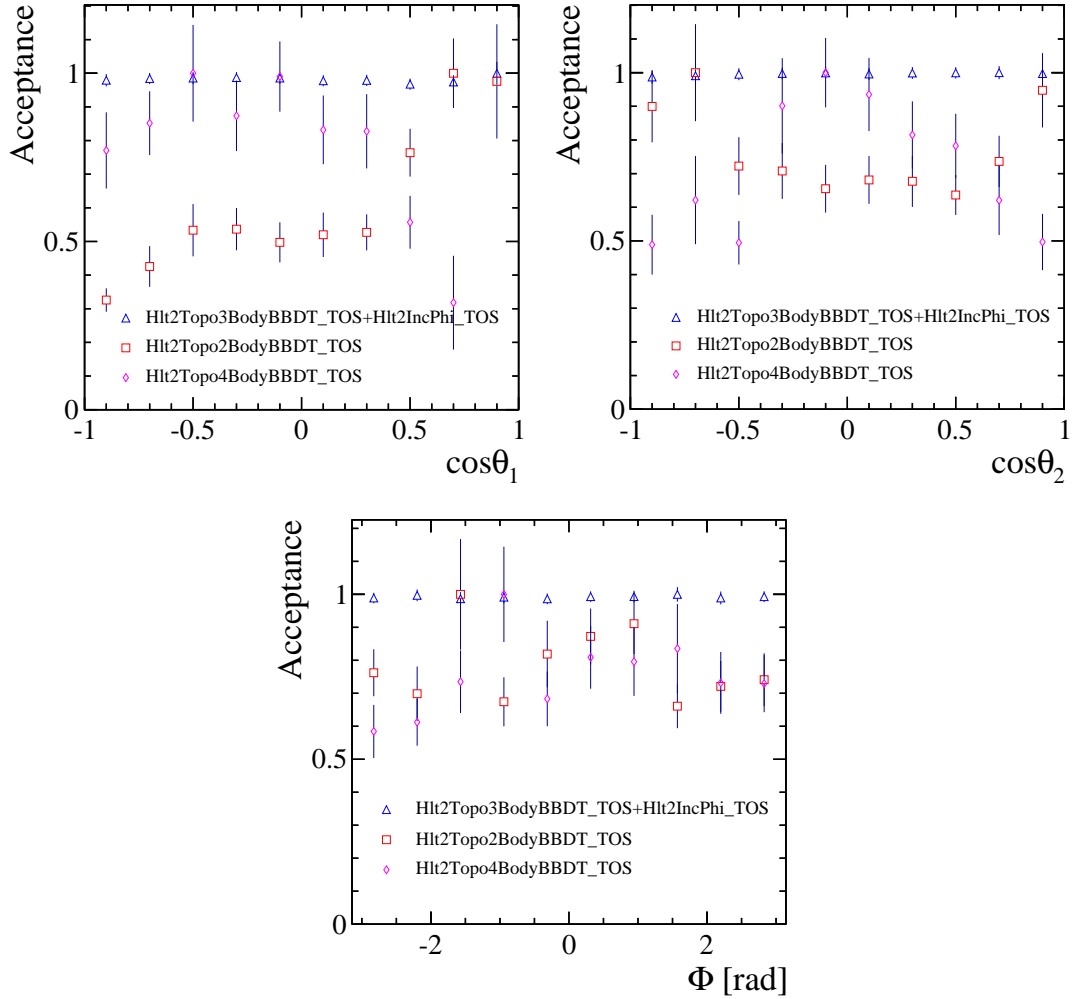
Figure 4.3: Distributions of the angular acceptance on $\cos\theta_1$, $\cos\theta_2$ and Φ. Simulated data with no cuts applied, fully stripped and selected are used in the calculation. Each line is then divided by the L0 acceptance, `L0Hadron_TOS` or `L0Global_TIS` depending on which trigger line the event is accepted. The histogram is filled such that each event can be in either `HLT2IncPhi_TOS` + `Hlt2Topo3BodyBBDT_TOS` or `Hlt2Topo2BodyBBDT_TOS` or `Hlt2Topo4BodyBBDT_TOS`.

4.3   Stripping and offline selection

To reconstruct the B^0 meson candidates in the exclusive decay $B^0 \to \phi K^*(892)^0$, the four reconstructed charged tracks are formed into ϕ and K^{*0} which are then combined into B^0 candidates. The stripping and final cuts are shown in Table 4.4. Reconstruction and selection criteria are discussed in the following.

Charged Tracks

The charged tracks are required to have transverse momentum p_T greater than $500 \, \text{MeV}/c$ and the quality of the track fit is required to have a $\chi^2_{track}/ndof$ smaller than 3. To remove the combinatorial background from particles originating from the Primary Vertex (PV), the products of b-hadron decays are required to have χ^2_{IP} with respect to any PV larger than 9, where χ^2_{IP} is the change in χ^2 of PV fit with and without the tracks from the signal. The ghost probability to reconstructed a track, which does not correspond to a real particle, is calculated. A requirement on this ghost probability, ProbNNghost < 0.5, allows to reject some more background. Misidentified particles are removed by requiring the kaons and pion to have a difference in the logarithm of the global Particle Identification (PID) Likelihood of the kaon hypothesis related to the pion hypothesis, the so-called Delta Log Likelihood ($\text{DLL}_{K\pi}$). This DLL information is provided by the RICH detector software. $\text{DLL}_{K\pi} < 0$ is required to select the pion in the $K^+\pi^-$ pair while $\text{DLL}_{K\pi} > 0$ is made to select the kaons that form the $\phi \to K^+K^-$ pair. For the kaon in the $K^+\pi^-$ pair, a tighter cut is applied, $\text{DLL}_{K\pi} > 2$, in order to reduce the combinatorial background under the K^{*0} hypothesis.

ϕ Mesons

The ϕ meson candidates are reconstructed using charged kaon pairs with a K^+K^- invariant mass within $\pm 15 \, \text{MeV}/c^2$ of the nominal ϕ mass from the PDG. The common vertex fit must be good and characterized by a χ^2_{vtx} per degree of freedom lower than 9. Finally, the transverse momentum p_T of the ϕ must be larger than $900 \, \text{MeV}/c$.

$K^*(892)^0$ Mesons

Similarly, the $K^*(892)^0$ meson candidates are formed using an kaon-pion pair of opposite charges with a $K^+\pi^-$ invariant mass within $\pm 150 \, \text{MeV}/c^2$ of the nominal $K^*(892)^0$ mass from the PDG. The same criteria as for ϕ meson are applied for p_T and for the vertex reconstruction of the $K^*(892)^0$.

B^0 Mesons

The final step of the selection is to combine the ϕ meson with $K^*(892)^0$ meson to build the B^0 meson candidate with the invariant mass in the range [5150, 5600] MeV/c^2. The fit of the common vertex, originated from the four daughter particles, is required to have the χ^2 per degree of freedom ($\chi^2_{vtx}/ndof$) smaller than 10. To remove $B^0_s \to \phi\phi$ decays where a kaon has been misidentified as a pion, the invariant mass of the $K\pi$ pair is recalculated assuming that both particles are kaons (denoted as $m(KK)_{MID}$). If the resulting invariant mass satisfy the condition $|m(KK)_{MID} - m_\phi| < 15\,\text{MeV}/c^2$ where m_ϕ is the nominal ϕ mass, the candidate is rejected. A study for this peaking background is carried out in Section 5.1.2. Finally, the B^0 candidate is required to be displaced from the associated PV with a flight distance significance (FDS)[1] more than 10, a lower cut on proper time $\tau_{B^0} > 0.2$ ps, and the B^0 momentum vector is required to point back towards the PV with a distance of closest approach (DOCA) less than 0.3 mm and $\chi^2_{\text{IP}} < 5$.

There are approximately 13000 candidates remain after the offline selection applied. The distribution of these candidates in $KKK\pi$ invariant mass is shown in Figure 4.4.
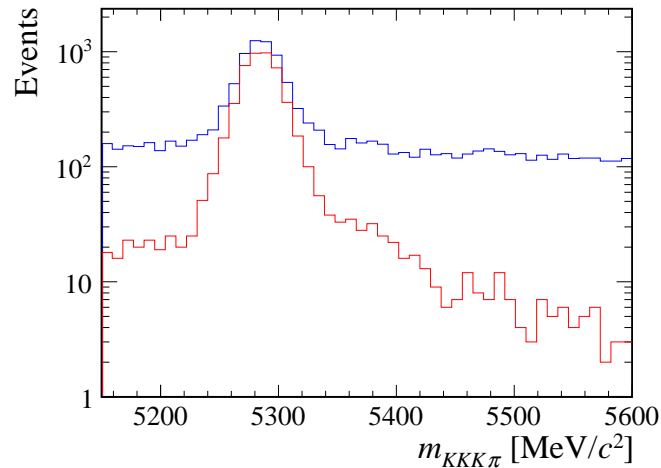
Figure 4.4: Invariant mass distribution of $KKK\pi$ after offline selection (see Section 4.3) (blue histogram) and after the BDT (see Section 4.4) has been applied (red histogram).

---

[1]FDS $= FD/\sigma_{FD}$, where FD is flight distance and σ_{FD} is the FD error.

	Stripping value	Final value
All tracks ProbNNghost	-	< 0.5
All tracks p_T	> 500 MeV/c	-
All tracks χ^2_{IP}	> 9	-
All tracks $\chi^2_{track}/ndof$	< 3	-
$DLL_{K\pi}(K^\pm$ from $\phi)$	> 0	-
$DLL_{K\pi}(K^\pm$ from $K^{*0})$	> 0	> 2
$DLL_{K\pi}(\pi^\pm)$	< 10	< 0
ϕ mass window	± 25 MeV/c^2	± 15 MeV/c^2
ϕ p_T	> 900 MeV/c	-
ϕ $\chi^2_{vertex}/ndof$	< 9	-
K^{*0} mass window	± 150 MeV/c^2	± 150 MeV/c^2
K^{*0} p_T	> 900 MeV/c	-
K^{*0} $\chi^2_{vertex}/ndof$	< 9	-
B^0 mass window	± 500 MeV/c^2	$[5150, 5600]$ MeV/c^2
B^0 p_T	-	> 2 GeV/c
B^0 τ	-	> 0.2 ps
B^0 DOCA	< 0.3 mm	-
B^0 $\chi^2_{vertex}/ndof$	< 15	< 10
B^0 χ^2_{IP}	-	< 5
B^0 flight distance significance	-	> 10
$|m(KK)_{MID} - m_\phi|$	-	> 15 MeV/c^2

Table 4.4: Stripping and final cuts to select $B^0 \to \phi K^*(892)^0$ events. The sign "-" stands for no-cut applied.

4.4 Multivariate analysis

Multivariate analysis (MA) is a statistical technique, implemented to extract the maximum information from each of the input variables in order to optimally separate the signal and the background samples where the signal sample is a simulated one and the background is the reconstructed events in the upper part of the B^0 mass spectrum. Several multivariate methods were tested, such as Likelihood method, Fisher discriminant, Multilayer Perceptron (MLP) and Boosted Decision trees (BDT) [60]: we have found that the BDT has the best performance as shown in Figure 4.6.

Boosted Decision trees

The goal is to classify data events into signal and background with a given number of input variables. A decision tree is a sequence of binary splits of the data. The data sample is divided into two parts: the training and testing samples. The training sample is used to train the decision tree, and the testing sample to test and evaluate the final classifier after the training phase. For each event, the split is done depending on the input variable that gives the best separation into one side having likely signal and other likely background. The process is repeated until the final nodes optimize the signal and background separation. Although, the decision tree is powerful, it is also an unstable method as small change in the initial training sample can produce a large change in the tree. This problem can be solved by using a boosting algorithm. If the training events are misclassified, *e.g.* a signal event fall in background leaf or vice versa, their weights increase (boosted) to form a new tree. This procedure is repeated and many trees are built up. Finally, a single classifier is given by the average of the individual decision trees using the tree scores as weight.

In this analysis, the Toolkit for Multivariate Analysis (TMVA) [89], provided by the ROOT Data Analysis Framework [90], is used for the training and evaluating of the BDT. The data and background samples as well as the input variables used for BDT training, are discussed in the following.

Signal and background samples

The BDT is trained using a sample of simulated $B^0 \to \phi K^*(892)^0$ signal events which has also passed the stripping selection and all the pre-selection cuts (see Table 4.4).

For the background, we take the reconstructed real data events which is selected from the upper mass sideband of the B^0 mass spectrum, $m_{KKK\pi} > 5415$ MeV/c^2. This region

is entirely dominated by the combinatorial background and is not used in the subsequent analysis.

Input variables

The distributions for signal and background of all potential variables have been tested and eight of them have been chosen based on their discriminating power. The variables used to train the BDT are:

- The IP χ^2 of the B^0 candidate with respect to the PV, B^0 χ^2_{IP}.

- The distance of closest approach of the ϕ and K^{*0} trajectory, DOCA(ϕ,K^{*0}).

- The proper time of the decay of the B^0 candidate, B^0 τ, calculated using the distance between the primary and the secondary vertices.

- The transverse momentum of the B^0 candidate, B^0 p_T.

- The minimum IP χ^2 among the ϕ daughters, min(min K^+ χ^2_{IP}, min K^- χ^2_{IP}).

- The minimum IP χ^2 among the K^{*0} daughters, min(min K χ^2_{IP}, min π χ^2_{IP}).

- The cosines of the angle between the momentum of the B^0 candidate and its direction of flight from the best PV to the decay vertex, B^0 DIRA.

where the χ^2_{IP} is defined as $(\text{IP}/\sigma_{\text{IP}})^2$, σ_{IP} is the IP error. The χ^2_{IP} value results from the adjustment of the vertex and the momentum determination of the track. The IP significance is equal to $\sqrt{\chi^2_{\text{IP}}}$. In order to have a better shape, the logarithm is used in some cases.

The list of the input variables used in the training and their relative discriminating importance is summarized in Table 4.5. Figure 4.5 shows the signal and background distribution of the events used as input for the BDT training.

BDT optimization

The result of the training for the BDT, MLP, Likelihood and Fisher classifiers is shown in Figure 4.6 in term of background rejection versus signal efficiency. These curve have been obtained with the test sample containing events not used for training. Since the BDT classifier gives the best background rejection it is chosen for the analysis.

Figure 4.7 shows the BDT output distribution for the signal and background. From the plot, one can see that the test result and training sample give the same which is an
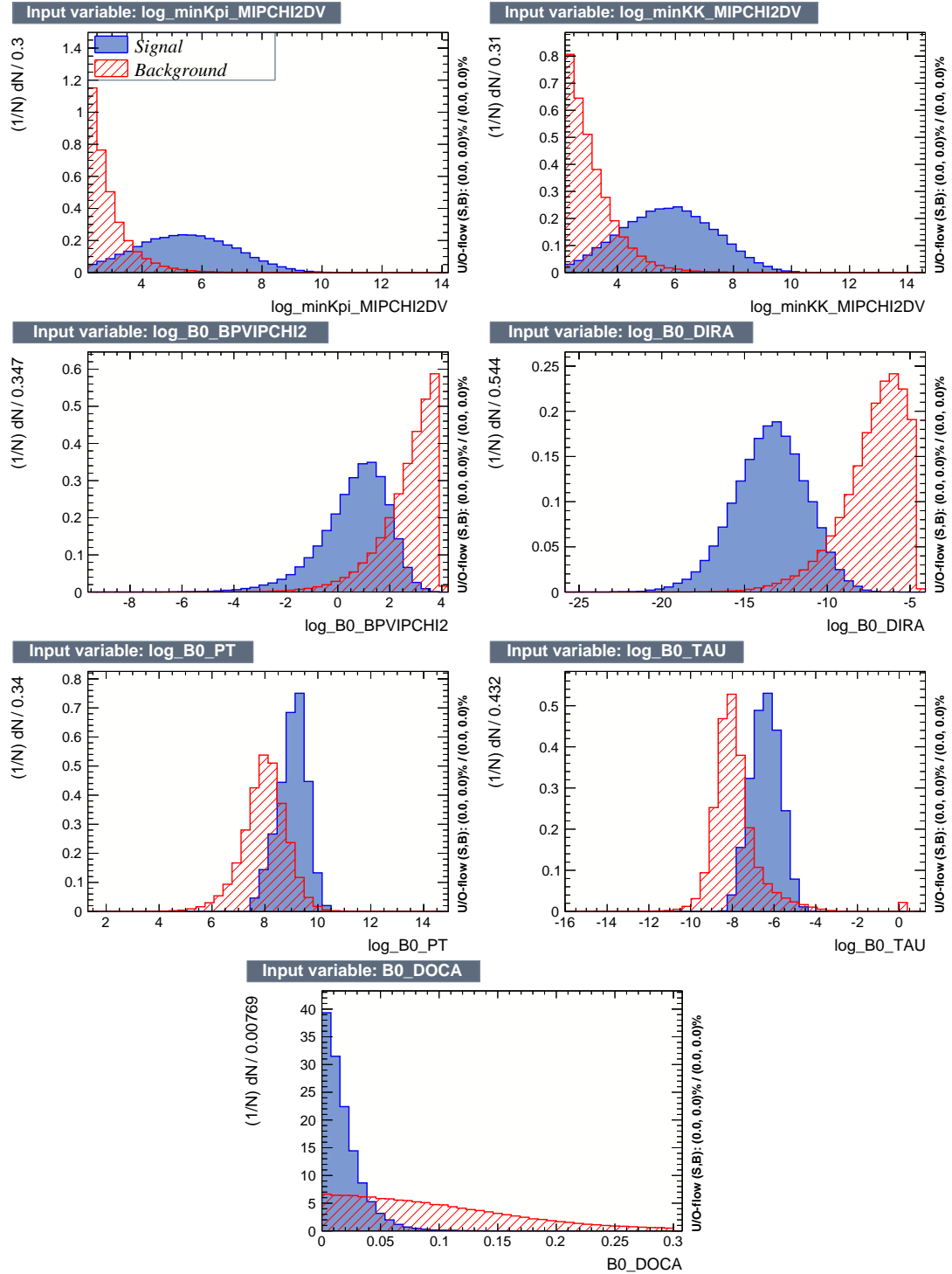
Figure 4.5: Distributions of the BDT input variables. The signal and background samples are in blue and red respectively.

Ranked	Variable	Variable Importance (%)
1	B^0 DIRA	19.57
2	B^0 p_T	18.32
3	B^0 τ	13.45
4	B^0 DOCA	11.62
5	B^0 χ^2_{IP}	10.12
6	$\min(\min K^+ \chi^2_{\mathrm{IP}}, \min K^- \chi^2_{\mathrm{IP}})$	9.47
7	$\min(\min K \chi^2_{\mathrm{IP}}, \min \pi \chi^2_{\mathrm{IP}})$	8.02

Table 4.5: Variables and their relative importance used in the training of the BDT for $B^0 \to \phi K^*(892)^0$ decay.

indication implies that the classifier is not over-training.

The efficiency for signal (blue curve) and background (red curve) of the BDT in the $B^0 \to \phi K^*(892)^0$ decay are shown in Figure 4.8. The choice of the cut applied on the BDT output is considered based on the Figure of Merit (FoM) value which is the ratio $S/\sqrt{S+B}$ (green curve in Figure 4.8), where S and B are the yields of signal and background candidates expected in the real data. After the stripping and offline selection, there are 13000 candidates remaining. The FoM was optimized supposing that there are 5000 signal events and 8000 background events in the full four-body invariant mass range. The maximum value for the FoM is found to be 69.38 for the BDT > 0.03. The signal efficiency for this point is 97%, the background retention 6.7%. After this step the data sample is reduced to 5100 candidates (see Figure 4.4) which will be used for angular-mass analysis.
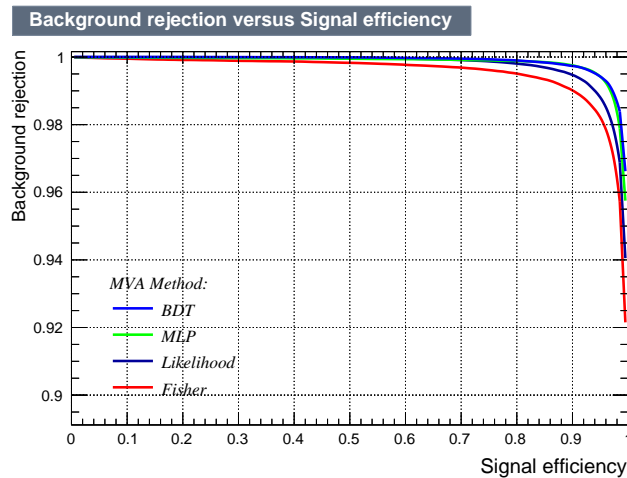
Figure 4.6: Background rejection vs. signal efficiency for four MVA methods: Boosted Decision trees (BDT), Multilayer Perceptron (MLP), Likelihood and Fisher discriminant.
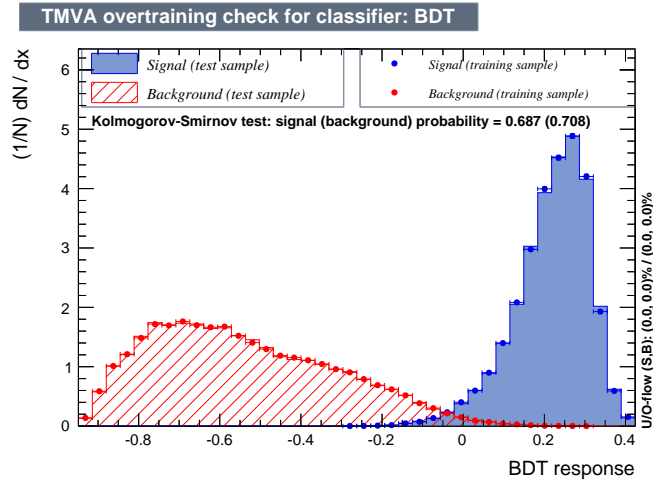
Figure 4.7: BDT output distribution: the distribution of the signal sample is in blue and the background distribution is in red; the points correspond to the training samples and the areas to the test samples.
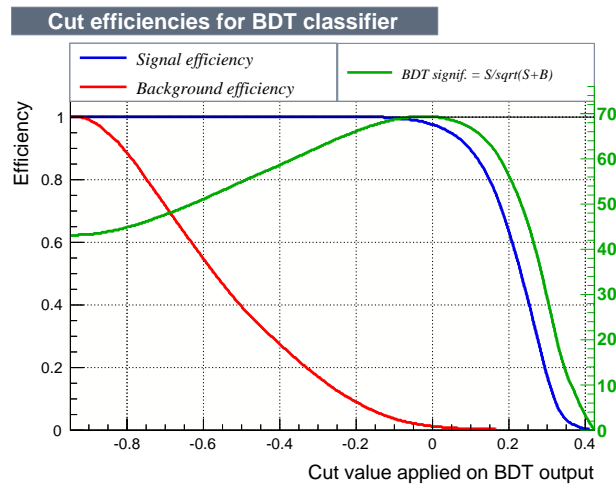
Figure 4.8: Efficiency of the signal and background, and Figure of Merit $(S/\sqrt{S+B})$ as a function of the BDT output response. S and B are the yields of signal and background candidates expected in the real data.

Chapter 5

Analysis of the $B^0 \to \phi K^*(892)^0$ decay

The analysis process of the $B^0 \to \phi K^*(892)^0$ decay is separated in two steps. In the first step, an unbinned maximum likelihood method is used to fit the $KKK\pi$ mass distribution. The fit model of the $KKK\pi$ mass is described in Section 5.1.1: the signal is modelled by a combination of Crystal Ball and a wider Gaussian function with a common mean and the background is modelled by an exponential function; we make here the assumption that the background contribution is mainly combinatorial. Furthermore, a background study is initiated in Section 5.1.1; the low mass background (or partially reconstructed background) can be eliminated by limiting the $KKK\pi$ invariant mass and the peaking background is negligible in the signal region. The fit is performed to the total sample, without separating the events in categories. The results from this fit can be used to unfold the combinatorial background from data and will be used for angular-mass fit.

In the second step, an unbinned maximum likelihood fit is then made to the three decay angles, the KK and $K\pi$ masses to extract the physics parameters. In order to subtract combinatorial background from data the *sPlot* technique [91] with the $KKK\pi$ invariant mass as the control variable is used. Data are then separated in four categories, depending on the flavour of the B^0 meson and the trigger category. A simultaneous fit to the four subsamples using the model described in Section 3.1.3 is used to perform the angular mass fit. Then, the polarization amplitudes and phases, CP asymmetries as well as triple-product asymmetries are derived. Systematic uncertainties on the measurement are then discussed in details; contributions of various sources to the systematics, the acceptance correction, the $KKK\pi$ mass model, the difference in kinematic variables between data and simulation and the S–*wave* lineshape, will be presented.

5.1 Mass fit for $B^0 \to \phi K^*(892)^0$

5.1.1 Signal yield for the decay $B^0 \to \phi K^*(892)^0$

To extract the signal, which will be used in the angular analysis, an unbinned maximum likelihood fit to the $K^+K^-K^+\pi^-$ invariant mass distribution is made. The model for the $B^0 \to \phi K^*(892)^0$ signal is a sum of a Crystal Ball (CB) [92] and a wider Gaussian function with a common mean; this can be written as

$$S(m) = f_{CB}CB(m) + (1 - f_{CB})G(m) \ , \tag{5.1}$$

where f_{CB} is the fraction of the Crystal Ball in the fit, $CB(m)$ and $G(m)$ are the Crystal Ball and Gaussian function respectively. They are defined as follows

$$CB(m) = N_{CB} \begin{cases} \exp\left(-\frac{(m-m_B)^2}{2\sigma_{CB}^2}\right), & \text{if } m > m_B - |a|\sigma_{CB} \\ \left(\frac{n}{|a|}\right)^n \exp\left(-\frac{|a|^2}{2}\right)\left(\frac{n}{|a|} - |a| - \frac{m-m_B}{\sigma_{CB}}\right)^{-n}, & \text{if } m \leqslant m_B - |a|\sigma_{CB} \end{cases}$$

$$G(m) = N_G \exp\left(-\frac{(m-m_B)^2}{2\sigma_G^2}\right), \tag{5.2}$$

where m_B is the mean of the B^0 or B_s^0, σ_{CB} is the width of the Crystal Ball, n is the exponent of the exponential tail and a the transition point at which the function changes from the Gaussian to the exponential, while σ_G is the width of the Gaussian. N_{CB} and N_G are the normalization factor of the Crystal Ball and Gaussian PDF, respectively.

Figure 5.1 shows the fit model described above applied to simulated data, $B^0 \to \phi K^*(892)^0$. The parameters extracted from the fit such as the width and the relative fraction $(1 - f_{CB})$ of the Gaussian and the parameters of the Crystal Ball (a, n) are fixed in the real data fit. These parameters and their values are shown as fixed parameters in the Table 5.1. The width of the Crystal Ball is left free in the fit. The contribution from the decay $\overline{B}_s^0 \to \phi K^*(892)^0$ is also included into the fit. The fit model used for the B_s^0 is the same for the B^0. In other words, all the parameters of the fit model for the B_s^0 are kept in common with the B^0 signal, excepted the mean of the B_s^0 which is fixed relative to the mean of the B^0 as: $m_{B^0}^{Fit} + (m_{B_s^0} - m_{B^0})$ where $m_{B^0}^{Fit}$ is the B^0 mean (a free parameter from the fit), and $m_{B^0_{s,d}}$ are the mean values of B_s^0 and B^0 mesons taken from PDG [27].

The mass range of $K^+K^-K^+\pi^-$ distribution used in the fit is chosen to be between 5150-5600 MeV/c^2 in order to eliminate the low mass background (see Section 5.1.2) from reconstructed B decays with a missing pion or photon. Since after the final selection the
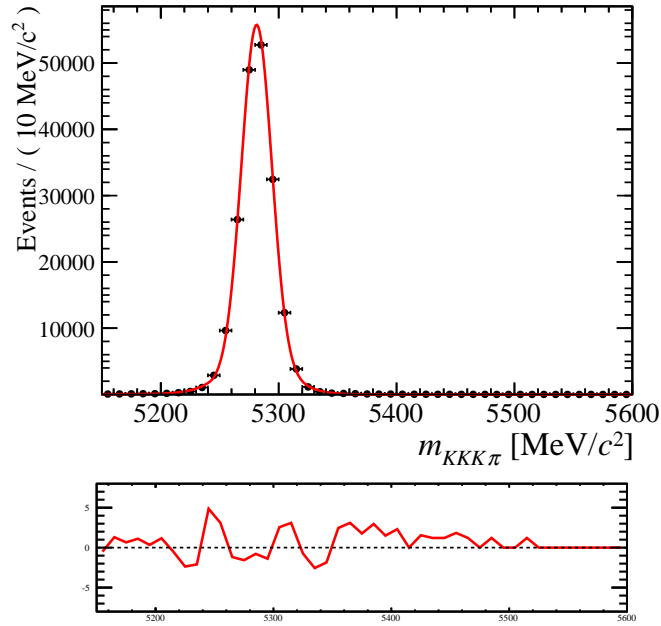
Figure 5.1: Invariant mass distribution of the simulated $B^0 \to \phi K^*(892)^0$ (after full stripping and final selection have been applied) fitted with a model of Crystal Ball and Gaussian described in the text. Bottom shows the pull distribution resulting from the fit.

background is almost completely combinatorial, it can be modelled using an exponential function.

After the stripping and the final selection, 5100 events are found in the mass range 5150-5600 MeV/c^2. An unbinned maximum likelihood fit to the data is used to extract the signal parameters. The fit results, which do not differentiate B^0 from $\overline{B}^0$, are shown in Table 5.1. A yield of 4467 ± 69 B^0 signal candidates is obtained from the fit. The ratio of the yields between B_s^0 and B^0 ($N_{B_s^0}/N_{B^0}$) is found to be 0.022 ± 0.003 which is similar to the result (0.024 ± 0.005) from the LHCb measurement based on an integrated luminosity of 1.0 fb^{-1}. The $KKK\pi$ invariant mass distribution is shown in Figure 5.2 with the fit result superimposed.

5.1.2 Background study

Low mass background

In $B^{0(\pm)} \to \phi K_j^{(*)}$ decays, many high mass $K_j^{(*)}$ can decay to $K^*(892)^0$ and an emitted π, *e.g.* $K_1(1270)$, $K_1(1400)$, $K^*(1410)$, $K_2^*(1430)$, $K_2(1770)$ and $K_2(1820)$. If the pion is
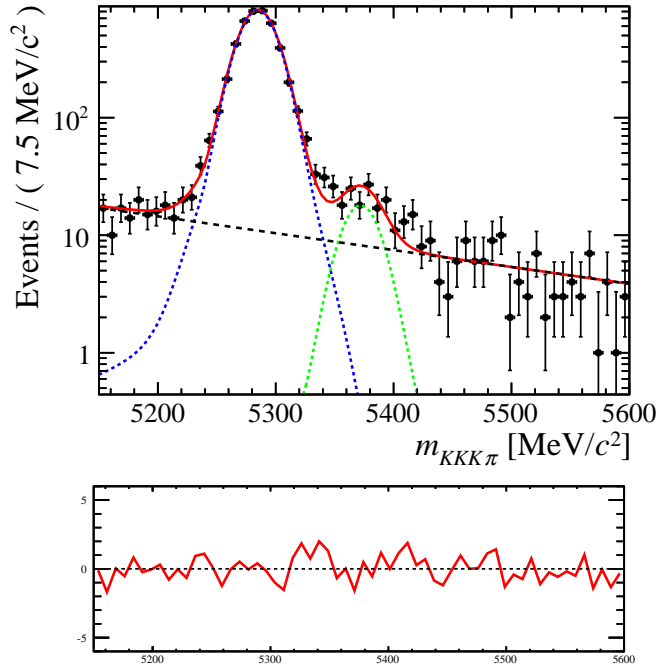
Figure 5.2: Invariant mass distribution of selected $KKK\pi$ candidates. A fit to the model described in the text is superimposed (red solid line). The signal contribution is shown as the blue dotted line. The contribution from combinatorial background is shown in dark dashed line. The contribution from $B_s^0 \rightarrow \phi \overline{K}^*(892)^0$ is also shown in green dotted line. The pull distribution resulting from the fit is small as shown below.

missing in the B^0 reconstruction from a true ϕ and a $K^*(892)^0$, an accumulation in the low mass region is generated as we can see in Figure 5.3. This partially reconstructed background is modelled with an ARGUS function [93] convolved with a Gaussian resolution having the same width as the signal (σ_{ARGUS}, see Table 5.2). The ARGUS probability density as a function of the invariant mass (x) is given by

$$A(x) = x \left[1 - \left(\frac{x}{m_{\mathrm{ARGUS}}} \right)^2 \right]^p \cdot \exp \left[c \left(1 - \left(\frac{x}{m_{\mathrm{ARGUS}}} \right)^2 \right) \right], \qquad (5.3)$$

where m_{ARGUS} is the endpoint of the ARGUS distribution and p and c (the "power" and the "curvature" parameters) are the ARGUS function parameters.

A fit is made to the mass range 5000-5600 MeV/c^2, using the model described in Section 5.1.1 to which an ARGUS function is added to model the low mass background. Figure 5.3 shows the result of the fit. The ARGUS fitted parameters are given in Table 5.2. Although in this analysis the B^0 candidates are selected in the mass range

Fit Parameter	Status	Value
N_{B^0}	Free	4467 ± 69
$N_{B_s^0}$	Free	98 ± 15
N_{bkg}	Free	535 ± 33
m_{B^0}	Free	5284.8 ± 0.3 MeV/c^2
f_{cg}	Fixed	0.856
σ_{CB}	Free	15.3 ± 0.3 MeV/c^2
a	Fixed	2.88
n	Fixed	1
σ_G	Fixed	26.5 MeV/c^2
λ	Free	$-3.31 \times 10^{-3} \pm 3.74 \times 10^{-4}$

Table 5.1: Parameters and their fixed and fitted values using in the fit of B^0 invariant mass distribution. Where m_{B^0} is the mean of the B^0 peak, f_{cg} is the fraction of the Crystal Ball $(1 - f_{cg}$ is the fraction of the Gaussian), σ_{CB} is the width of the Crystal Ball, a and n are Crystal Ball parameters, σ_G is the width of the signal Gaussian distribution. λ is the parameter which describes the slope of the background.
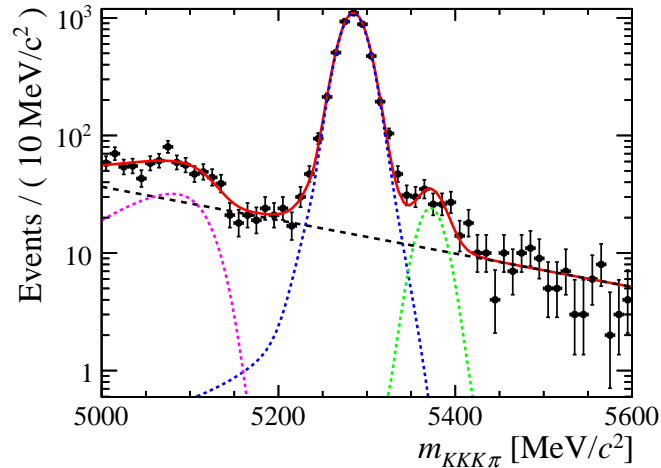
Figure 5.3: The $KKK\pi$ invariant mass distribution after the stripping and selection have been applied in the mass range 5000-5600 MeV/c^2. The distribution is fitted by the model described in Section 5.1.1 with the inclusion of an the ARGUS function (dotted magenta).

5150-5600 MeV/c^2, the yield of the ARGUS distribution in this region is found to be 4 events. To test the effect of this low mass contribution on the fit model applied to the signal the following study was carried out (more details in Section 5.3.2). All the parameters of the ARGUS function from the fit in the mass range 5000-5600 MeV/c^2 are fixed in the *sPlot* technique (see Section 5.2) which is used to unfold the signal and background in a fit range 5150-5600 MeV/c^2. The new weighted dataset is then used in the angular-mass distribution fit. The deviation from the nominal result is considered as

Parameter	Value	
ARGUS yield	355 ± 55	$\in [5000, 5600]$ MeV/c^2
	3.5 ± 0.5	$\in [5150, 5600]$ MeV/c^2
m_{ARGUS}	5135	MeV/c^2
σ_{ARGUS}	17.4	MeV/c^2
p	0.81	
c	-41.68	

Table 5.2: Table showing the ARGUS parameters and their values used in fit model. σ_{ARGUS} is the width of the Gaussian which is used to convolve with the ARGUS, is calculated as $[f_{CB}\sigma_{CB}^2 + (1 - f_{CB})\sigma_{Gauss}^2]^{1/2}$, where $\sigma_{CB,Gauss}$ are the widths of the Crystal Ball and Gaussian functions used in fit to the signal model and f_{CB} is the fraction of the Crystal Ball.

a systematic error caused by the low mass background.

Peaking background

A. Contribution from $B_s^0 \to \phi\phi$

The major source of background expected in the B^0 mass peak for the decay $B^0 \to \phi K^*(892)^0$ is the decay $B_s^0 \to \phi(K^+K^-)\phi(K^+K^-)$, where one kaon is misidentified as a pion.

The $K\pi$ invariant mass recalculated assuming the KK hypothesis ($m(KK)_{MID}$) is shown on the left of Figure 5.4. A clear peak is observed at the nominal ϕ mass. By using all events in the mass window of $|m(KK)_{MID} - m_\phi| < 15$ MeV/c^2, the $KKKK$ mass reconstructed with a pion misidentified as a kaon is shown on the right. A misidentified events peak is also seen under the B_s^0 mass. These informations suggest a contribution from $B_s^0 \to \phi\phi$ decay.

To quantify the number of $B_s^0 \to \phi\phi$ candidates which could be found in the dataset, 1 million $B_s^0 \to \phi\phi$ MC events have been reconstructed and selected in an identical way to the data. After the final selection a yield of the 171 events has been found. This gives a "probability" of misidentifying the $B_s^0 \to \phi\phi$ events as $KKK\pi$ events of 1.71×10^{-4}.

Parameter	Value
$\sigma_{b\bar{b}}^{acc}$	$75.3 \pm 5.4 \pm 13.0$ μb [94]
f_s	0.103 ± 0.009 [95]
$BR(B_s^0 \to \phi\phi)$	$(1.91 \pm 0.31) \times 10^{-5}$ [95]
$BR(\phi \to K^+K^-)$	0.489 ± 0.005 [95]

Table 5.3: Reference values used in equation 5.4.
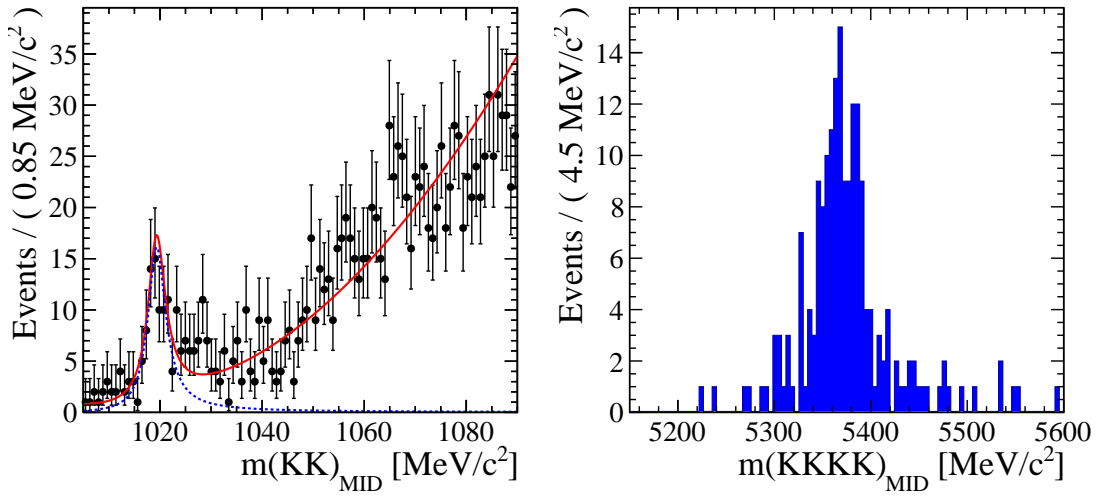
Figure 5.4: The invariant KK (left) and $KKKK$ mass (right) distribution taken from data, after a pion misidentified as a kaon. Note that events on the $KKKK$ mass distribution are in the mass window of $|m(KK)_{MID} - m_\phi| < 15$ MeV/c^2. A fit to the $m(KK)_{MID}$ spectrum yields 115 events in the peak (dotted blue line). Total fit is solid red line.

The number of expected $B_s^0 \to \phi\phi$ events to be produced in 2.08 fb^{-1} of pp collision data in the LHCb detector can be written as

$$N_{B_s^0 \to \phi\phi} = 2 \times \mathcal{L}_{int} \times \sigma_{b\bar{b}}^{acc} \times f_s \times BR(B_s^0 \to \phi\phi) \times BR(\phi \to K^+K^-)^2 , \qquad (5.4)$$

where $\mathcal{L}_{int}$ is the integrated luminosity, $\sigma_{b\bar{b}}^{acc}$ is the cross section of b hadrons produced in the LHCb acceptance and f_s is the probability for a b-quark to produce a B_s^0 meson. The factor 2 which appears in Equation (5.4) accounts for the fact that the b-quark as well as the $\bar{b}$-quark may hadronize into B_s^0 (or $\overline{B}_s^0$). Using the values in Table 5.3 to equation 5.4, we get 141691 $B_s^0 \to \phi\phi$ events. The number of events with $KKK\pi$ in the final state is then:

$$N_{B_s^0 \to KKK\pi} = N_{B_s^0} \times \epsilon \times 4 , \qquad (5.5)$$

where ϵ is the "probability" obtained from Monte Carlo and the factor 4 accounts for the fact that any of the four kaons can be misidentified as a pion. We get an expected number of $KKKK$ final state of 96 events in the 2.08 fb^{-1} dataset.

In addition, a fit is perform to the KK_{MID} distribution taken from data where the signal is used the resonant ϕ mass (see Section 3.1.2) and the continuum is described by a Chebyshev polynomial, $1 + \sum_{i=0,1} a_i T_i(x)$, where the coefficient a_i are determined and fixed from simulation. The parameters of the resonant ϕ mass, taken from Table 3.2, are

also fixed in the fit. The fit result is shown on Table 5.4 and Figure 5.4. There are about 115 events of the KK_{MID} peak have been found in the data. This is consistent with the expected number (96 events) of $KKKK$ final state calculated in the text.

Parameter	Status	Value
$N_{KK}(MID)$	Free	115 ± 14
N_{bkg}	Free	1145 ± 35
ϕ resonance	fixed	Table 3.2
a_0	Fixed	1.31
a_1	Fixed	0.36

Table 5.4: Fit results obtained from a fit to the KK_{MID} invariant mass.

To remove the contribution form $B_s^0 \to \phi\phi$ decay a selection veto on events within ± 15 MeV/c^2 of the KK_{MID} mass has been applied (see Section 4.3).

B. Contribution from $B^0 \to D_s^\pm K^\mp$

The decay $B^0 \to D_s^\pm K^\mp$ where D_s^+ decays to $K^+K^-\pi^+$ and $\phi(K^+K^-)\pi^+$ final states with branching ratio $5.5 \pm 0.27\%$ and $2.32 \pm 0.14\%$ [27] respectively, is a possible source of background to $B^0 \to \phi K^*(892)^0$. Figure 5.5 shows the invariant mass of the $KK\pi$ system obtained from the data and Monte Carlo simulating the decay $B^0 \to \phi K^*(892)^0$; in the later, a kaon pair form a ϕ meson which is combined to a pion from $K^*(892)^0$. A peak is observed near 1968.3 MeV/c^2 in the data and suggests a contribution from $D_s^\pm$ mesons. As the continuum in Figure 5.5 is well reproduced by the Monte Carlo, we assume that it comes from $B^0 \to \phi K^*(892)^0$ events with a wrong association.

To estimate the number of $D_s^\pm$ events ($B^0 \to D_s^\pm K^\mp$), the peak of Figure 5.5 and 5.6 is fitted by a Gaussian distribution whose mean is taken from the PDG [27] and whose width is from an earlier LHCb paper [96]. The continuum is modelled by a Chebyshev polynomial, $1 + \sum_{i=0,1} c_i T_i(x)$, where the coefficient c_i are determined and fixed from simulation.

The observed number of $D_s^\pm$ is 41 ± 7 events (see Table 5.5). When limiting to a window of ± 20 MeV/c^2 around 1968.3 MeV/c^2, we obtain 75 events ($D_s^\pm$ + Continuum) as shown in Figure 5.7 overlaid onto the full $KKK\pi$ mass spectrum. However these events are dispersed in the $B^0 \to \phi K^{*0}$ spectrum and only 35 events fall in the signal region of ± 45 MeV/c^2 around the nominal B^0 mass. This contributes only 0.7% of the signal yield. In addition, the angular-mass analysis is also performed using data after veto events in mass window of ± 15 MeV/c^2 around the $D_s^\pm$ nominal mass ($|m(KK\pi) - m_{D_s^\pm}| > 15$).

The difference compared to the main results is small, therefore the contamination from $B^0 \to D_s^\pm K^\mp$ can be considered to be negligible.
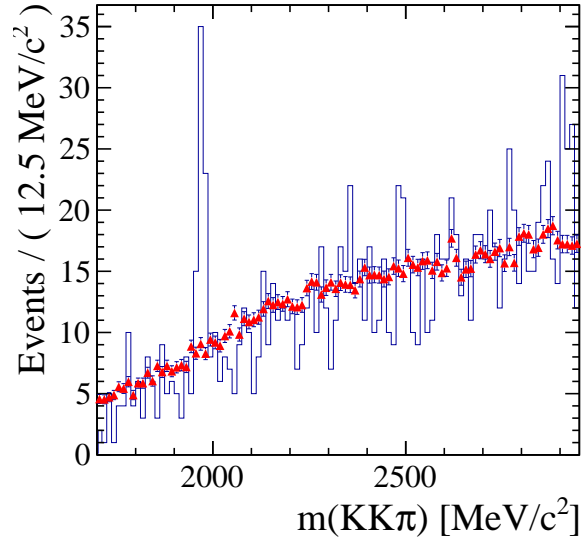
Figure 5.5: Invariant mass of the $KK\pi$ system which was combined by the kaon pair associated with ϕ meson and the pion from K^{*0}. The histogram taken from data (blue) is compared to Monte Carlo (red) which is normalized to the number of events seen in the data. A peak is observed near 1968.3 MeV/c^2, which is the averaged mass of the $D_s^\pm$ meson [27].

Parameter	Status	Value
$N_{D_s^\pm}$	Free	41 ± 7
N_{bkg}	Free	1203 ± 35
$\sigma_{D_s^\pm}$	Fixed	6.72 MeV/c^2
$m_{D_s^\pm}$	Fixed	1968.5 MeV/c^2
c_0	Fixed	0.55
c_1	Fixed	-0.12

Table 5.5: Fit results obtained from a fit to the $KK\pi$ invariant mass.

C. Possible contribution from double Mis-ID in $K^+\pi^-$ system

A test for contribution from double misidentified, the kaon and pion mass hypothesis are swapped, in $K^+\pi^-$ system is carried out. Figure 5.8 shows the invariant mass of the $K\pi$ system after the pion and kaon have been double misidentified in data compared to the simulation. No peak is observed at the nominal $K^*(892)^0$ mass and consistent with the simulation indicating that there are no real $K^*(892)^0$ events with a double misidentification hypothesis.
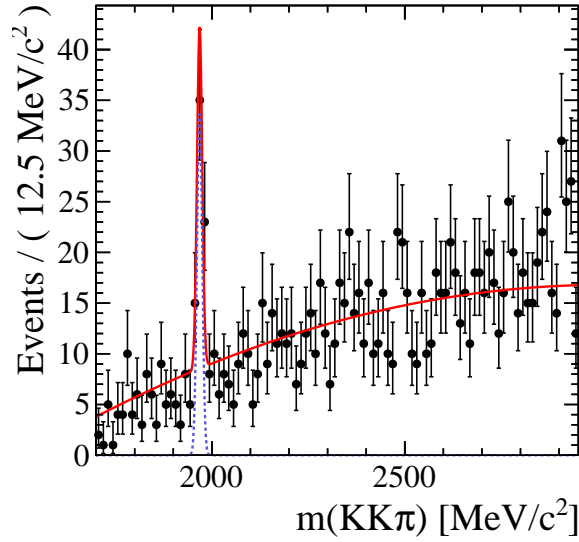
Figure 5.6: Invariant mass distribution for the $KK\pi$ candidates taken from data. A fit to the Gaussian signal and Polynomial background described in the text is superimposed (red solid line). The signal contribution is shown as the blue dotted line.
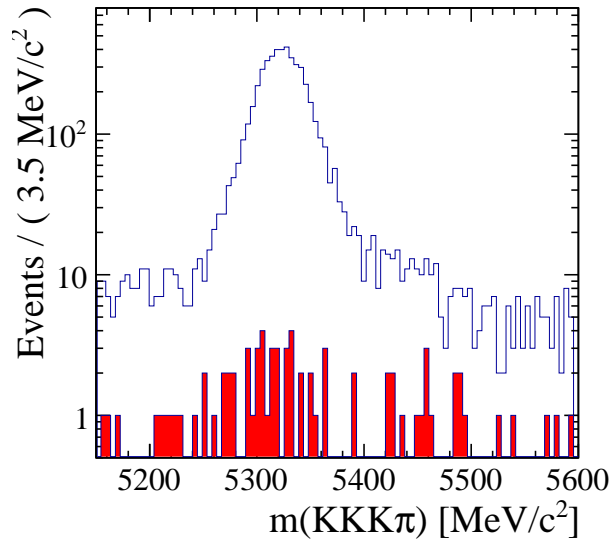
Figure 5.7: Invariant $KKK\pi$ mass distribution (white histogram) of the real data (after full stripping and final selection) overlayed with events containing a possible $D_s^{\pm}$ meson (red histogram).

D. Possible three-body contributions

All possible contributions of three-body is also studied in data such as KKK and $KK\pi$ systems where the KK were associated to the ϕ meson, $K\pi K$ system where the $K\pi$ was previously associated with the $K^*(892)^0$ meson. Figures 5.9, 5.10 and 5.11 show
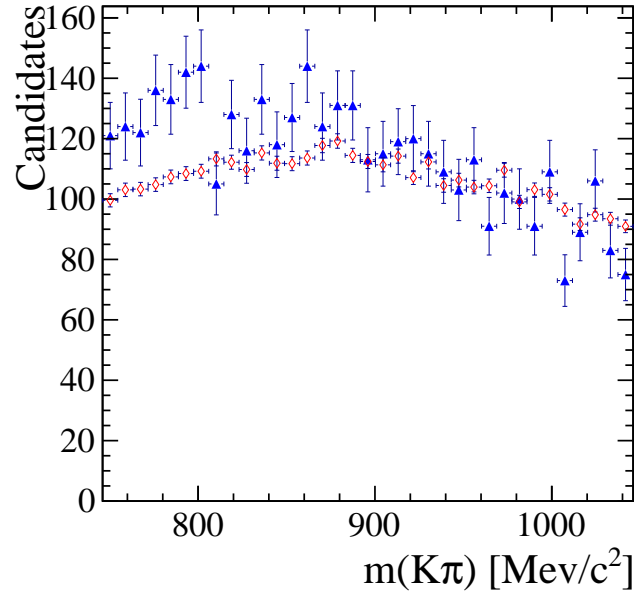
Figure 5.8: Invariant $K^+\pi^-$ mass distributions taken from data (blue), compared with simulation (red) with the pion and kaon mass hypotheses are swapped. No peak is observed at the nominal $K^*(892)^0$ mass and consistent with simulation indicating no real $K^*(892)^0$ from double misidentification.

the comparison of Dalitz-like distributions between data and Monte Carlo where all the offline cuts as well as a addition cut of ± 45 MeV/c^2 around the nominal B^0 mass have been applied. The consistency between data and Monte Carlo distributions is observed indicating that no contamination from three-body decay exists in the data sample.
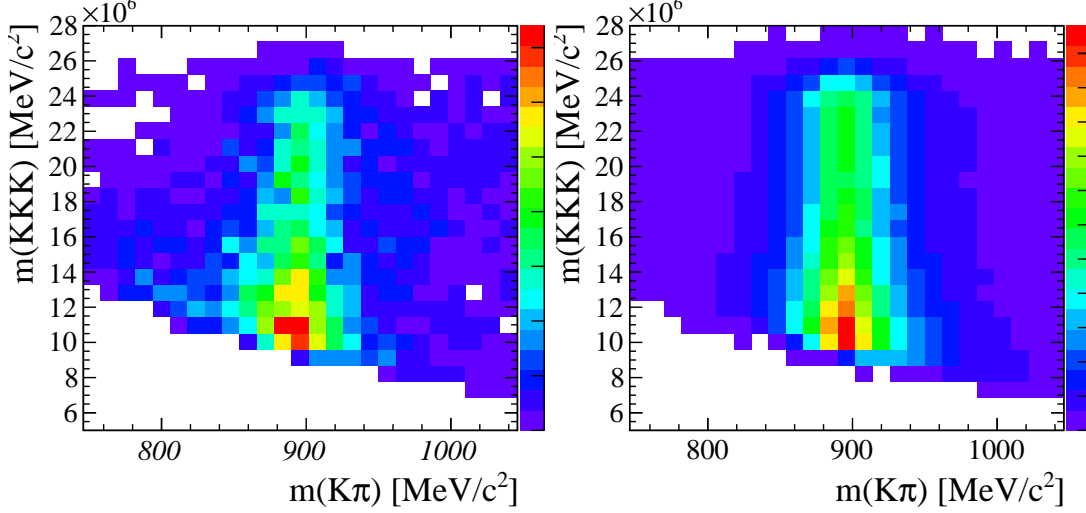
Figure 5.9: Invariant KKK mass versus $K\pi$ mass distributions taken from data (left), compared with Monte Carlo (right) where an addition cut of ± 45 MeV/c^2 around the nominal B^0 is applied to the $KKK\pi$ invariant mass. The consistency between data and Monte Carlo distributions indicates that no particles decaying into KKK are in the dataset.
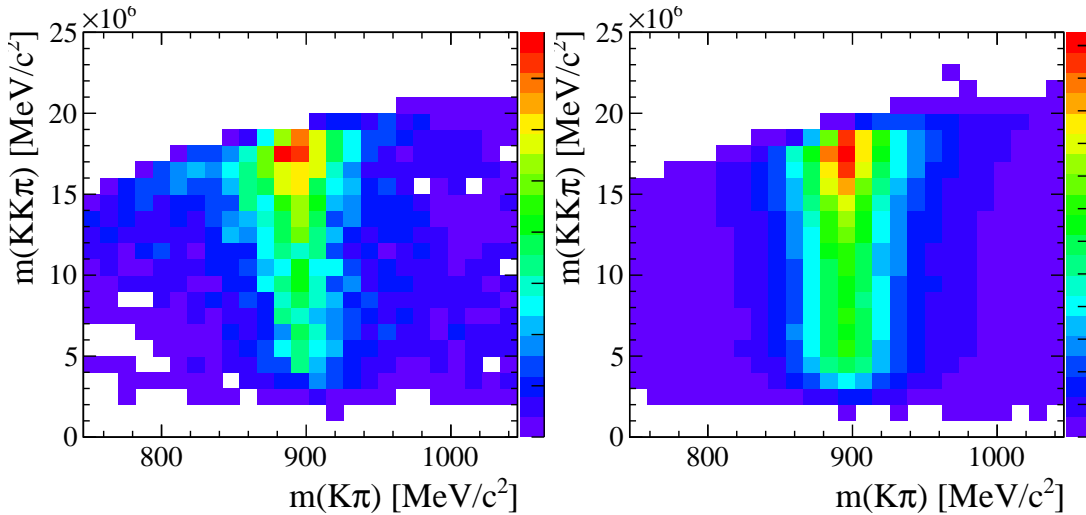
Figure 5.10: Invariant $KK\pi$ mass versus $K\pi$ mass distributions taken from data (left), compared with Monte Carlo (right) where an addition cut of ± 45 MeV/c^2 around the nominal B^0 is applied to the $KKK\pi$ invariant mass. The consistency between data and Monte Carlo distributions indicates that no particles decaying into $KK\pi$ are in the dataset.
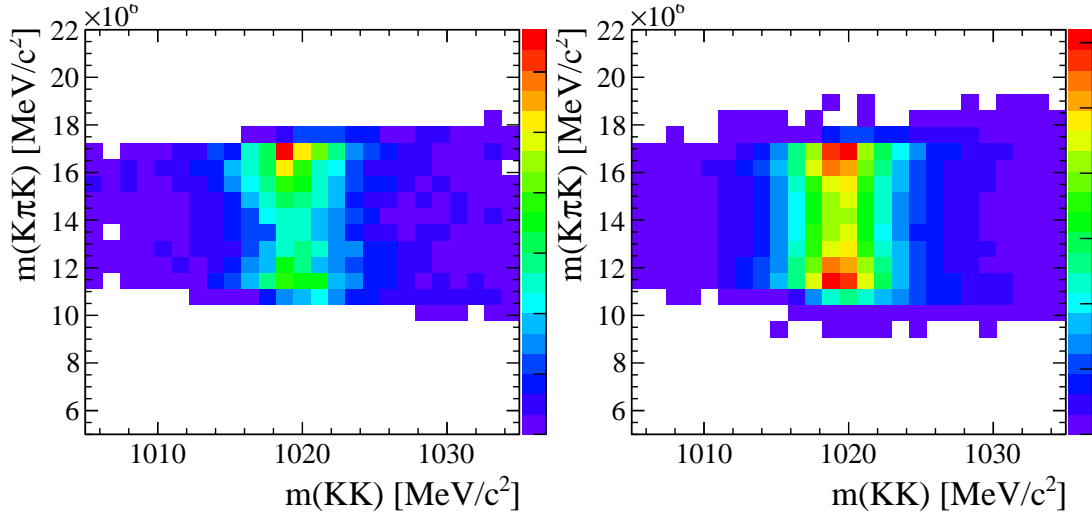
Figure 5.11: Invariant $K\pi K$ mass versus KK mass distributions taken from data (left), compared with Monte Carlo (right) where an addition cut of ± 45 MeV/c^2 around the nominal B^0 is applied to the $KKK\pi$ invariant mass. The consistency between data and Monte Carlo distributions indicates that no particles decaying into $K\pi K$ are in the dataset.

5.2 Angular-Mass fit results

The physics parameters used in this analysis have been defined in Table 3.4 which include the polarization amplitudes, the phases and the amplitude (squared) differences between B^0 and $\overline{B}^0$ decays. To determine these parameters the *sPlot* [91] method is used, with the $KKK\pi$ invariant mass as the discriminating variable. This method allows to separate signal and background. The invariant mass fit results discussed in Section 5.1.1 are used to assign a weight, W_e, to each candidate. Candidates that are likely to be background are assigned small or negative weights, whereas signal-like events are assigned larger weights. The *sPlot* technique is only valid if the discriminating variable is independent from all other observables. Table 5.6 shows the correlation coefficient between the $KKK\pi$ invariant mass ($m_{KKK\pi}$) and each of the fit variables ($\cos\theta_1, \cos\theta_1, \Phi, m_{K\pi}$ and m_{KK}) which is calculated[1] from Monte Carlo. Since the correlation is found to be small (less than 3.6 %), the background can be removed using the *sPlot* method.

Then, a maximum likelihood fit is performed where each candidate is weighted by W_e.

---

[1]The correlation between x and y distributions is defined as $\frac{\text{cov}(x,y)}{\sigma_x \sigma_y}$, where $\sigma_x (\sigma_y)$ is standard deviation of the $x(y)$ distribution.

Variable	Correlation with $m_{KKK\pi}$
$\cos\theta_1$	-0.004
$\cos\theta_2$	-0.001
Φ	0.004
$m_{K\pi}$	0.030
m_{KK}	0.036

Table 5.6: Correlation between $m_{KKK\pi}$ and the fit variables calculated from Monte Carlo.

The fit minimizes the negative log likelihood summed over selected candidates

$$-\ln\mathcal{L}(\vec{\lambda}) = -\alpha \sum_{e=1}^{N} W_e \ln \mathcal{S}(\vec{x}_e|\vec{\lambda}) \ , \tag{5.6}$$

where $\alpha = \sum_e W_e / \sum_e W_e^2$ is a normalization factor which ensures the correct determination of the statistical uncertainties for the weighted data sample. $\mathcal{S}(\vec{x}_e|\vec{\lambda})$ is the signal PDF, described in Section 3.1.3:

$$\mathcal{S}(\vec{x}_e|\vec{\lambda}) = \frac{h_i(\vec{\lambda})f_i(\vec{\Omega}_e)\mathcal{M}_i(\vec{m}_e)}{h_j(\vec{\lambda})\xi_j} \ . \tag{5.7}$$

In this PDF, the acceptance is present through the normalization weights ξ_j and the summation over i and j (independently) is assumed. Note that the fit is first performed to the $K^+K^-K^+\pi^-$ invariant mass with the total sample without separating events in categories. Then, data are separated in four categories, depending on the flavour of the B^0 meson identified by the charge of the pion and the TOS and TIS ("not-TOS", see Section 3.2.1) trigger category. The number of events in each subsample is shown in Table 5.7.

Subsample	Event
TOS; B^0	1219
TIS; B^0	1292
TOS; $\bar{B}^0$	1273
TIS; $\bar{B}^0$	1316
Total	5100

Table 5.7: Number of events in each subsample used in the angular-mass fit.

A simultaneous fit to the four subsamples using the model described in Section 3.1.3 is used to perform the angular-mass analysis. The separation into TOS and TIS ("not-TOS")

categories is mandatory as their acceptances are different. When the fit is completed, the physics parameters listed in Table 3.3 are available for B^0 and $\overline{B}^0$ decays. We deduce from them the polarization amplitudes and phases, CP asymmetries (described in Table 3.4) and triple-product asymmetries (described in Section 3.1.5). All the results are shown in Table 5.8. The first error on the fitted values is statistical and the second is the systematic error which will be studied in the next Section.

The value of longitudinal fraction f_L is around 0.5, indicating that the longitudinal and transverse polarizations have similar size. The $S\text{--}wave$ contributions are found 13.2% and 10.1% in the $K^+\pi^-$ and K^+K^- systems respectively. The CP asymmetries in both the amplitudes and the phases are consistent with zero.

Figure 5.12 shows the data distribution for the three helicity angles $\cos\theta_1$, $\cos\theta_2$ and ϕ and the two invariant masses $m_{K\pi}$ and m_{KK} with the projections of fit model superimposed.
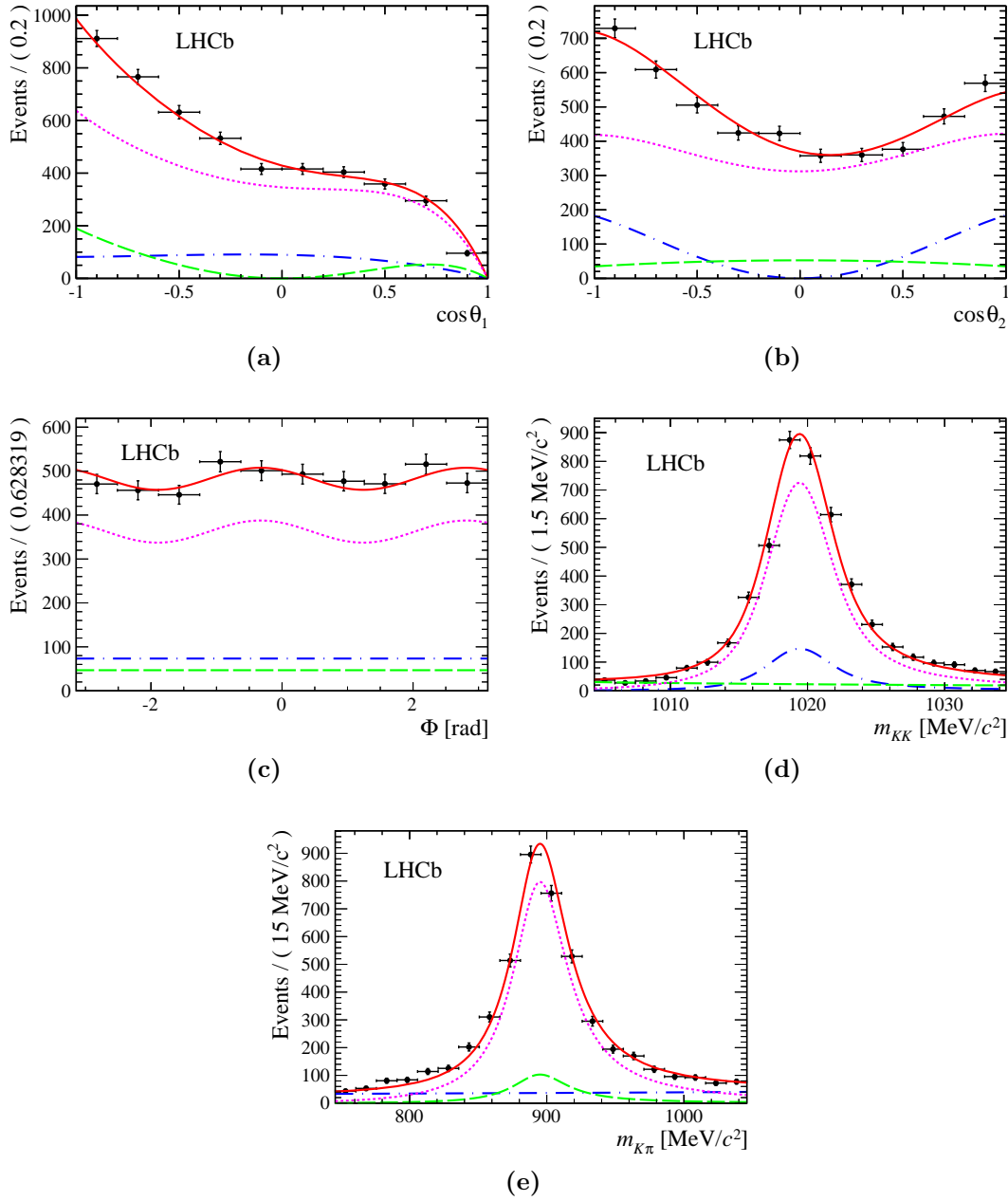
Figure 5.12: Data distribution (both B^0 and $\overline{B}^0$) and projections of the fit model on the three helicity angles (a) $\cos\theta_1$, (b) $\cos\theta_2$, (c) Φ, and the two resonance masses (d) m_{KK} and (e) $m_{K\pi}$. The background has been subtracted using the *sPlot* method described in the text. The magenta dashed lines represent the projections of the *P–wave* component while the dashed dotted blue and dashed green lines represent the $K\pi$ and KK *S–wave* components, respectively. The solid red line is the total fit.

Parameter	2012 data $\mathcal{L} = 2.0\,\mathrm{fb}^{-1}, \sqrt{s} = 8$ TeV
f_L	$0.499 \pm 0.011 \pm 0.010$
$f_\perp$	$0.223 \pm 0.009 \pm 0.008$
$f_\mathrm{S}(K\pi)$	$0.132 \pm 0.007 \pm 0.007$
$f_\mathrm{S}(KK)$	$0.101 \pm 0.007 \pm 0.007$
$\delta_\perp$ (rad)	$2.628 \pm 0.038 \pm 0.022$
$\delta_\parallel$ (rad)	$2.549 \pm 0.037 \pm 0.021$
$\delta_\mathrm{S}(K\pi)$ (rad)	$2.239 \pm 0.037 \pm 0.064$
$\delta_\mathrm{S}(KK)$ (rad)	$2.516 \pm 0.044 \pm 0.035$
$\mathcal{A}_0^{CP}$	$-0.012 \pm 0.022 \pm 0.006$
$\mathcal{A}_\perp^{CP}$	$-0.037 \pm 0.042 \pm 0.005$
$\mathcal{A}_\mathrm{S}(K\pi)^{CP}$	$0.105 \pm 0.053 \pm 0.018$
$\mathcal{A}_\mathrm{S}(KK)^{CP}$	$0.003 \pm 0.070 \pm 0.048$
$\delta_\perp^{CP}$ (rad)	$0.044 \pm 0.038 \pm 0.007$
$\delta_\parallel^{CP}$ (rad)	$0.029 \pm 0.037 \pm 0.013$
$\delta_\mathrm{S}(K\pi)^{CP}$ (rad)	$0.030 \pm 0.037 \pm 0.028$
$\delta_\mathrm{S}(KK)^{CP}$ (rad)	$0.076 \pm 0.044 \pm 0.017$
$\mathcal{A}_{T(true)}^1$	$0.0062 \pm 0.0071 \pm 0.0007$
$\mathcal{A}_{T(true)}^2$	$-0.0013 \pm 0.0052 \pm 0.0006$
$\mathcal{A}_{T(true)}^3$	$-0.0010 \pm 0.0030 \pm 0.0008$
$\mathcal{A}_{T(true)}^4$	$-0.0009 \pm 0.0026 \pm 0.0005$
$\mathcal{A}_{T(fake)}^1$	$-0.0494 \pm 0.0071 \pm 0.0015$
$\mathcal{A}_{T(fake)}^2$	$-0.0062 \pm 0.0052 \pm 0.0008$
$\mathcal{A}_{T(fake)}^3$	$-0.0165 \pm 0.0030 \pm 0.0018$
$\mathcal{A}_{T(fake)}^4$	$0.0038 \pm 0.0026 \pm 0.0007$

Table 5.8: Parameters measured in the angular mass fit of the decay $B^0 \to \phi K^*(892)^0$ with statistical and systematic uncertainties which will be detailed here after. The CP asymmetries (the eight middle entries) and the triple-product asymmetry (the last eight entries) are deduced from the fitted parameters (the first eight lines).

5.3 Sources of systematic uncertainties

In this section the main sources of systematic uncertainties on the physics parameters are studied; these are the acceptance correction, the $KKK\pi$ mass model, the difference in kinematic variables between data and simulation and the S–wave lineshape.

5.3.1 Statistical uncertainty on the acceptance correction

The acceptance correction has been studied in Section 3.2. In this method one just has to find the normalization weights numbers (ξ_j) using the simulated data. The Monte

Carlo statistics limits the precision of the normalization weights numbers. A systematic uncertainty must therefore be included to the final result due to the uncertainty on the acceptance correction.

To evaluate this systematic uncertainty, the acceptance function parametrisation in Section 3.2.2 is included in the generation of the toy Monte Carlo data. Two data samples are generated, one of 80000 events (approximately the size of the generated Monte Carlo data for TOS or TIS data sample) and one of 1 million events. The size of the large sample is chosen to be big enough compared to data to make the statistical uncertainties on the angular-mass variables negligible. These toy Monte Carlo samples contain both $K\pi$ and KK S–wave amplitudes are generated using the Foam generator [97] which is now fully integrated in the ROOT package.

The acceptance weights is then recalculated using the smaller sample of events. The results are used to fit the large sample (1 million) of events. This procedure is repeated 600 times and the large sample is kept unchanged. The difference between the fit result and the value used in the generation is filled for each parameter. The distributions of these differences are then fitted by a Gaussian function whose width is taken as the systematic uncertainty. The results of this study are shown in Table 5.9. Note that the CP parameters are fixed to zero for this study as we assume that the acceptance correction does not depend on the charge of particles in the final state.

Parameter	Systematic Error
f_{L}	0.0062
$f_\perp$	0.0064
$f_{\mathrm{S}}(K\pi)$	0.0058
$f_{\mathrm{S}}(KK)$	0.0052
$\delta_\perp$ (rad)	0.0173
$\delta_\parallel$ (rad)	0.0116
$\delta_{\mathrm{S}}(K\pi)$ (rad)	0.0309
$\delta_{\mathrm{S}}(KK)$ (rad)	0.0293

Table 5.9: Systematic uncertainties on the physics parameters due to the statistical uncertainty on the acceptance weights.

5.3.2 Dependence of the fitted parameters on the $m_{KKK\pi}$ mass model

A further uncertainty arises from the $K^+K^-K^+\pi^-$ mass model used to determine the signal weights for the angular analysis. In this study, the *sWeight* technique was used to separate the signal and background as described in Section 5.2 and is applied again with different signal and background parametrisations. We have considered the following cases:

- To test the signal model, a double Gaussian function is used to describe the signal shape instead of a Crystal Ball plus a wider Gaussian (see Section 5.1.1). The second Gaussian function of this new model has a width of 28.5 MeV/c^2 and accounts for a fraction of 0.88 compared to 26.5 MeV/c^2 and 0.857 for the wider Gaussian function in the Crystal Ball plus Gaussian model. These values were determined from the simulation. The result of the fit using a double Gaussian signal model is shown in Figure 5.13.

- To investigate the background model a first-order polynomial is chosen instead of the exponential function to describe the combinatorial background, the result is shown in Figure 5.14.

- A contribution from partially reconstructed B-decays (low mass background) is taken into account by using an ARGUS function. The yield and parameters of the ARGUS distribution are fixed based on the study of low mass background in Section 5.1.2. Figure 5.15 shows the fit result which includes a contribution from low mass background.

- Finally, an additional background model is considered with a possible contribution from the yet unobserved decays $\Lambda_b \to \phi p\pi^-$ and $\Lambda_b \to \phi pK^-$. For the first decay the proton is misidentified as a kaon, while for the second the proton is misidentified as a pion or the proton is misidentified as a kaon and a kaon is misidentified as a pion. This background is parametrized by using an ARGUS function with the end point m_{ARGUS} taken from previous study [8], all other parameters being left free. The result of the fit is shown in Figure 5.16.

Table 5.10 summarises the B^0 yield and the fitted parameters (such as the mean and width) of the B^0 signal peak. The new *sWeight* are then used in the fit of the polarization amplitudes and phases. The difference of these new fit results with respect to the nominal

one are shown in Table 5.11. The largest deviation result on each parameter is taken as
the systematic error for that parameter and is listed in the last column.
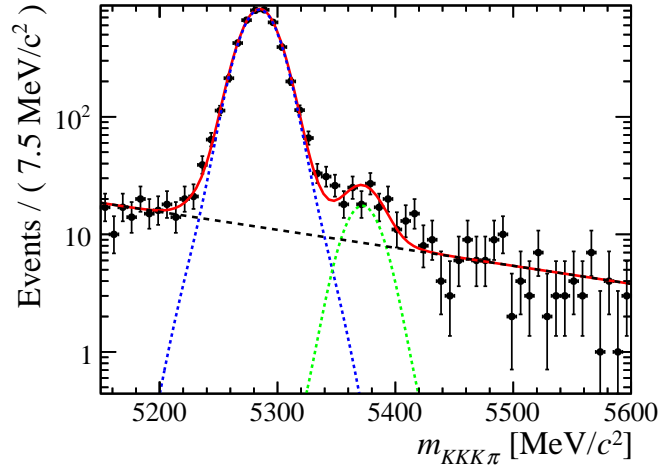
Figure 5.13: Invariant mass distribution of the selected $KKK\pi$ candidates. The distribution
is fitted by the model in which a double Gaussian function is used to model the signal (B^0 and
B_s^0 peaks correspond to blue dotted and green dotted lines); an exponential is used to model
the combinatorial background (black dashed line). The solid red line is the total fit.
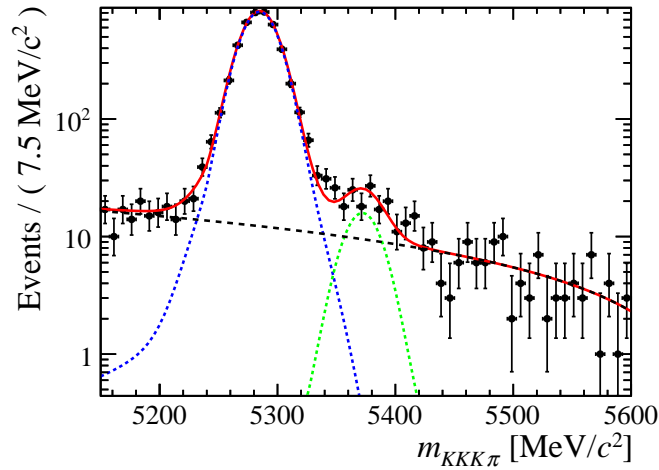
Figure 5.14: Invariant mass distribution of the selected $KKK\pi$ candidates. The total fit
(solid red line) is superimposed where a first order polynomial is used to model the background.
The B^0 and B_s^0 signals are shown in blue dotted and green dotted lines, respectively.
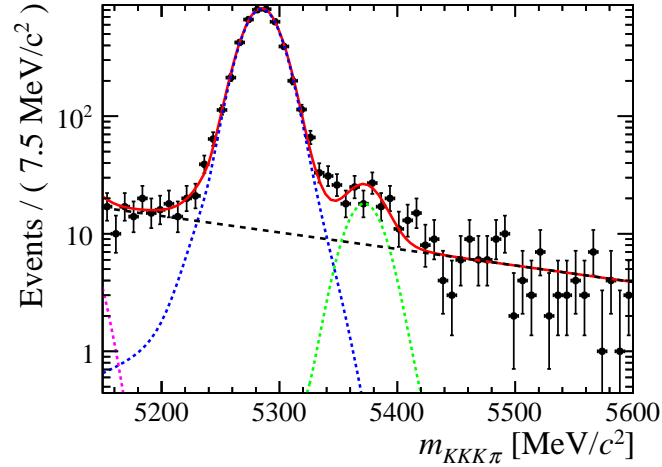
Figure 5.15: Invariant mass distribution of the selected $KKK\pi$ candidates. The total fit is shown in solid red line where a possible contribution from the low mass background is included (dotted magenta). The B^0 and B_s^0 signals are shown in blue dotted and green dotted lines, respectively and the background in black dashed line. The yield and parameters of the ARGUS are fixed based on the study of low mass background in Section 5.1.2.
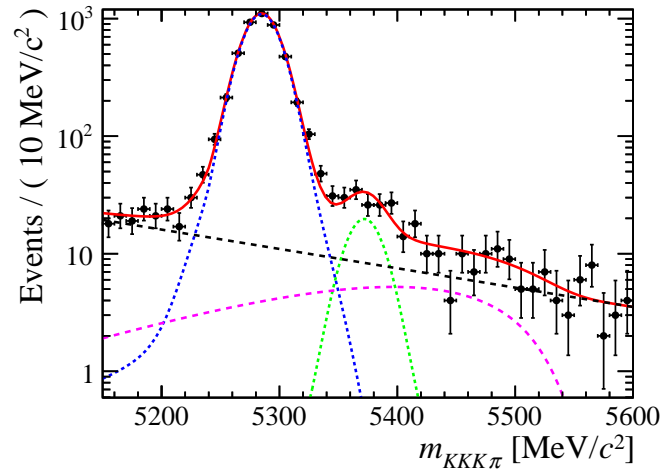
Figure 5.16: Invariant mass distribution of the selected $KKK\pi$ candidates. The total fit is shown in solid red line. A possible contributions form Λ_b decay is shown in dotted magenta line where the shape is described by an ARGUS function. The "power" and the "curvature" parameters of the ARGUS function are left free except for the end point m_{ARGUS} is taken from previous study Reference [8]. The B^0 and B_s^0 signals are shown in blue dotted and green dotted lines, respectively and the background in black dashed line.

Parameter	Nominal	Double Gaussian	Polynomial background	Argus	Λ_b background
m_{B^0} (MeV/c^2)	5284.8 ± 0.3	5284.8 ± 0.3	5284.8 ± 0.3	5284.8 ± 0.3	5284.8 ± 0.3
σ (MeV/c^2)	15.3 ± 0.3	15.5 ± 0.2	15.2 ± 0.3	15.3 ± 0.3	15.2 ± 0.3
N_{B^0}	4467 ± 69	4451 ± 69	4447 ± 70	4469 ± 69	4457 ± 69
$N_{B_s^0}$	98 ± 15	94 ± 15	86 ± 15	99 ± 15	81 ± 16
N_{Argus}	-	-	-	4	-
N_{Λ_b}	-	-	-	-	144 ± 49

Table 5.10: Table showing the fit results using different signal and background models. m_{B^0} is the fitted mean of the B^0 and σ is the width of the Crystal Ball function or the first Gaussian function in the double Gaussian model. $N_{B^0, B_s^0, \Lambda_b, Argus}$ are the yields for the B^0, B_s^0, Λ_b and low mass background components of the fit.

Parameter	Double Gaussian	Polynomial background	Argus	Λ_b background	Maximum
$f_{\rm L}$	0.00001	0.00017	0.00005	0.00008	0.0002
$f_\perp$	-0.00001	-0.00006	-0.00010	-0.00010	0.0001
$f_{\rm S}(K\pi)$	0.00000	-0.00001	0.00005	0.00005	0.0001
$f_{\rm S}(KK)$	-0.00000	-0.00005	-0.00001	-0.00002	0.0001
$\delta_\perp$ (rad)	0.00001	-0.00007	0.00002	0.00002	0.0001
$\delta_\parallel$ (rad)	-0.00000	-0.00002	-0.00006	-0.00006	0.0001
$\delta_{\rm S}(K\pi)$ (rad)	0.00000	0.00008	-0.00011	-0.00009	0.0001
$\delta_{\rm S}(KK)$ (rad)	-0.00000	0.00005	0.00007	0.00008	0.0001
$\mathcal{A}_0^{CP}$	-0.00002	-0.00028	-0.00021	-0.00026	0.0003
$\mathcal{A}_\perp^{CP}$	0.00001	0.00059	0.00011	0.00023	0.0006
$\mathcal{A}_{\rm S}(K\pi)^{CP}$	0.00001	0.00013	0.00011	0.00013	0.0001
$\mathcal{A}_{\rm S}(KK)^{CP}$	0.00000	-0.00004	0.00008	0.00005	0.0001
$\delta_\perp^{CP}$ (rad)	-0.00002	-0.00019	-0.00024	-0.00025	0.0003
$\delta_\parallel^{CP}$ (rad)	-0.00003	-0.00039	-0.00034	-0.00040	0.0004
$\delta_{\rm S}(K\pi)^{CP}$ (rad)	0.00000	0.00009	-0.00002	-0.00001	0.0001
$\delta_{\rm S}(KK)^{CP}$ (rad)	0.00001	-0.00016	0.00011	0.00008	0.0002
$\mathcal{A}_{T(true)}^1$	-0.000002	-0.000031	-0.000018	-0.000022	0.00003
$\mathcal{A}_{T(true)}^2$	-0.000001	-0.000019	-0.000009	-0.000014	0.00002
$\mathcal{A}_{T(true)}^3$	0.000001	0.000003	0.000005	0.000005	0.00001
$\mathcal{A}_{T(true)}^4$	-0.000001	0.000001	-0.000009	-0.000008	0.00001
$\mathcal{A}_{T(fake)}^1$	0.000002	-0.000008	0.000017	0.000016	0.00002
$\mathcal{A}_{T(fake)}^2$	-0.000001	0.000007	-0.000005	-0.000004	0.00001
$\mathcal{A}_{T(fake)}^3$	-0.000000	0.000007	-0.000004	-0.000003	0.00001
$\mathcal{A}_{T(fake)}^4$	0.000000	-0.000005	-0.000002	-0.000003	0.00001

Table 5.11: Table showing the difference between the nominal result and those using various signal and background models for a fit to the $KKK\pi$ invariant mass. The last column shows the maximal variation, which is then taken as the systematic uncertainty of the $KKK\pi$ mass model.

5.3.3   Difference in kinematic variables between data and simulation

A difference is observed in the kinematical distributions of the final-state particles between data and simulation as can be seen in Appendix C. This is due to the different values for the physics parameters[2] used in MC generation (P_{gen}) compared to their true values in data (P_{true}). In particular, the S–$wave$ is present in the data whereas it is not in the simulation. In order to have better agreement between data and MC, the simulated events are reweighted to match the signal distributions (or physics parameters) as expected from data (including the S-wave). In addition, the events are reweighted to match the observed distributions of the B^0 candidate and final-state particle momenta. To do this, an iterative procedure is applied as follows:

First, the nominal fit (described in Section 5.2) is performed using an initial estimate of the acceptance weights, which is obtained from the uncorrected MC sample using the method described in Section 3.2.1. Then we repeat this fit with the new acceptance weights obtained from the MC after reweighting to have the same B^0 transverse momentum as in the data. This yields a first estimate of the physics parameters, P_1. These parameters are then used to reweight each simulated event using the ratio of the PDF evaluated for P_1, divided by the PDF evaluated for P_{gen}. The final-state particle momentum spectra (K^+, K^-, K^+, π^-) of this "physics" reweighted sample is then further reweighted to have the same final state particle momentum as data. This MC sample, which has been reweighed twice: once for "physics" and once for the final-state particle momenta, is used to calculate new acceptance weights.

The new acceptance weights are then used in a second fit of the data to obtain a second estimate of the physics parameters, P_2. The MC sample is then reweighted again for physics and then for the final-state particle momenta. This process is iterative, the fits are performed with the new acceptance weights from each iteration in order to have better estimates $P_{2,3..i}$. The process ends when the convergence has been achieved (no further change to the acceptance weights). The procedure is summarised as follows:

1. Fit the data using the acceptance weights calculated from the nominal Monte Carlo.

2. Reweight the Monte Carlo to have the same B^0 transverse momentum as in the data.

3. Reweight the Monte Carlo to match "physics" parameters from the data.

---

[2]These "physics parameters" have been listed in Table 3.3.

4. Reweight the Monte Carlo to have the same final-state particle momenta as in the data.

5. Use this twice weighted Monte Carlo to recalculate the acceptance weights.

6. Use these new acceptance weights to fit the data.

7. Go back to step 3 and iterate until the fit result converges.

The reweighting is done for three helicity angles, the $K\pi$ mass distribution and the final-state momenta separately for TOS and not-TOS events due to the fact that the TOS and not-TOS data samples have different kinematic distributions. This also corrects for the difference in the ratio of TOS to not-TOS in data and Monte Carlo. Table 5.12 shows the acceptance weights for each step of the iterative procedure and Table 5.13 shows the fit results at each iteration.

The systematic uncertainty is taken as the difference between the nominal angular-mass fit using the unweighted acceptance weights and a fit using the weights calculated from the final iteration. The systematic uncertainty due to the discrepancy in kinematic variables in data and simulation is shown in Table 5.14.

TOS weight	Unweighted	$p_T(B)$	Iter. 1	Iter. 2	Iter. 3	Iter. 4
ξ_1	0.8917	0.8917	0.8631	0.8639	0.8641	0.8639
ξ_2	1.1287	1.1282	1.1066	1.1084	1.1083	1.1082
ξ_3	1.1436	1.1448	1.1159	1.1175	1.1186	1.1171
ξ_4	-0.0049	-0.0049	-0.0025	-0.0026	-0.0027	-0.0025
ξ_5	-0.0068	-0.0061	-0.0055	-0.0047	-0.0050	-0.0047
ξ_6	0.0159	0.0134	0.0150	0.0141	0.0151	0.0133
ξ_7	1.0681	1.0666	1.0470	1.0482	1.0490	1.0477
ξ_8	-0.1584	-0.1594	-0.1646	-0.1644	-0.1637	-0.1642
ξ_9	-0.0011	-0.0001	-0.0146	-0.0137	-0.0131	-0.0128
ξ_{10}	-0.0133	-0.0123	-0.0080	-0.0083	-0.0079	-0.0078
ξ_{11}	-0.0018	-0.0020	0.0006	0.0001	0.0006	0.0004
ξ_{12}	0.0240	0.0192	0.0224	0.0210	0.0229	0.0202
ξ_{13}	0.9252	0.9246	0.8822	0.8830	0.8832	0.8832
ξ_{14}	-0.0004	-0.0004	-0.0002	-0.0003	-0.0001	-0.0001
ξ_{15}	-0.0086	-0.0083	-0.0080	-0.0081	-0.0082	-0.0079
TIS weight	Unweighted	$p_T(B)$	Iter. 1	Iter. 2	Iter. 3	Iter. 4
ξ_1	0.8262	0.8261	0.7660	0.7675	0.7679	0.7679
ξ_2	1.2010	1.2021	1.1405	1.1443	1.1447	1.1447
ξ_3	1.2140	1.2133	1.1553	1.1593	1.1597	1.1598
ξ_4	0.0127	0.0153	0.0155	0.0156	0.0158	0.0157
ξ_5	-0.0105	-0.0106	0.0014	0.0027	0.0030	0.0032
ξ_6	-0.0110	-0.0109	-0.0093	-0.0092	-0.0094	-0.0093
ξ_7	1.0242	1.0252	0.9729	0.9769	0.9773	0.9780
ξ_8	-0.4155	-0.4106	-0.3786	-0.3784	-0.3784	-0.3783
ξ_9	0.0017	0.0019	0.0023	0.0025	0.0023	0.0022
ξ_{10}	-0.0040	-0.0032	-0.0063	-0.0066	-0.0068	-0.0069
ξ_{11}	0.0020	0.0012	-0.0023	-0.0025	-0.0024	-0.0026
ξ_{12}	0.0025	0.0030	0.0044	0.0047	0.0050	0.0052
ξ_{13}	0.8602	0.8627	0.7997	0.8006	0.8011	0.8008
ξ_{14}	0.0003	0.0003	0.0001	0.0002	0.0001	0.0000
ξ_{15}	0.0020	0.0015	0.0010	0.0009	0.0009	0.0009

Table 5.12: Table showing acceptance weights calculated at each iteration of the reweighting procedure described in the text.

Parameter	Nominal	$p_T(B^0)$	Iter. 1	Iter. 2	Iter. 3	Iter. 4
f_L	0.499	0.499	0.507	0.507	0.507	0.507
$f_\perp$	0.219	0.219	0.215	0.215	0.215	0.215
$f_S(K\pi)$	0.155	0.155	0.152	0.152	0.151	0.152
$f_S(KK)$	0.076	0.076	0.078	0.078	0.079	0.078
$\delta_\perp$ (rad)	2.620	2.621	2.629	2.631	2.631	2.631
$\delta_\parallel$ (rad)	2.521	2.521	2.535	2.537	2.537	2.537
$\delta_S(K\pi)$ (rad)	2.247	2.248	2.256	2.257	2.257	2.257
$\delta_S(KK)$ (rad)	2.498	2.499	2.491	2.491	2.491	2.491

Table 5.13: Table showing the fit results using the nominal acceptance weights and the new acceptance weights recalculated at each iteration. The fit converged after the fourth iteration.

Parameter	Systematic Error
f_L	0.0079
$f_\perp$	0.0045
$f_S(K\pi)$	0.0035
$f_S(KK)$	0.0026
$\delta_\perp$ (rad)	0.0104
$\delta_\parallel$ (rad)	0.0168
$\delta_S(K\pi)$ (rad)	0.0103
$\delta_S(KK)$ (rad)	0.0071
$\mathcal{A}_0^{CP}$	0.0015
$\mathcal{A}_\perp^{CP}$	0.0017
$\mathcal{A}_S(K\pi)^{CP}$	0.0008
$\mathcal{A}_S(KK)^{CP}$	0.0142
$\delta_\perp^{CP}$ (rad)	0.0063
$\delta_\parallel^{CP}$ (rad)	0.0126
$\delta_S(K\pi)^{CP}$ (rad)	0.0096
$\delta_S(KK)^{CP}$ (rad)	0.0103
$\mathcal{A}_{T(true)}^1$	0.0005
$\mathcal{A}_{T(true)}^2$	0.0006
$\mathcal{A}_{T(true)}^3$	0.0001
$\mathcal{A}_{T(true)}^4$	0.0004
$\mathcal{A}_{T(fake)}^1$	0.0011
$\mathcal{A}_{T(fake)}^2$	0.0008
$\mathcal{A}_{T(fake)}^3$	0.0004
$\mathcal{A}_{T(fake)}^4$	0.0004

Table 5.14: Table showing systematic uncertainties due to the discrepancy in kinematic distributions in data and simulation.

5.3.4   Influence of the S–wave lineshape on fitted parameters

We also consider the contributions of the *S–wave* models in both the KK and $K\pi$ system. The default fit uses the LASS parametrization to model the $K\pi$ *S–wave* (see Section 3.1.2). Both a pure phase-space model and a spin-0 relativistic Breit-Wigner with mean and width from the $K_0^*(1430)$ resonance are used to model the $K\pi$ *S–wave*. For the KK *S–wave*, a pure phase-space model is also used instead of the Flatté parametrization (see Section 3.1.2). The variation of the fit values with respect to the nominal fit is shown in Table 5.15, where the largest observed deviation, listed in the last column, is taken as a systematic uncertainty.

Parameter	BW(1430)	Phase space $K^+\pi^-$	Phase space K^+K^-	Maximum
f_{L}	0.00192	0.00040	−0.00038	0.0019
$f_\perp$	0.00007	0.00158	−0.00033	0.0016
$f_{\mathrm{S}}(K\pi)$	−0.00172	0.00125	0.00082	0.0017
$f_{\mathrm{S}}(KK)$	0.00101	0.00364	−0.00271	0.0036
$\delta_\perp$ (rad)	0.00037	−0.00757	−0.00328	0.0076
$\delta_\parallel$ (rad)	0.00063	−0.00633	−0.00536	0.0063
$\delta_{\mathrm{S}}(K\pi)$ (rad)	−0.01995	−0.05524	−0.00310	0.0552
$\delta_{\mathrm{S}}(KK)$ (rad)	−0.00468	0.01842	−0.00830	0.0184
$\mathcal{A}_0^{CP}$	0.00569	0.00518	−0.00222	0.0057
$\mathcal{A}_\perp^{CP}$	−0.00175	0.00421	−0.00048	0.0042
$\mathcal{A}_{\mathrm{S}}(K\pi)^{CP}$	−0.01792	−0.01682	0.00574	0.0179
$\mathcal{A}_{\mathrm{S}}(KK)^{CP}$	0.01440	0.04628	−0.00225	0.0463
$\delta_\perp^{CP}$ (rad)	0.00319	−0.00203	−0.00130	0.0032
$\delta_\parallel^{CP}$ (rad)	0.00207	−0.00303	−0.00420	0.0042
$\delta_{\mathrm{S}}(K\pi)^{CP}$ (rad)	−0.00201	−0.02683	0.00002	0.0268
$\delta_{\mathrm{S}}(KK)^{CP}$ (rad)	−0.00721	0.01375	0.00117	0.0137
$\mathcal{A}_{T(true)}^1$	0.00010	−0.00057	0.00002	0.00057
$\mathcal{A}_{T(true)}^2$	−0.00001	−0.00002	−0.00025	0.00025
$\mathcal{A}_{T(true)}^3$	−0.00002	−0.00080	−0.00001	0.00080
$\mathcal{A}_{T(true)}^4$	0.00027	−0.00034	−0.00005	0.00034
$\mathcal{A}_{T(fake)}^1$	−0.00017	−0.00100	−0.00018	0.00100
$\mathcal{A}_{T(fake)}^2$	0.00007	0.00009	−0.00017	0.00017
$\mathcal{A}_{T(fake)}^3$	−0.00060	−0.00179	−0.00002	0.00179
$\mathcal{A}_{T(fake)}^4$	0.00013	−0.00061	0.00009	0.00061

Table 5.15: Variation of the fit values with respect to the nominal fit when using different model of the $K^+\pi^-$ and K^+K^- *S–wave* as described in the text. The maximum of these variation is taken as the systematic error which is shown in the last column.

5.3.5   Summary of the systematic uncertainties

The systematic uncertainties on the measurement of the polarization amplitudes, on the relative strong phases and on the CP asymmetries and on the triple-product asymmetries as well are summarised in Table 5.16. The largest systematic uncertainties on the results of the angular analysis often arise from the understanding of the detector acceptance, labelled "Acceptance" in the table, which is assigned to account for the limited size of the Monte Carlo sample used. The column, labelled "Data/MC", shows the systematic uncertainty caused by the discrepancy between data and Monte Carlo sample. The uncertainty arising from the $K^+K^-K^+\pi^-$ mass model is shown in the column labelled "Mass model". The S–$wave$ lineshapes in both the $K^+\pi^-$ and K^+K^- system also contribute to an uncertainty on the measurement as shown in the column labelled "S-wave" in the table. Finally, the column labelled "Total" is the quadratic sum of the above individual contributions.

Measurement	Acceptance	Data/MC	Mass model	S-wave	Total
$f_{\rm L}$	0.0062	0.0079	0.0001	0.0019	0.010
$f_\perp$	0.0064	0.0045	0.0001	0.0016	0.008
$f_{\rm S}(K\pi)$	0.0058	0.0035	0.0001	0.0017	0.007
$f_{\rm S}(KK)$	0.0052	0.0026	0.0001	0.0036	0.007
$\delta_\perp$ (rad)	0.0173	0.0104	0.0001	0.0076	0.022
$\delta_\parallel$ (rad)	0.0116	0.0168	0.0001	0.0063	0.021
$\delta_{\rm S}(K\pi)$ (rad)	0.0309	0.0103	0.0002	0.0552	0.064
$\delta_{\rm S}(KK)$ (rad)	0.0293	0.0071	0.0001	0.0184	0.035
$\mathcal{A}_0^{CP}$	-	0.0015	0.0003	0.0057	0.006
$\mathcal{A}_\perp^{CP}$	-	0.0017	0.0005	0.0042	0.005
$\mathcal{A}_{\rm S}(K\pi)^{CP}$	-	0.0008	0.0002	0.0179	0.018
$\mathcal{A}_{\rm S}(KK)^{CP}$	-	0.0142	0.0002	0.0463	0.048
$\delta_\perp^{CP}$ (rad)	-	0.0063	0.0002	0.0032	0.007
$\delta_\parallel^{CP}$ (rad)	-	0.0126	0.0004	0.0042	0.013
$\delta_{\rm S}(K\pi)^{CP}$ (rad)	-	0.0096	0.0001	0.0268	0.028
$\delta_{\rm S}(KK)^{CP}$ (rad)	-	0.0103	0.0002	0.0137	0.017
$\mathcal{A}_{T(true)}^1$	-	0.00046	0.00002	0.00057	0.0007
$\mathcal{A}_{T(true)}^2$	-	0.00057	0.00002	0.00025	0.0006
$\mathcal{A}_{T(true)}^3$	-	0.00011	0.00001	0.00080	0.0008
$\mathcal{A}_{T(true)}^4$	-	0.00036	0.00001	0.00034	0.0005
$\mathcal{A}_{T(fake)}^1$	-	0.00109	0.00002	0.00100	0.0015
$\mathcal{A}_{T(fake)}^2$	-	0.00076	0.00001	0.00017	0.0008
$\mathcal{A}_{T(fake)}^3$	-	0.00037	0.00001	0.00179	0.0018
$\mathcal{A}_{T(fake)}^4$	-	0.00039	0.00000	0.00061	0.0007

Table 5.16: Systematic uncertainties on the measurement of the polarization amplitudes and relative strong phases and CP asymmetries. The column labelled "Total" is the quadratic sum of the individual contributions.

5.4 Fit validation

The PDF used in the angular-mass analysis is very complex and mistakes could be present. It is very important that the fitting procedure is verified. This section is devoted to this verification:

- first, a fit which includes the detector acceptance correction is performed on the fully simulated and selected Monte Carlo events to verified our procedure.

- second, the stability of the procedure is also checked with fit on magnet up/down samples as well as TOS/not-TOS, not-TIS/TIS samples.

So, should the results of the fits be different from the parameters introduced in the Monte Carlo (point 1), or be different from one sample to the other, this will indicate that our procedure is wrong or not stable.

The dataset used in this analysis is separated in TOS and not-TOS categories. The detector acceptance is calculated and corrected separately as discussed in Section 3.2.1. All events that overlaps between TOS and not-TOS categories are treated as TOS data sample. Therefore it is important to know the ratio of the number of overlapping events between TOS and not-TOS categories ($N_{\text{TOS\&TIS}}$) over the number of events in TOS category (N_{TOS}), $r = \frac{N_{\text{TOS\&TIS}}}{N_{\text{TOS}}}$. This ratio r is shown for simulation and data in Table 5.17 in which the number of events of data has been applied the *sPlot* technique. The fraction of events in TOS and TIS data sample are also shown. As the ratio r is the same for simulation and data, the effect caused by the difference of this ratio in simulation and data can be neglected.

	TOS (%)	TIS (%)	r (%)
Simulation	58.6	41.4	30.3
Data	48.7	51.3	31.8

Table 5.17: The fractions of TOS and TIS in simulation and data. The ratio r is defined in the text.

5.4.1 Fitting simulated data

A fit to fully simulated and selected events which are divided in TOS and TIS categories using the normalization weights from Table 3.5 is performed. As the simulation sample does not contain any *S–wave* amplitudes, these are fixed to zero in the fit. The fit results

are compared to the values which have been used in generation in Table 5.18. The results are in good agreement. Whereas no CP violation is introduced in the simulation, tiny non-zero CP asymmetries, consistent with zero, are observed as the result of acceptance correction.

Parameter	Generated value	Fitted value
f_{L}	0.521	0.520 ± 0.0013
$f_{\perp}$	0.251	0.248 ± 0.0011
$\delta_{\perp}$ (rad)	1.426	1.420 ± 0.0046
$\delta_{\parallel}$ (rad)	1.352	1.349 ± 0.0042
$\mathcal{A}_0^{CP}$		-0.003 ± 0.0025
$\mathcal{A}_{\perp}^{CP}$		0.002 ± 0.0046
$\delta_{\perp}^{CP}$ (rad)		-0.002 ± 0.0046
$\delta_{\parallel}^{CP}$ (rad)		-0.003 ± 0.0042
Event yield		151628

Table 5.18: Results from a fit to simulated events with detector acceptance effects correction (using normalization weights in Table 3.5) compared to values using in generation. A small non-zero CP violation appears that is due to the acceptance correction. The uncertainty is statistical only.

5.4.2   Fitting data in subdatasets

In order to test the stability of the fitting procedure, fits have been performed to data in subsamples such as TOS, not-TOS, magnet up and magnet down data samples. First, data is split into TOS and not-TOS samples, then two independent fits are performed to these subsamples. The results of the fits are compared in Table 5.19 with a good agreement within statistical uncertainty. This is also a good test of the detector acceptance corrections. Two other fits are performed separately to the subsamples selected with the magnet polarities up and down, respectively. The results are also good agreement within statistical uncertainty as shown in Table 5.20.

5.4.3   Fitting data split into not-TIS and TIS data samples

In this analysis, overlapping events between TOS and TIS trigger categories are treated as TOS data (formed TOS and not-TOS categories). An additional fit is performed by putting these events into the TIS data sample (formed not-TIS and TIS categories). The normalization weights are recalculated to correct the detector acceptance in not-TIS and

Parameter	TOS	TIS
f_{L}	0.518 ± 0.016	0.477 ± 0.015
$f_{\perp}$	0.216 ± 0.014	0.231 ± 0.013
$f_{\mathrm{S}}(K\pi)$	0.109 ± 0.009	0.151 ± 0.010
$f_{\mathrm{S}}(KK)$	0.097 ± 0.012	0.104 ± 0.010
$\delta_{\perp}$ (rad)	2.595 ± 0.057	2.679 ± 0.053
$\delta_{\parallel}$ (rad)	2.550 ± 0.059	2.564 ± 0.054
$\delta_{\mathrm{S}}(K\pi)$ (rad)	2.212 ± 0.069	2.282 ± 0.058
$\delta_{\mathrm{S}}(KK)$ (rad)	2.535 ± 0.069	2.485 ± 0.061
$\mathcal{A}_0^{CP}$	-0.045 ± 0.031	0.024 ± 0.032
$\mathcal{A}_{\perp}^{CP}$	-0.065 ± 0.064	-0.020 ± 0.058
$\mathcal{A}_{\mathrm{S}}(K\pi)^{CP}$	0.157 ± 0.080	0.064 ± 0.067
$\mathcal{A}_{\mathrm{S}}(KK)^{CP}$	-0.169 ± 0.132	0.143 ± 0.098
$\delta_{\perp}^{CP}$ (rad)	0.034 ± 0.057	0.029 ± 0.053
$\delta_{\parallel}^{CP}$ (rad)	0.067 ± 0.059	-0.025 ± 0.054
$\delta_{\mathrm{S}}(K\pi)^{CP}$ (rad)	0.098 ± 0.068	-0.040 ± 0.058
$\delta_{\mathrm{S}}(KK)^{CP}$ (rad)	0.144 ± 0.069	-0.013 ± 0.061

Table 5.19: Results from a fit to TOS data (left) and not-TOS data (right). The uncertainty is statistical only.

Parameter	Magnet up	Magnet down
f_{L}	0.507 ± 0.016	0.491 ± 0.015
$f_{\perp}$	0.226 ± 0.014	0.224 ± 0.013
$f_{\mathrm{S}}(K\pi)$	0.127 ± 0.011	0.136 ± 0.010
$f_{\mathrm{S}}(KK)$	0.094 ± 0.010	0.109 ± 0.010
$\delta_{\perp}$ (rad)	2.638 ± 0.054	2.632 ± 0.051
$\delta_{\parallel}$ (rad)	2.532 ± 0.057	2.565 ± 0.050
$\delta_{\mathrm{S}}(K\pi)$ (rad)	2.191 ± 0.053	2.282 ± 0.052
$\delta_{\mathrm{S}}(KK)$ (rad)	2.578 ± 0.066	2.452 ± 0.060
$\mathcal{A}_0^{CP}$	-0.015 ± 0.031	-0.013 ± 0.031
$\mathcal{A}_{\perp}^{CP}$	0.027 ± 0.061	-0.099 ± 0.059
$\mathcal{A}_{\mathrm{S}}(K\pi)^{CP}$	0.135 ± 0.084	0.091 ± 0.070
$\mathcal{A}_{\mathrm{S}}(KK)^{CP}$	0.116 ± 0.108	-0.091 ± 0.089
$\delta_{\perp}^{CP}$ (rad)	0.102 ± 0.054	-0.003 ± 0.051
$\delta_{\parallel}^{CP}$ (rad)	0.001 ± 0.057	0.054 ± 0.050
$\delta_{\mathrm{S}}(K\pi)^{CP}$ (rad)	0.097 ± 0.053	-0.030 ± 0.052
$\delta_{\mathrm{S}}(KK)^{CP}$ (rad)	0.139 ± 0.066	0.023 ± 0.060

Table 5.20: Results from a fit to magnet up data (left) and magnet down data (right). The uncertainty is statistical only.

TIS data samples as shown in Table 5.21. The fit results from not-TIS and TIS data samples as well as from TOS and not-TOS (main results of this analysis) are compared

in Table 5.22. It is good to see that the results are the same as the main results.

ξ_i	Flat Acc.	not-TIS weight	TIS weight
ξ_1	1	0.8986	0.8369
ξ_2	1	1.1395	1.1723
ξ_3	1	1.1318	1.1823
ξ_4	0	-0.0096	0.0104
ξ_5	0	-0.0039	-0.0110
ξ_6	0	0.0116	-0.0036
ξ_7	1	1.0139	1.0283
ξ_8	0	-0.1285	-0.3366
ξ_9	0	-0.0021	0.0033
ξ_{10}	0	0.0312	0.0001
ξ_{11}	1	0.9252	0.8772
ξ_{12}	0	-0.0189	-0.0020
ξ_{13}	0	-0.0041	0.0020
ξ_{14}	0	-0.0002	0.0001
ξ_{15}	0	-0.0070	-0.0012

Table 5.21: Table showing the normalization weights ξ_j described in the text for not-TIS and TIS datasets. Values in the second column correspond to the case flat acceptance.

Parameter	TOS/not-TOS (main result)	not-TIS/TIS
f_{L}	0.499 ± 0.011	0.498 ± 0.011
$f_{\perp}$	0.223 ± 0.009	0.224 ± 0.009
$f_{\mathrm{S}}(K\pi)$	0.132 ± 0.007	0.132 ± 0.007
$f_{\mathrm{S}}(KK)$	0.101 ± 0.007	0.100 ± 0.007
$\delta_{\perp}$ (rad)	2.628 ± 0.038	2.630 ± 0.038
$\delta_{\parallel}$ (rad)	2.549 ± 0.037	2.551 ± 0.037
$\delta_{\mathrm{S}}(K\pi)$ (rad)	2.239 ± 0.037	2.245 ± 0.037
$\delta_{\mathrm{S}}(KK)$ (rad)	2.516 ± 0.044	2.516 ± 0.044
$\mathcal{A}_0^{CP}$	-0.012 ± 0.022	-0.012 ± 0.022
$\mathcal{A}_{\perp}^{CP}$	-0.037 ± 0.042	-0.036 ± 0.042
$\mathcal{A}_{\mathrm{S}}(K\pi)^{CP}$	0.105 ± 0.053	0.105 ± 0.053
$\mathcal{A}_{\mathrm{S}}(KK)^{CP}$	0.003 ± 0.070	0.003 ± 0.070
$\delta_{\perp}^{CP}$ (rad)	0.044 ± 0.038	0.047 ± 0.038
$\delta_{\parallel}^{CP}$ (rad)	0.029 ± 0.037	0.030 ± 0.037
$\delta_{\mathrm{S}}(K\pi)^{CP}$ (rad)	0.030 ± 0.037	0.030 ± 0.037
$\delta_{\mathrm{S}}(KK)^{CP}$ (rad)	0.076 ± 0.044	0.077 ± 0.044

Table 5.22: Result from a fit to new dataset in which events overlap between TOS and TIS categories treated as TIS data sample and a recalculated normalization weights compared to the main results. The uncertainty is statistical only.

Chapter 6

Summary and conclusions

This thesis work has been devoted to the angular analysis of $B^0 \to \phi K^*(892)^0$ decays. The analysis used the pp collision data collected at a centre-of-mass energy of $\sqrt{s} = 8\,\text{TeV}$, corresponding to an integrated luminosity of 2.08 fb^{-1}, with the LHCb detector. An unbinned maximum likelihood fit is used in which the angular acceptance is corrected by using the normalization weights method. The acceptance corrections are done by finding the normalization numbers (ξ_j) using the MC simulation. The angular-mass analysis includes the contribution of $K^+\pi^-$ and K^+K^- *S–waves* and allows the polarization amplitudes, strong phase differences and *CP* asymmetries as well as triple-product asymmetries in the decay mode $B^0 \to \phi K^*(892)^0$ to be measured and deduced.

Table 6.1 shows a comparison of our results based on an integrated luminosity of 2.08 fb^{-1} (LHCb 2012) with the one of the previous measurements by LHCb (integrated luminosity of 1.0 fb^{-1}) (LHCb 2011) [8], and those of the BaBar [14] and Belle collaborations [7]. The comparisons here are only for the *P–wave* components: BaBar and Belle results did not take into account contribution of the interference between the K^+K^- *S–wave* and the *P–wave*. The LHCb 2011 measurement is the first to account both the $K^+\pi^-$ and K^+K^- *S–waves* and their interferences with the *P–wave*. The mass ranges of the $K^+\pi^-$ system used in the fits are also different. As the BaBar and Belle measurements include the contribution of *D–wave* (spin-2) from $B^0 \to \phi K_2^*(1430)$ decay, the $K^+\pi^-$ invariant mass range needed to be expanded up to 1.55 GeV/c^2. In contrast, the LHCb measurements do not consider the *D–wave* contribution, therefore the $K^+\pi^-$ mass is limited in a window of ± 150 MeV/c^2 around the nominal $K^*(892)^0$ mass.

Our results on *P–wave* components agree with the one of BaBar and Belle, but are much more precise. The measurements of the polarization amplitude differences show no evidence for *CP* violation.

Parameter	BaBar [14]	Belle [7]	LHCb (2011) [8]	LHCb (2012)
f_L	$0.494 \pm 0.034 \pm 0.013$	$0.499 \pm 0.030 \pm 0.018$	$0.497 \pm 0.019 \pm 0.015$	$0.499 \pm 0.011 \pm 0.010$
$f_\perp$	$0.212 \pm 0.032 \pm 0.013$	$0.238 \pm 0.026 \pm 0.008$	$0.221 \pm 0.016 \pm 0.013$	$0.223 \pm 0.009 \pm 0.008$
$\delta_\perp$	$2.35 \pm 0.13 \pm 0.09$	$2.37 \pm 0.10 \pm 0.04$	$2.633 \pm 0.062 \pm 0.037$	$2.628 \pm 0.038 \pm 0.022$
$\delta_\parallel$	$2.40 \pm 0.13 \pm 0.08$	$2.23 \pm 0.10 \pm 0.02$	$2.562 \pm 0.069 \pm 0.040$	$2.549 \pm 0.037 \pm 0.021$
A_0^{CP}	$+0.01 \pm 0.07 \pm 0.02$	$-0.030 \pm 0.061 \pm 0.007$	$-0.003 \pm 0.038 \pm 0.005$	$-0.012 \pm 0.022 \pm 0.006$
$A_\perp^{CP}$	$-0.04 \pm 0.15 \pm 0.06$	$-0.14 \pm 0.11 \pm 0.01$	$+0.047 \pm 0.072 \pm 0.009$	$-0.037 \pm 0.042 \pm 0.005$
$\delta_\perp^{CP}$	$+0.21 \pm 0.13 \pm 0.08$	$+0.05 \pm 0.10 \pm 0.02$	$+0.062 \pm 0.062 \pm 0.006$	$0.044 \pm 0.038 \pm 0.007$
$\delta_\parallel^{CP}$	$+0.22 \pm 0.12 \pm 0.08$	$-0.02 \pm 0.10 \pm 0.01$	$+0.045 \pm 0.068 \pm 0.015$	$0.029 \pm 0.037 \pm 0.013$

Table 6.1: Comparison of measurements made by the BaBar, Belle and LHCb experiments. The first uncertainty is statistical while the second is systematic.

The previous LHCb measurement is based on approximately 1655 signal candidates while the our measurement has approximately 4467 signal candidates. The improvements on the statistics both in the data and in the simulation lead to a decrease of the errors of about 50%. Our results, shown in Table 5.8, confirm the previous LHCb ones both concerning the polarization amplitudes, strong phases differences and CP asymmetries. The results also show a significant contribution from the two S–waves. The longitudinal polarization fraction f_L is about 0.5; this is consistent with previous measurements but does not agree with the naïve expectation of a dominant longitudinal polarization.

The triple-product (T-odd) asymmetries have also been derived from the results of the angular analysis. The results on the triple-product asymmetries are shown in Table 5.8 with true and fake asymmetries. $\mathcal{A}_T^1$, $\mathcal{A}_T^2$ are produced by the interference between the $A_\perp$ and A_0 or $A_\parallel$, whereas $\mathcal{A}_T^3$, $\mathcal{A}_T^4$ by the interference between the $A_\perp$ and $A_S^{K\pi}$ or A_S^{KK} which have not been measured in BaBar and Belle. The $\mathcal{A}_T^3$ and $\mathcal{A}_T^4$ have been studied for the first time in the LHCb 2011 measurement, however it should be noted that these triple-product asymmetries depend on the range of the $K^+\pi^-$ and K^+K^- invariant masses. The values of triple-product asymmetries used to compare are taken from older results of BaBar and Belle because the recent publications (BaBar 2008, Belle 2013) do not provide those triple-product asymmetries. There are differences between BaBar, Belle and LHCb results, as they have not fully considered the contribution of $K^+\pi^-$ and K^+K^- S–waves and their interferences into the analysis. Our results are consistent with the LHCb 2011 measurement. The measured true triple-product asymmetries are all close to zero and are consistent with CP conservation. Whereas, larger fake triple-product asymmetries are observed, implying the possible contribution of strong phases or the presence of significant final-state interactions.

In order to determine direct CP asymmetry, corrections are needed which are the detection asymmetry between $K^+\pi^-$ and $K^-\pi^+$ final-states and the asymmetry in production

Parameter	BaBar [14]	Belle [7]	LHCb (2011) [8]	LHCb (2012)
$\mathcal{A}^1_{T(true)}$	$0.11 \pm 0.05 \pm 0.01$	$0.16^{+0.16}_{-0.14} \pm 0.03$	$-0.007 \pm 0.012 \pm 0.002$	$0.0062 \pm 0.0071 \pm 0.0007$
$\mathcal{A}^2_{T(true)}$	$-0.02 \pm 0.04 \pm 0.01$	$0.01 \pm 0.10 \pm 0.02$	$0.004 \pm 0.014 \pm 0.002$	$-0.0013 \pm 0.0052 \pm 0.0006$
$\mathcal{A}^3_{T(true)}$	-	-	$0.004 \pm 0.006 \pm 0.001$	$-0.0010 \pm 0.0030 \pm 0.0008$
$\mathcal{A}^4_{T(true)}$	-	-	$0.002 \pm 0.006 \pm 0.001$	$-0.0009 \pm 0.0026 \pm 0.0005$
$\mathcal{A}^1_{T(fake)}$	-	$-0.41^{+0.16}_{-0.14} \pm 0.04$	$-0.105 \pm 0.012 \pm 0.006$	$-0.0494 \pm 0.0071 \pm 0.0015$
$\mathcal{A}^2_{T(fake)}$	-	$-0.06 \pm 0.10 \pm 0.01$	$-0.017 \pm 0.014 \pm 0.003$	$-0.0062 \pm 0.0052 \pm 0.0008$
$\mathcal{A}^3_{T(fake)}$	-	-	$-0.063 \pm 0.006 \pm 0.005$	$-0.0165 \pm 0.0030 \pm 0.0018$
$\mathcal{A}^4_{T(fake)}$	-	-	$-0.019 \pm 0.006 \pm 0.007$	$0.0038 \pm 0.0026 \pm 0.0007$

Table 6.2: Comparison of the triple-product asymmetries measurements made by the BaBar, Belle and LHCb experiments. The first uncertainty is statistical while the second is systematic.

rate between B^0 and $\overline{B}^0$ mesons. These corrections can be obtain by using the control channel decay $B^0 \to J/\psi K^{*0}$ in which CP violation is predicted to be zero. Unfortunately due to a lack of time, in this study the analysis of the control channel has not been done. Thus, only the raw asymmetry is obtained $A^{raw}_{CP} = 0.0162 \pm 0.0178$ (see Appendix D)

Future prospects

The analysis needs to be combined with the one presented in [8] in order to have a result with full dataset. The branching fraction also needs to be determined.

The statistical and systematic uncertainties on the result are almost equal as shown in Table 5.8. Therefore, any improvement on the statistics of the measured events, *e.g.* in RUN II (2015-2019), should be accompanied by an equivalent improvement in the simulation method and statistics. Most of the systematic uncertainties on the results are dominated by the detector acceptance correction. In this study, about 150,000 simulated events after passing the final selection have been used to study the detector acceptance correction. A larger simulation sample will reduce this source of systematic uncertainty. Other dominating systematic uncertainties arise from the difference in kinematic variables between data and simulation. The study on Section 5.3.3 shows that the discrepancy between the data and simulation samples has its origin in the imprecise values of the physics parameters introduced in the simulation and in the absence of any S–*wave* contribution. These are the two points which should be addressed in a new simulation of the $B^0 \to \phi K^{*0}$ decay channel.

In this study, the $K^+\pi^-$ invariant mass is limited in a window of ± 150 MeV/c^2. An experimental improvement could be to include the contributions of the higher order $K^+\pi^-$ resonances into the analysis: the mass region need then to be extended above $1 \, \text{GeV}/c^2$. As a result, the analysis will be more complicate because of the contributions

of the D–$wave$ $B^0 \to \phi K_2^*(1430)$ and S–$wave$ $B^0 \to \phi K_0^*(1430)$ and their interference. However, this could lead to an analysis which will be more complete.

Appendices

A The helicity formalism

$B^0 \to \phi K^{*0}$ is a pseudo-scalar to vector-vector decay. The B^0 being pseudo-scalar, the total angular momentum in the initial state is therefore $J = S_{B^0} = 0$. Let us call the daughter particles' spins by $S_1 = S_2 = 1$, the total spin in the final state S can therefore take the value 0, 1 or 2.

Invoking the isotropy of the B^0 decay implies that $S = L = 0$, leaving the following three combinations of spins $|S_1, S_2\rangle = |1, -1\rangle, \rangle = |0, 0\rangle$ and $\rangle = |-1, 1\rangle$.

The **helicity** λ is defined as the projection of the spin $\vec{S}$ onto the momentum direction $\hat{p}$

$$\lambda = \vec{S} \cdot \hat{p} \ \text{ with } \ \hat{p} = \frac{\vec{p}}{|\vec{p}|} \ . \tag{A.1}$$

The allowed spin combinations therefore correspond the helicities

$$(\lambda_\phi, \lambda_{K^{*0}}) = (+1, +1), \, (0, 0) \, \text{and} \, (-1, -1) \ . \tag{A.2}$$

The corresponding states are often written as $|f_+\rangle = |J, M, +1, +1\rangle$, $|f_0\rangle = |J, M, 0, 0\rangle$ and $|f_-\rangle = |J, M, -1, -1\rangle$, with in our case $J = M = 0$. Accordingly, the helicity amplitudes for the decay are labelled as: $H_\lambda = \langle f_\lambda|H_{eff}|\text{B}^0\rangle$, H_{eff} being the effective Hamiltonian with $\lambda = 0, +$ and $-$.

In a study of CP violation (or non-violation), we often want to identify CP eigenstates. It is therefore interesting to express the above states in terms of parity eigenstates. We define a transversity basis in which the states are eigenstates of the parity operator:
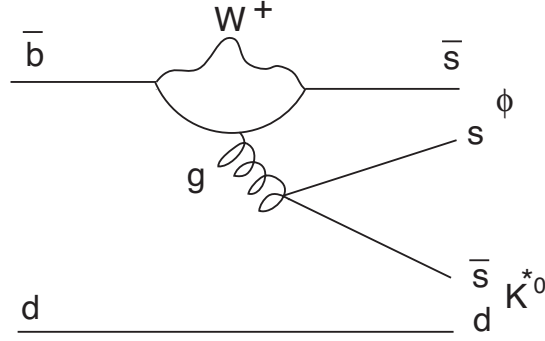
Figure A.1: Penguin diagram for the decay $B^0 \to \phi K^{*0}$.

$$P|f_+\rangle = |f_-\rangle \qquad\qquad |f_\parallel\rangle = \frac{|f_+\rangle + |f_-\rangle}{\sqrt{2}} \qquad\qquad P|f_\parallel\rangle = |f_\parallel\rangle$$

$$P|f_0\rangle = |f_0\rangle \qquad\qquad |f_0\rangle = |f_0\rangle \qquad\qquad P|f_0\rangle = |f_0\rangle$$

$$P|f_-\rangle = -|f_+\rangle \qquad\qquad |f_\perp\rangle = \frac{|f_+\rangle - |f_-\rangle}{\sqrt{2}} \qquad\qquad P|f_\perp\rangle = -|f_\perp\rangle$$

Parity operator on helicity basis vectors	Definition of the transversity basis	Parity operator on transversity basis

Similarly, the transversity amplitudes are defined as

$$A_0 = H_0 \quad A_\parallel = \frac{H_+ + H_-}{\sqrt{2}} \quad \text{and} \quad A_\perp = \frac{H_+ - H_-}{\sqrt{2}} \ . \tag{A.3}$$

The transversity basis allows to access directly to the CP violation quantities of interest.

Naive expectation of the relative importance of the amplitudes

In the Standard Model, the $\bar{s}$ quark from the loop in $B^0 \to \phi K^{*0}$ is produced in an helicity state of $+\frac{1}{2}$ (figure A.1). The upper s and $\bar{s}$ quarks now form a ϕ meson whose helicity can be $\lambda_\phi = 0$, 1 or -1; the value $\lambda_\phi = -1$ must be discarded as $\bar{s}$ helicity is already $+\frac{1}{2}$. Because helicity is conserved in strong interaction the s quark from the ϕ and the $\bar{s}$ quark from the K^{*0} must have opposite spin. In addition, angular momentum conservation the K^{*0} should has the same helicity as the ϕ in the decay of the B^0. These expectations can also be satisfied as weak decays of heavy quarks can undergo a spin flip, changing helicity form $\frac{1}{2}$ to $-\frac{1}{2}$ or vice-versa.

In this simple and naive analysis, we arrive at the conclusion that ϕ and K^{*0} both have helicities $\lambda = 0$. In other word, the $\bar{s}$ (s) quark from the ϕ has an helicity of $\lambda = +\frac{1}{2}$ $\left(-\frac{1}{2}\right)$

and the $\bar{s}$ (d) quark from the ϕ has a helicity of $\lambda = +\frac{1}{2}$ ($-\frac{1}{2}$). One can of course have helicity flips, but each flip would be suppressed by the ratio $\frac{m_V}{m_B}$ where m_V (m_B) is the mass of the vector (B^0) meson. We therefore expect $H_0 \gg H_+ \gg H_-$ (see Figure A.2).
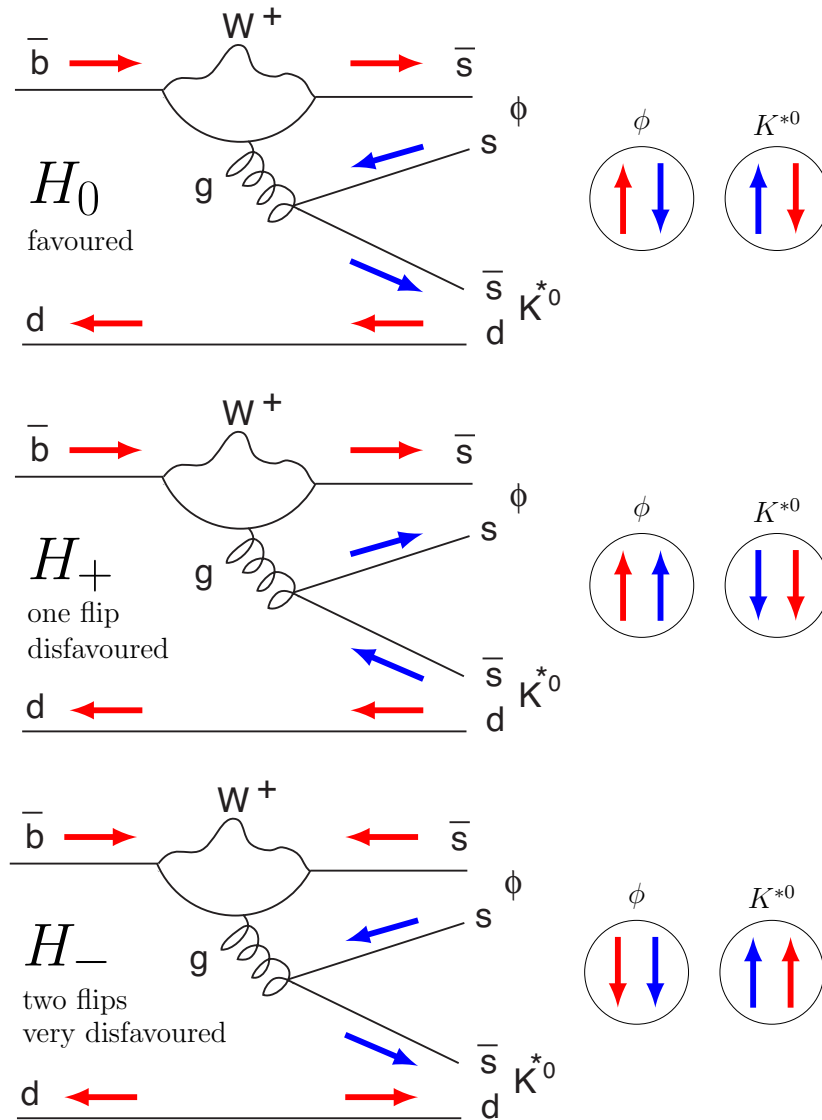
Figure A.2: Helicity amplitudes for the decay $B^0 \to \phi K^{*0}$. The arrows on the quark lines represent their spins. The red present for b and d quarks, while the blue for s and $\bar{s}$ quarks from the gluon.

B   The resolution on K^+K^- invariant mass system

The reconstructed mass of the ϕ and K^{*0} mesons are affected by the detector resolution effects on momentum and energy measurements. Since the K^{*0} meson width is very large $(48\,\mathrm{MeV}/c^2)$ compared to the experimental mass resolution, the resolution effect on the measured $m_{K\pi}$ distribution can be ignored. This is not the case for the ϕ mass.

To take into account the experimental mass resolution on the KK system, a Breit-Wigner function convolved with a Gaussian function is used to fit the m_{KK} distribution. The width of the Breit-Wigner is fixed to the World average value of the ϕ meson $(4.26\,\mathrm{MeV}/c^2)$ [27] and the width of the Gaussian is left free. The fitted width of the Gaussian distribution is then taken as the experimental mass resolution on m_{KK}. Figure B.3 shows the result of the m_{KK} distribution with fully selected simulation data (MC 2012) fitted by a Breit-Wigner convolved with a Gaussian function. The experimental mass resolution was measured to be $1.23 \pm 0.015\,\mathrm{MeV}/c^2$.
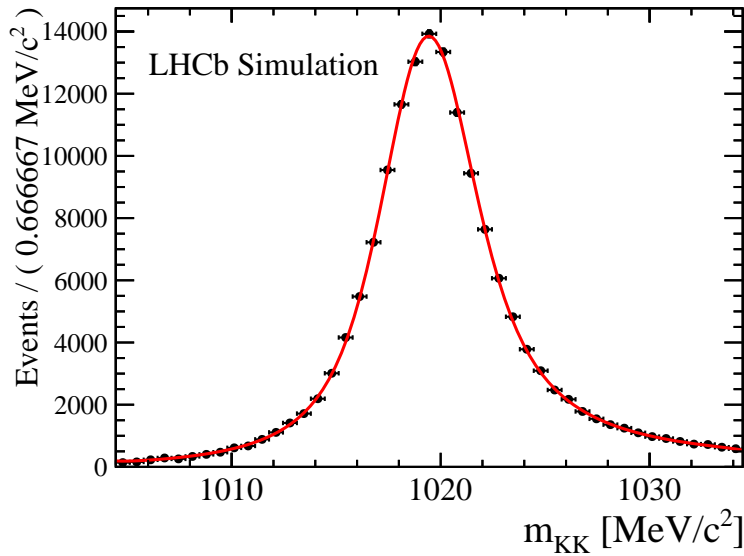
Figure B.3: Fit a relativistic Breit-Wigner convolved with a Gaussian to invariant mass K^+K^- distribution using the simulation data (MC 2012).

C Comparisons of kinematic variables between data and simulation

The difference between the data and the simulation, which has been studied in Section 5.3.3, is treated as a source of systematic uncertainty. Due to the fact that the background is present in the data but not in the simulated events, the *sPlot* [91] technique is used to unfold the background distributions for the momentum, transverse momentum of the pion and kaon and the reconstructed B^0 meson in each event. To ensure that the differences in the distributions are not due to a large difference in the ratio of TOS to not-TOS between data and simulation, the simulation has been weighted to have the same ratio of TOS to not-TOS events as the signal data. The reweighting described in Section 5.3.3 is then done. The comparisons of those kinematic variables are shown in Figures C.4 - C.7 for before and after the reweighting (see Section 5.3.3). We can see that after reweighting procedure the difference between data and Monte Carlo is reduced, particularly in the low momentum region.
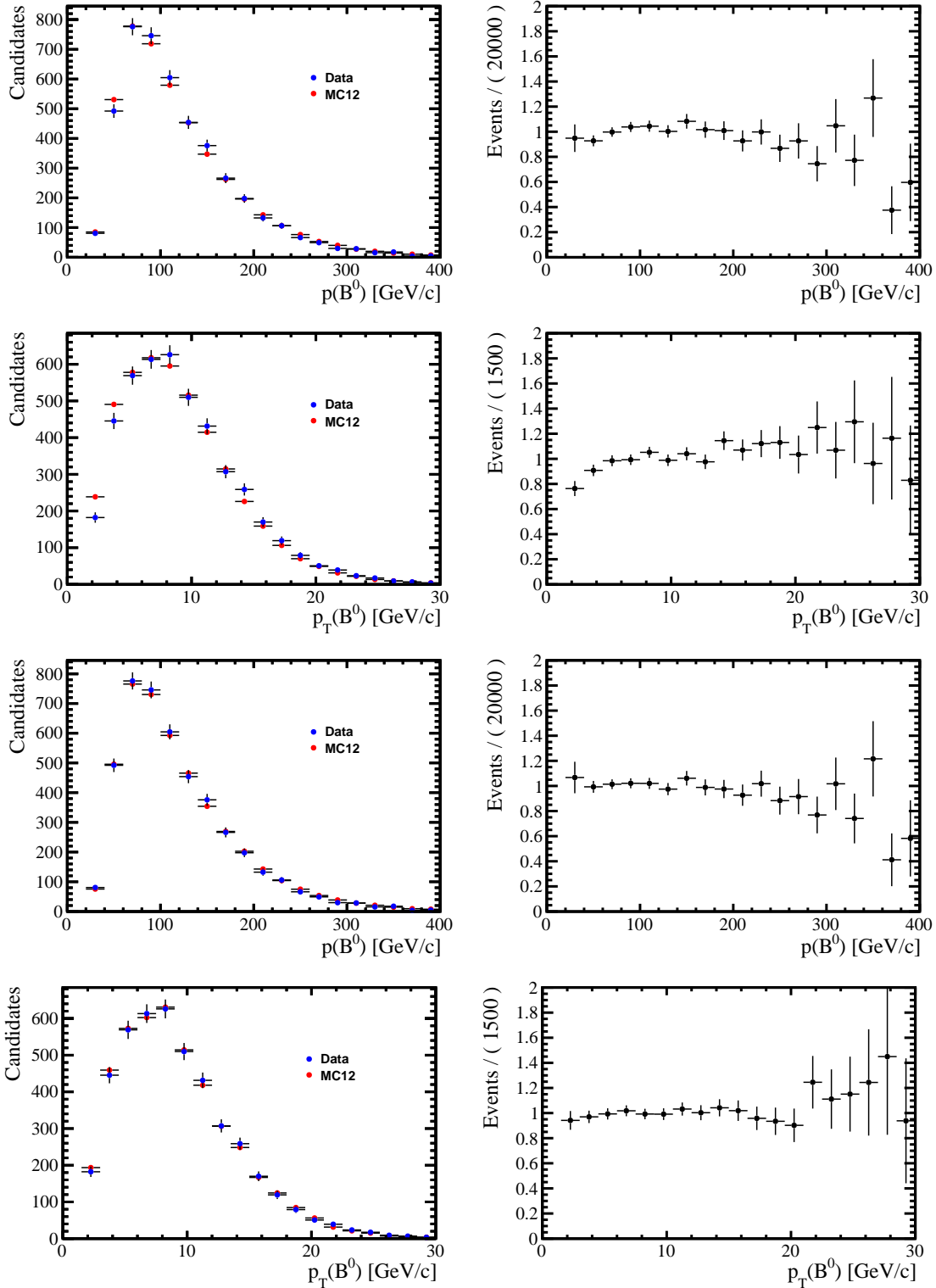
Figure C.4: Comparison of the B^0 momentum and transverse momentum distribution obtained from the data (blue) with the simulation (red) before (two rows above) and after (two rows below) the reweighting procedure described in Section 5.3.3. Note that the background in data has been removed using the *sPlot* technique and that the MC histogram is normalized to the number of events seen in the data. The right column distributions give the ratio of data over Monte Carlo as a function of the B^0 momentum.
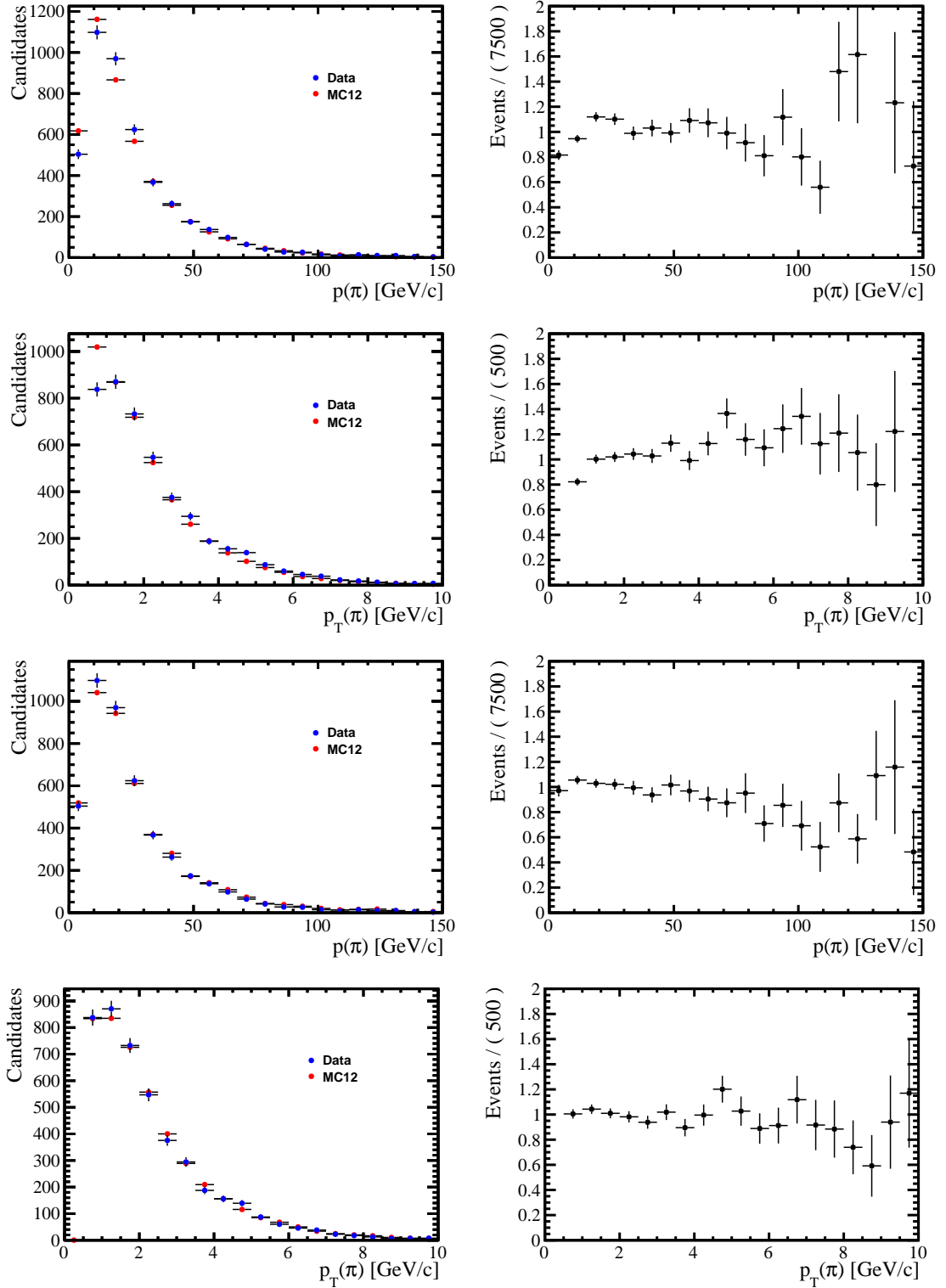
Figure C.5: Comparison of the pion momentum and transverse momentum distribution obtained from the data (blue) with the simulation (red) before (two rows above) and after (two rows below) the reweighting procedure described in Section 5.3.3. Note that the background in data has been removed using the *sPlot* technique and that the MC histogram is normalized to the number of events seen in the data. The right column distributions give the ratio of data over Monte Carlo as a function of the B^0 momentum.
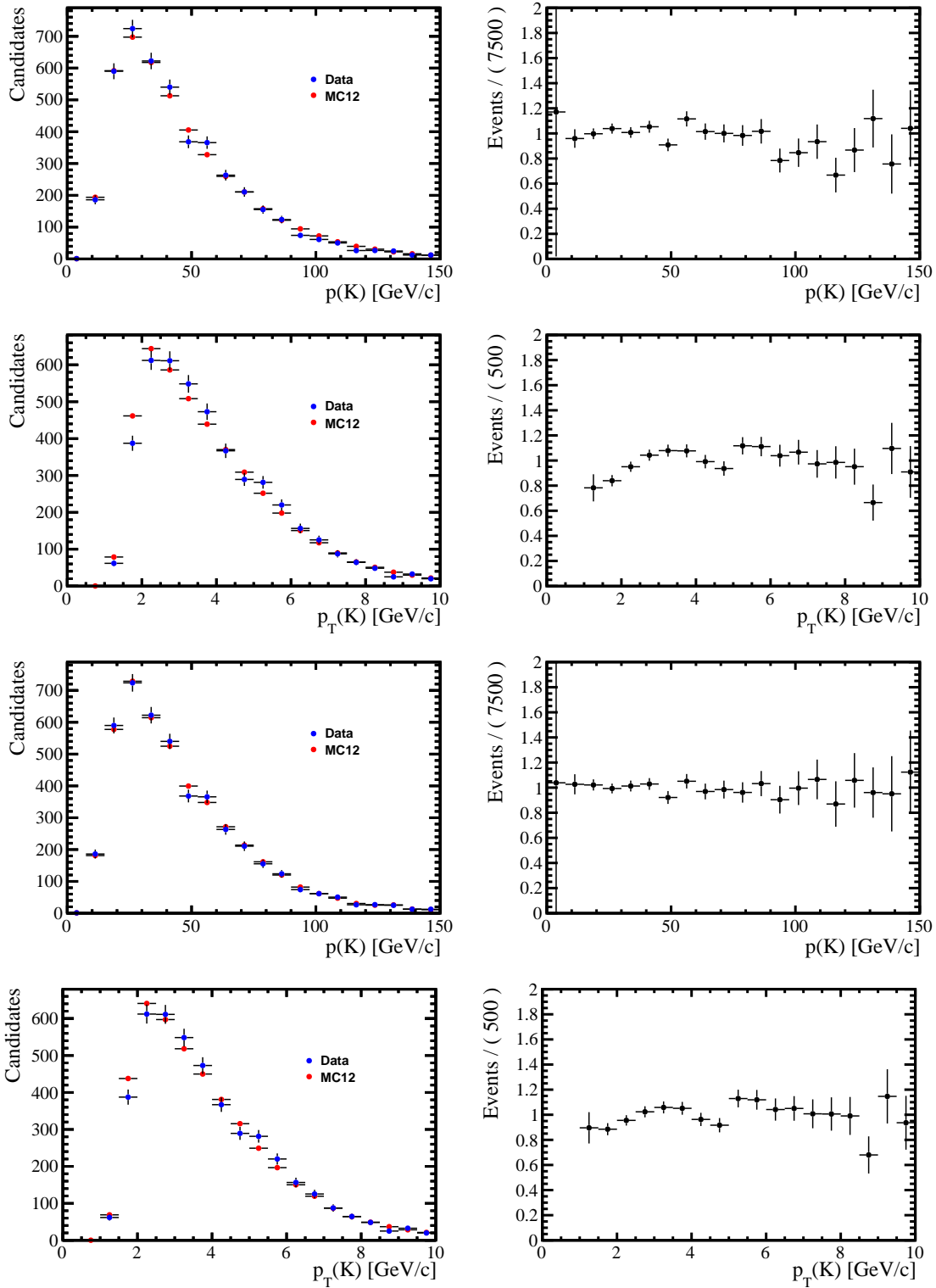
Figure C.6: Comparison of the maximum kaon momentum and transverse momentum distribution obtained from the data (blue) with the simulation (red) before (two rows above) and after (two rows below) the reweighting procedure described in Section 5.3.3. Note that the background in data has been removed using the *sPlot* technique and that the MC histogram is normalized to the number of events seen in the data. The right column distributions give the ratio of data over Monte Carlo as a function of the B^0 momentum.
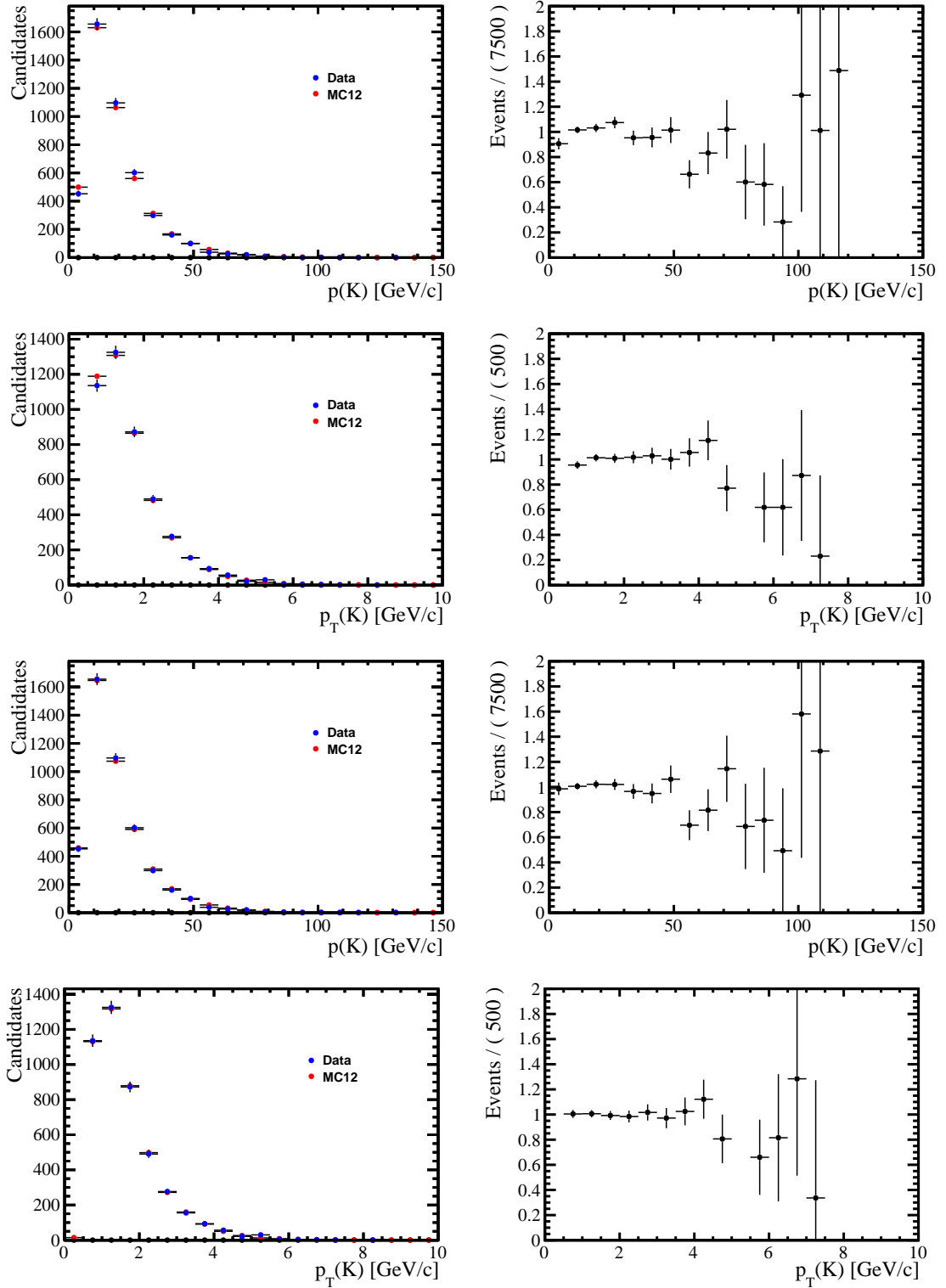
Figure C.7: Comparison of the minimum kaon momentum and transverse momentum distribution obtained from the data (blue) with the simulation (red) before (two rows above) and after (two rows below) the reweighting procedure described in Section 5.3.3. Note that the background in data has been removed using the *sPlot* technique and that the MC histogram is normalized to the number of events seen in the data. The right column distributions give the ratio of data over Monte Carlo as a function of the B^0 momentum.

D   Determination of the raw direct CP asymmetry

The raw measurement of the direct CP asymmetry in the $B^0 \to \phi K^{*0}$ decay is obtained from

$$A_{raw} = \frac{N_{\bar{B}} - N_B}{N_{\bar{B}} + N_B} \ , \tag{D.4}$$

where N_B and $N_{\bar{B}}$ are the numbers of events which are determined from fit to the $m_{KKK\pi}$ invariant mass distributions and performed separately for $B^0 \to \phi K^{*0}$ and $\bar{B}^0 \to \phi \bar{K}^{*0}$ decays. The N_B and $N_{\bar{B}}$ obtained from the fit include the numbers of $K\pi$ and KK S–wave events. Hence, the dilution from the S–wave components needs to be corrected using the results of the angular analysis. Formula D.4 becomes

$$A_{raw} = \frac{N_{\bar{B}} \times (1 - |A_{S,\bar{B}}^{K\pi}|^2 - |A_{S,\bar{B}}^{KK}|^2) - N_B \times (1 - |A_{S,B}^{K\pi}|^2 - |A_{S,B}^{KK}|^2)}{N_{\bar{B}} \times (1 - |A_{S,\bar{B}}^{K\pi}|^2 - |A_{S,\bar{B}}^{KK}|^2) + N_B \times (1 - |A_{S,B}^{K\pi}|^2 - |A_{S,B}^{KK}|^2)} \ . \tag{D.5}$$

Since the detector response depends on the trigger line, the candidates are separated into the TOS and TIS trigger categories. The events that fall in both the two categories (17%) are assigned as TOS. For each category, the data is separated in B^0 and $\bar{B}^0$ by using the charge of the pion. Finally, a simultaneous fit is performed to both data categories with the model is described in Section 5.1. Figure D.8 shows data distribution (for both B^0 and $\bar{B}^0$) and the projection of the fit on the TOS and TIS samples. The numbers of events obtained from the fit are given in Table D.1.

	TOS		TIS	
Number of Event	B^0	$\bar{B}^0$	B^0	$\bar{B}^0$
N_{B^0}	1086 ± 34	1103 ± 34	1155 ± 35	1127 ± 35
$N_{B_s^0}$	22 ± 7	35 ± 8	20 ± 7	23 ± 7
N_{bkg}	112 ± 15	135 ± 16	127 ± 16	157 ± 17

Table D.1: Table showing the results of the simultaneous fit using the model is described in Section 5.1 to the data separated in the trigger types and B meson flavors.

Using the N_B, $N_{\bar{B}}$ from Table D.1 and the values of S–wave amplitudes from the nominal fit result (Table 5.8), we obtain the raw asymmetries for the two trigger types as

$$A_{raw}^{\text{TOS}} = 0.0265 \pm 0.0253 \ ,$$
$$A_{raw}^{\text{TIS}} = 0.0061 \pm 0.0250 \ . \tag{D.6}$$

The final value for the raw CP asymmetry is achieved after averaging the two trigger categories by using

$$A_{CP} = \frac{A_{CP}^{\mathrm{TOS}}/\sigma^2(A_{CP}^{\mathrm{TOS}}) + A_{CP}^{\mathrm{TIS}}/\sigma^2(A_{CP}^{\mathrm{TIS}})}{1/\sigma^2(A_{CP}^{\mathrm{TOS}}) + 1/\sigma^2(A_{CP}^{\mathrm{TIS}})} \ , \tag{D.7}$$

$$\sigma(A_{CP}) = \left[\frac{1}{\sigma^2(A_{CP}^{\mathrm{TOS}})} + \frac{1}{\sigma^2(A_{CP}^{\mathrm{TIS}})} \right]^{-\frac{1}{2}} \ , \tag{D.8}$$

where $\sigma(A_{CP}^{\mathrm{TOS}})$ and $\sigma(A_{CP}^{\mathrm{TIS}})$ are the statistical errors of the A_{CP} for the TOS and TIS trigger categories. We obtain

$$A_{CP}^{raw} = 0.0162 \pm 0.0178 \ . \tag{D.9}$$
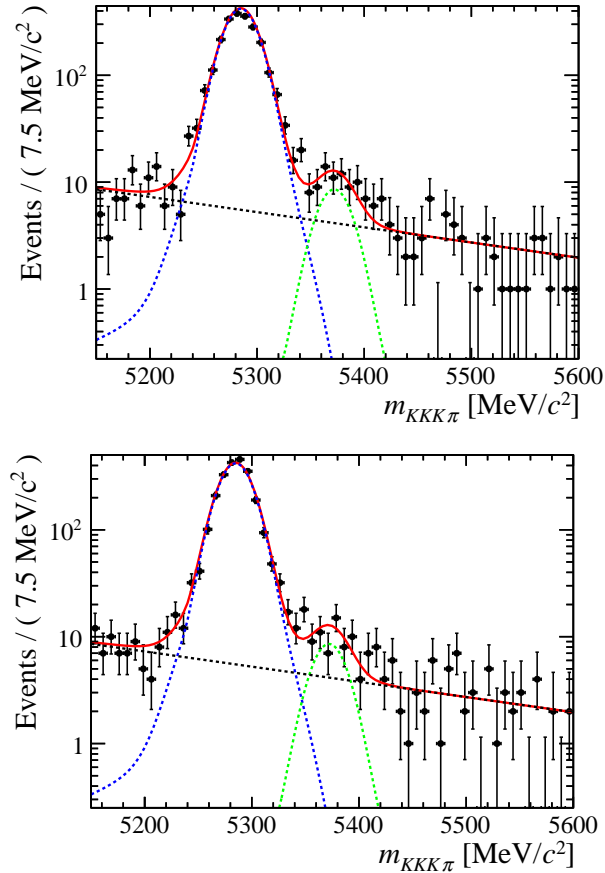
Figure D.8: Data distributions (for both B^0 and $\overline{B}^0$) and the projection of the fit model on the TOS (top) and TIS (bottom) samples used to obtain the raw asymmetries A_{raw}^{TOS} and A_{raw}^{TIS}.

Bibliography

[1] CLEO collaboration, R. A. Briere *et al.*, *Observation of $B \to \phi K$ and $B \to \phi K^*$*, Phys. Rev. Lett. **86** (2001) 3718, `arXiv:0101032`.

[2] BaBar collaboration, B. Aubert *et al.*, *Measurement of the decay $B \to \phi K$ and $B \to \phi K^*$*, Phys. Rev. Lett. **87** (2001) 151801.

[3] BaBar collaboration, B. Aubert *et al.*, *Measurement of the $B^0 \to \phi K^{*0}$ decay amplitudes*, Phys. Rev. Lett. **93** (2004) 231804, `arXiv:0408017`.

[4] BaBar collaboration, B. Aubert *et al.*, *Vector-tensor and vector-vector decay amplitude analysis of $B^0 \to \phi K^{*0}$*, Phys. Rev. Lett. **98** (2007) 051801, `arXiv:0610073`.

[5] Belle collaboration, K.-F. Chen *et al.*, *Measurement of branching fractions and polarization in $B \to \phi K^{(*)}$ decays*, Phys. Rev. Lett. **91** (2003) 201801.

[6] Belle collaboration, K.-F. Chen *et al.*, *Measurement of polarization and triple product correlations in $B^0 \to \phi K^{*0}$ decays*, Phys. Rev. Lett. **94** (2005) 221801.

[7] Belle collaboration, M. Prim *et al.*, *Angular analysis of $B^0 \to \phi K^*$ decays and search for CP violation at Belle*, Phys. Rev. **D88** (2013) 072004, `arXiv:1308.1830`.

[8] LHCb Collaboration, R. Aaij *et al.*, *Measurement of polarization amplitudes and CP asymmetries in $B^0 \to \phi K^*(892)^0$*, JHEP **05** (2014) 069, `arXiv:1403.2888`.

[9] Particle Data Group, K. Olive *et al.*, *The Review of Particle Physics*, Chin. Phys. **C38** (2014) 090001.

[10] Belle collaboration, A. Somov *et al.*, *Measurement of the Branching Fraction, Polarization, and CP Asymmetry for $B^0 \to \rho^+ \rho^-$ Decays, and Determination of the Cabibbo-Kobayashi-Maskawa Phase ϕ_2*, Phys. Rev. Lett. **96** (2006) 171801.

[11] BaBar collaboration, B. Aubert *et al.*, *Study of $B^0 \to \rho^+ \rho^-$ decays and constraints on the CKM angle α*, Phys. Rev. **D76** (2007) 052007.

[12] BaBar collaboration, B. Aubert *et al.*, *Measurement of the Branching Fraction, Polarization, and CP Asymmetries in $B^0 \to \rho^0 \rho^0$ Decay, and Implications for the CKM Angle α*, Phys. Rev. **D78** (2008) 071104.

[13] Belle Collaboration, I. Adchi *et al.*, *Study of $B^0 \to \rho^0 \rho^0$ decays, implications for the CKM angle ϕ_2 and search for other B^0 decay modes with a four-pion final state*, Phys. Rev. **D89** (2014) 072008, `arXiv:1212.4015`.

[14] BaBar collaboration, B. Aubert *et al.*, *Time-dependent and time-integrated angular analysis of the $B \to \phi K_S^0 \pi^0$ and $\phi K^\pm \pi^\mp$* , Phys. Rev. **D78** (2008) 092008, `arXiv:0808.3586`.

[15] A. Kagan, *Polarization in $B \to VV$ Decays*, Phys. Lett. **B601** (2004) 151.

[16] P. Colangelo, F. Fazio, and T. Pham, *The riddle of polarization in $B \to VV$ transitions*, Phys. Lett. **B597** (2004) 291.

[17] M. Beneke, J. Rohrer, and D. Yang, , Nucl. Phys. **B774** (2007) 64.

[18] H. Cheng and K. Yang, , Phys. Rev. **D78** (2008) 094001.

[19] Heavy Flavor Averaging Group, Y. Amhis *et al.*, *Averages of b-hadron, c-hadron, and tau-lepton properties as of summer 2014*, `arXiv:1412.7515`, online update at http://www.slac.stanford.edu/xorg/hfag.

[20] A. Datta and D. London, *Triple-Product Correlations in $B \to V_1 V_2$ Decays and New Physics*, Int. J. Mod. Phys. **A19** (2004) 2505, `arXiv:0303159v3`.

[21] M. Gronau and J. L. Rosner, *Triple product asymmetries in K, $D_{(s)}$ and $B_{(s)}$ decays*, Phys. Rev. **D84** (2011) 096013, `arXiv:1107.1232`.

[22] ATLAS Collaboration, G. Aad *et al.*, *Observation of a new particle in the search for the Standard Model Higgs boson with the ATLAS detector at the LHC*, Phys. Lett. **B716** (2012) 1, `arXiv:1207.7214`.

[23] CMS Collaboration, S. Chatrchyan *et al.*, *Observation of a new boson at a mass of 125 GeV with the CMS experiment at the LHC*, Phys. Lett. **B716** (2012) 30, `arXiv:1207.7235`.

[24] D. J. Richman, *Heavvy-quark Physics and CP Violation*, 1997. Les Houches summer school lectures.

[25] M. Kobayashi and K. Maskawa, *CP-Violation in the Renormalizahle Theory of Weak Interaction*, Prog. Theor. Phys. **49** (1973) 652.

[26] N. Cabibbo, *Unitary Symmetry and Leptonic Decays*, Phys. Rev. Lett. **10** (1963) 531.

[27] Particle Data Group, J. Beringer *et al.*, *The Review of Particle Physics*, Phys. Rev. **D86** (2012) 010001.

[28] L. Wolfenstein, *Parametrization of the Kobayashi-Maskawa Matrix*, Phys. Rev. Lett. **51** (1983) 1945.

[29] CKMfitter group, J. Charles *et al.*, , Eur. Phys. J. **C41** (2005) 1, updated Summer 2015; http://ckmfitter.in2p3.fr.

[30] P. Kooijman and N. Tuning, *CP Violation*, Lectures 2012.

[31] Y. Nir, *CP violation in meson decays*, arXiv:0510413v1.

[32] LHCb collaboration, R. Aaij *et al.*, *First observation of CP violation in the decays of B_s^0 mesons*, Phys. Rev. Lett. **110** (2013) 221601, arXiv:1304.6173.

[33] Particle Data Group, K. Olive *et al.*, $B^0 - \overline{B}^0$ *Mixing*, Chin. Phys. **C38** (2014) 090001.

[34] LHCb Collaboration, R. Aaij *et al.*, *Measurement of CP violation in $B^0 \rightarrow J/\psi K_{\mathrm{s}}^0$ decays*, Phys. Rev. Lett. **115** (2015) 031601, arXiv:1503.0708.

[35] LHCb Collaboration, R. Aaij *et al.*, *Precision measurement of CP violation in $B_s^0 \rightarrow J/\psi K^+ K^-$ decays*, Phys. Rev. Lett. **114** (2015) 041801, arXiv:1411.3104.

[36] L. Evans and P. Bryant, *LHC Machine*, J. Instrum. **3** (2008) S08001.

[37] ATLAS collaboration, G. Aad *et al.*, *The ATLAS Experiment at the CERN Large Hadron Collider*, J. Instrum. **3** (2008) S08003.

[38] CMS collaboration, R. Adolphi *et al.*, *The CMS experiment at the CERN LHC. The Compact Muon Solenoid experiment*, J. Instrum. **3** (2008) S08004.

[39] LHCb collaboration, A. Alves *et al.*, *The LHCb Detector at the LHC*, J. Instrum. **3** (2008) S08005.

[40] ALICE collaboration, K. Aamodt *et al.*, *The ALICE experiment at the CERN LHC. A Large Ion Collider Experiment*, J. Instrum. **3** (2008) S08002.

[41] CERN, *Web page: ,* https://twiki.cern.ch/twiki/bin/view/Main/LHCb-Facts.

[42] LHCb collaboration, P. R. Barbosa Marinho *et al.*, *LHCb VELO (VErtex LOcator): Technical Design Report*, CERN-LHCC-2001-011; LHCb TDR 5.

[43] R. Aaij *et al.*, *Performance of the LHCb Vertex Locator*, JINST **9** (2014) P09007, 1405.7808.

[44] LHCb collaboration, S. Amato *et al.*, *LHCb Magnet: Technical Design Report*, CERN-LHCC-2000-007.

[45] LHCb collaboration, R. Antunes Nobrega *et al.*, *LHCb reoptimized detector design and performance : Technical Design Report*, CERN-LHCC-2003-030.

[46] LHCb collaboration, A. Franca Barbosa *et al.*, *LHCb inner tracker: Technical Design Report*, CERN-LHCC-2002-029.

[47] LHCb collaboration, P. R. Barbosa Marinho *et al.*, *LHCb outer tracker: Technical Design Report*, CERN-LHCC-2001-024.

[48] LHCb collaboration, R. Hierck *et al.*, *Performance of the LHCb OO track-fitting software*, LHCb-2000-86.

[49] LHCb collaboration, N. Brook *et al.*, *LHCb RICH1 engineering design review report*, LHCb-2004-121.

[50] LHCb collaboration, M. Adinolfi *et al.*, *LHCb RICH2 engineering design review report*, LHCb-EDR-2002-9.

[51] LHCb collaboration, S. Amato *et al.*, *LHCb calorimeters: Technical Design Report*, CERN-LHCC-2000-036.

[52] J. Badier *et al.*, *Shashlik calorimeter: Beam test results*, Nucl. Instrum. Meth. **A348** (1994) 74.

[53] LHCb collaboration, S. Amato *et al.*, *LHCb Muon System Technical Design Report*, CERN-LHCC-2000-007; LHCb-TDR-4.

[54] LHCb collaboration, R. Antunes Nobrega *et al.*, *LHCb trigger system: Technical Design Report*, CERN-LHCC-2003-031.

[55] R. Aaij *et al.*, *The LHCb trigger and its performance in 2011*, JINST **8** (2013) 04022, `arXiv:1211.3055`.

[56] LHCb collaboration, K. Senderowska *et al.*, *HLT1 Electromagnetic Alley*, LHCb-PUB-2009-001.

[57] LHCb collaboration, J. Angel Hernando *et al.*, *The Hadron Alley description*, LHCb-2009-034.

[58] LHCb collaboration, S. Amato *et al.*, *Hlt1 Muon Alley Description*, LHCb-2008-058.

[59] LHCb collaboration, A. Perez-Calero *et al.*, *The muon+track alley of the LHCb High Level Trigger*, LHCb-2008-075.

[60] L. Breiman *et al.*, *Classification and regression trees*, Wadsworth International Group, Belmont, California, USA (1984).

[61] R. Antunes-Nobrega *et al.*, *LHCb computing Technical Design Report*, Tech. Rep. CERN-LHCC-2005-019; LHCb-TDR-11, CERN, Geneva, June, 2005.

[62] I. Belyaev *et al.*, *Handling of the generation of primary events in* Gauss, *the LHCb simulation framework*, Nuclear Science Symposium Conference Record (NSS/MIC) **IEEE** (2010) 1155.

[63] T. Sjöstrand, S. Mrenna, and P. Skands, *PYTHIA 6.4 physics and manual*, JHEP **05** (2006) 026, `arXiv:hep-ph/0603175`.

[64] D. J. Lange, *The EvtGen particle decay simulation package*, Nucl. Instrum. Meth. **A462** (2001) 152.

[65] Geant4 collaboration, S. Agostinelli *et al.*, *Geant4: a simulation toolkit*, Nucl. Instrum. Meth. **A506** (2003) 250.

[66] LHCb collaboration, *The* Boole *project*, Web page http://lhcb-releasearea.web.cern.ch/LHCb-release-area/DOC/boole/.

[67] LHCb collaboration, Brunel- *The LHCb Reconstruction Program*, Web page http://lhcb-release-area.web.cern.ch/LHCb-release-area/DOC/brunel/.

[68] LHCb collaboration, DaVinci- *The LHCb Analysis Program*, Web page http://lhcb-release-area.web.cern.ch/LHCb-release-area/DOC/davinci/.

[69] LHCb collaboration, *Smart and Friendly* C++ *Physics Analysis Toolkit*, CERN Report LHCb-2004-023.

[70] LHCb collaboration, *The* PANORAMIX *Project*, http://lhcb-release-area.web.cern.ch/LHCb-release-area/DOC/panoramix/.

[71] LHCb collaboration, *The* BENDER *Project*, http://lhcb-release-area.web.cern.ch/LHCb-release-area/DOC/bender/.

[72] LHCb collaboration, *The* MOORE *Project*, http://lhcb-release-area.web.cern.ch/LHCb-release-area/DOC/moore/.

[73] CERN, *Web page:* , http://wlcg-public.web.cern.ch/.

[74] K. Abe, M. Satpathy, and H. Yamamoto, *Time-dependent Angular Analysis of B Decays*, UH-511-982-01 BELLE note 419 `arXiv:hep-ex/0103002v1`.

[75] E. P. Wigner, *Group Theory and its Application to the Quantum Mechanics of Atomic Spectra*, New York: Academic Press (1959).

[76] D. Aston *et al.*, *A Study of $K^-\pi^+$ Scattering in the Reaction $K^-p \to K^-\pi^+n$ at 11-GeV/c*, Nucl. Phys. **B296** (1988) 493.

[77] P. Lichard, *Are the production and decay of a resonance always independent?*, Acta Phys. Slov. **49** (1999) 215, `arXiv:9811493v1`.

[78] S. Flatté, *Coupled-channel analysis of the $\pi\eta$ and $K\overline{K}$ systems near $K\overline{K}$ threshold*, Phys. Lett. **B63** (1976) 224.

[79] BES Collaboration, A. M. *et al.*, *Resonances in $J/\psi \to \phi\pi^+\pi^-$ and ϕK^+K^-*, Phys. Lett. **B607** (2005) 243.

[80] LHCb collaboration, R. Aaij *et al.*, *Analysis of the resonant components in $\overline{B}_s^0 \to J/\psi\,\pi^+\pi^-$*, Phys. Rev. **D86** (2012) 052006.

[81] Particle Data Group, E. P. Wigner, *Kinematics, Cross-Section Formulae, and Plots*, Phys. Lett. **B667** (2008) 340.

[82] S. T'Jampens, *Thesis (in French)*, PhD thesis, Université Paris XI, 18 Dec. 2002, BaBar Thesis-03/016.

[83] T. A. Du Pree, *Search for a Strange Phase in Beautiful Oscillations*, PhD thesis, VRIJE University, Amsterdam, 2010, CERN-THESIS-2010-124.

[84] F. Azfar *et al.*, *Formulae for the Analysis of the Flavor-Tagged Decay $B_s^0 \to J/\psi\,\phi$*, JHPE **11** (2010) 158.

[85] R. Aaij *et al.*, *Tagged time-dependent analysis of $B_s^0 \to J/\psi\,K^+K^-$ and $B_s^0 \to J/\psi\,\pi^+\pi^-$ decays with 1.0 fb^{-1}*, LHCb-ANA-2012-067.

[86] R. Aaij *et al.*, *Tagged time-dependent angular analysis with $B_s^0 \to J/\psi\phi$ decay with 337 pb^{-1} of data*, LHCb-ANA-2011-036.

[87] B. R. Wong, *On the overlap integral of associated legendre polynomials*, J. Phys. A:Math. Gen. **31** (1998) 1101.

[88] LHCb collaboration, A. Puig, *The LHCb trigger in 2011 and 2012*, LHCb-PUB-2014-046.

[89] A. Hoeker *et al.*, *TMVA - Toolkit for Multivariate Data Analysis*, 2009. CERN-OPEN-2007-007.

[90] CERN, *ROOT - Data Analysis Framework*, https://root.cern.ch/drupal/.

[91] M. Pivk and F. R. Le Diberder, *sPlot: a statistical tool to unfold data distributions*, Nucl. Instrum. Meth. **A555** (2005) 356, arXiv:physics/0402083.

[92] T. Skwarnicki, *A Study of the Radiative Cascade Transitions Between the Upsilon-Prime and Upsilon Resonances*, PhD thesis, DESY F31-86-02, 1986.

[93] ARGUS collaboration, H. Albrecht *et al.*, *SEARCH FOR $b \to s\gamma$ IN EXCLUSIVE DECAYS OF B MESONS*, Phys. Lett. **B229** (1989) 304.

[94] LHCb collaboration, R. Aaij *et al.*, *Measurement of $\sigma(pp \to b\bar{b}X)$ at $\sqrt{s} = 7$ TeV in the forward region*, Phys. Lett. **B694** (2010) 209, arXiv:1009.2731.

[95] Particle Data Group, K. Nakamura *et al.*, *The review of particle physics*, Nucl. Part. Phys **G37** (2010) 075021.

[96] LHCb collaboration, R. Aaij *et al.*, *Precision measurement of D meson mass differences*, JHEP **06** (2013) 065, arXiv:1304.6865, LHCb-ANA-2012-110.

[97] S. Jadach, *Foam: A general-purpose cellular Monte Carlo event generator*, Computer Physics Communications **152** (2003) 55.

List of Figures

List of Tables

Curriculum Vitae

PERSONAL DETAILS

Name	Anh Duc NGUYEN
Sex	Male
Birth	November 15, 1980
Nationality	Vietnamese
Email	anhduc.nguyen@epfl.ch;ducna_kvl@vnu.edu.vn

EDUCATION

2011-2015	PhD in High Energy Physics, EPFL, Switzerland. Thesis: Determination of the Polarization Amplitudes and CP Asymmetries in $B^0 \to \phi K^*(892)^0$ at LHCb. Supervisor: Dr Trần Minh Tâm (EPFL)
2004-2006	MSc in Physics, Hanoi University of Science - VNU, Vietnam.
1998-2002	BSc in Physics, Hanoi University of Science - VNU, Vietnam.

WORK EXPERIENCE

2011-2015	Teaching Assistant, School of Basic Sciences (EPFL).
9-12/2009	Intern at the Laboratory for High Energy Physics, IPEP, EPFL, I analyzed Monte Carlo Data of the decay $B^0_{(s)} \to D^-_s(K^+K^-\pi^-)\pi^+$.
9-12/2008	Intern at the Laboratory for High Energy Physics, IPEP, EPFL in research work for the LHCb experiment at CERN, my main assignment was to study the misalignment of Inner Tracker detector of the LHCb experiment.
2008	Member of the High Energy Physics Group (GPHE) at the Hanoi University of Sciences.
2002-2008	Teaching assistant at Faculty of Physics - Hanoi University of Science - VNU

SKILLS

Computer:	Programming:	C++, Python.
	Analysis:	Mathlab, ROOT, Multivariate Analysis, Bash/Csh.
	Application:	LaTeX, OpenOffice.
Languages:	Vietnamese, English.	

INTERESTS

Reading, Music, Sports (Ping-pong, footbal, badminton), Travel.